ABSTRACT

Title of Thesis: EVALUATION OF INFORMATION ENTROPY FROM ACOUSTIC EMISSION WAVEFORMS AS A FATIGUE DAMAGE METRIC FOR AL7075-T6

Christine Marie Sauerbrunn, Master of Science, 2016

Thesis Directed By: Professor Mohammad Modarres
Department of Mechanical Engineering

Information entropy measured from acoustic emission (AE) waveforms is shown to be an indicator of fatigue damage in a high-strength aluminum alloy. Several tension-tension fatigue experiments were performed with dogbone samples of aluminum alloy, Al7075-T6, a commonly used material in aerospace structures. Unlike previous studies in which fatigue damage is simply measured based on visible crack growth, this work investigated fatigue damage prior to crack initiation through the use of instantaneous elastic modulus degradation. Three methods of measuring the AE information entropy, regarded as a direct measure of microstructural disorder, are proposed and compared with traditional damage-related AE features. Results show that one of the three entropy measurement methods appears to better assess damage than the traditional AE features, while the other two entropies have unique trends that can differentiate between small and large cracks.

EVALUATION OF INFORMATION ENTROPY FROM ACOUSTIC EMISSION WAVEFORMS AS A FATIGUE DAMAGE METRIC FOR AL7075-T6

by

Christine Marie Sauerbrunn

Thesis submitted to the Faculty of the Graduate School of the
University of Maryland, College Park, in partial fulfillment
of the requirements for the degree of
Master of Science
2016

Advisory Committee:
Professor Mohammad Modarres, Chair and Advisor
Professor Balakumar Balachandran
Professor Hugh Bruck

© Copyright by
Christine Marie Sauerbrunn
2016

Acknowledgements

First and foremost, I would like to thank my advisor, Dr. Mohammad Modarres, for the continued support and guidance throughout both my undergraduate and Master's studies. I am grateful for the research experience, opportunities, and knowledge you have given to me over the past three years. I would also like to extend my appreciation to my other committee members, Dr. Hugh Bruck and Dr. Balakumar Balachandran. Thank you both for your guidance in the classroom and your advice on this work.

Many thanks are extended to my coworkers and friends at the Center of Risk and Reliability (CRR). Specifically, thank you to Huisung Yun for being a great research partner to bounce ideas off of, for your positive attitude each time the lab equipment malfunctioned, and for your unwavering commitment to polishing, imaging, and preparing all the test specimens. Your help over the past two years has been truly invaluable. I am also appreciative for my discussions with Dr. Ali Kahirdeh about acoustic emissions and information entropy. You have encouraged me to think critically about my engineering assumptions while also teaching me to be less self-critical. Finally, thank you to those who first welcomed me to CRR as an undergraduate and helped me get accustomed to research practices; Victor Ontiveros, Mehdi Amiri, Azadeh Keshtgar, and Abdullah Al Tamimi.

I am also so thankful for my loving and supportive family and friends. Thank you Mom and Dad for always encouraging me to achieve my goals – I could not have done any of this without you. To my sisters, Liz and Steph, thanks for always welcoming me home after the stressful weeks at school. And to my Oma, thank you

for always reminding me of the importance of education and supporting all of my endeavors. Special thanks goes to my college friends for all of the fun times and distractions from the stress of classes and work. You all have kept me sane these past five years and have made my time at Maryland unforgettable. Our friendships will extend for many years to come.

Finally, this research would not have been possible without the financial support of the Office of Naval Research under grant #N00014140453. On behalf of myself and the University of Maryland, thank you for your generous support.

Table of Contents

Acknowledgements ii
Table of Contents iv
List of Tables vi
List of Figures vii
List of Abbreviations ix
Chapter 1 – Introduction 1
1.1 Motivation and Background 1
1.2 Research Objectives and Methodology 4
1.3 Contributions 5
1.4 Outline of Thesis 5
Chapter 2 – Literature Review 7
2.1 Fatigue Damage in Metals 7
2.1.1 Stages of Fatigue 7
2.1.2 Literature on Crack Nucleation, Initiation, and Small Cracks 9
2.2 Acoustic Emission Background 12
2.2.1 AE Theory 12
2.2.2 AE Instrumentation and Terminology 13
2.2.3 Estimating Fatigue Damage with AE 17
2.3 Information Entropy Background 21
2.3.1 Understanding Information Entropy 21
2.3.2 Application of Information Entropy to Fatigue and AE 25
Chapter 3 – Experimental Procedure 30
3.1 Specimen Preparation 30
3.2 Loading Conditions 32
3.3 Strain Measurement 35
3.4 Crack Monitoring System 37
3.5 Acoustic Emission Instrumentation 40
3.6 Mechanical Damping Apparatus 40
3.6.1 Why Mechanical Damping? 40
3.6.2 Damping Techniques 41
3.7 Details of Individual Fatigue Experiments 43
Chapter 4 – Post-Processing Methods 45
4.1 Noise Reduction 45
4.2 Instantaneous Elastic Modulus Calculations 49
4.3 Discrete Information Entropy Formulations 51
4.3.1 Feature Entropy 53
4.3.2 Updated Entropy 55
4.3.3 Temporally Weighted Entropy 57
4.3.4 Summary of Entropy Formations 59
Chapter 5 – Results and Discussion 61
5.1 Crack Growth and Fracture Surface Images 61
5.2 Stress-Life Analysis 63

5.3 Measured Damage from Modulus Degradation 65
5.3.1 Modulus Trends 65
5.3.2 Normalizing Modulus to Produce Measured Damage 68
5.4 AE Parameter Cyclic Trends 73
5.4.1 AE Counts 73
5.4.2 AE Absolute Energy 76
5.4.3 Feature Entropy 77
5.4.4 Updated Entropy 79
5.4.5 Temporally Weighted Entropy 81
5.5 Normalized AE Parameters Compared to Measured Damage 83
5.5.1 Cumulative Counts, Energy, and Feature Entropy 83
5.5.2 Updated and Temporally Weighted Entropy 87
5.6 Summary of Results 89
Chapter 6 – Conclusions 90
6.1 Summary 90
6.2 Contributions 91
6.3 Future Work 92
Appendices 95
Appendix A – Applied Load vs. Signal Arrival Time Scatter Plots 95
Appendix B – Code for Modulus Evolution 101
Appendix C – Error Propagation 104
C.1 Initial Elastic Modulus 104
C.2 Measured Crack Length 105
Appendix D – Code for AE Entropy Formulations 107
Appendix E – Code for Matching Modulus and AE Hits Data 111
Bibliography 114

List of Tables

Table 1: Various definitions of crack phases 10
Table 2: User defined AE parameters and their descriptions [27] 16
Table 3: Commonly extracted AE features and their descriptions [4, 27] 17
Table 4: Composition and mechanical properties for Al7075-T6 30
Table 5: Loading conditions for each experiment 34
Table 6: Experiments for each loading condition 34
Table 7: Strain measurement techniques and associated attributes. Advantages are in green, disadvantages are in red. 37
Table 8: AE software settings 40
Table 9: Experiment details. Tests with any detail in red are discarded 44
Table 10: AE noise behavior for each test with an acceptable test setup 49
Table 11: Measurement uncertainty for 11 experiments 51
Table 12: Summary of entropy formulations 60
Table 13: Parameters for theoretical S-N curve for particular Al7075-T6 specimen. 64
Table 14: Fitted models for measured damage 69
Table 15: Error for crack length measurements 71
Table 16: Error in cycles at measured crack lengths 72

List of Figures

Figure 1: Proposed Short-Term Loading Process (STLP) where constant high-amplitude loading is interrupted by small excitation loading to observe response of damage precursor parameter 3
Figure 2: Crack development and phases of fatigue life 8
Figure 3: AE sensor recording surface displacement waves from damage region 13
Figure 4: Transformation of AE signal due to signal shaping chain. Adapted from [4]. 15
Figure 5: AE voltage waveform with labelled features 15
Figure 6: a) Probability mass function (PMF) of flipping a fair coin and calculated information entropy. b) PMF of a biased coin with probability of flipping tails as 0.70 and calculated entropy. c) PMF of a biased coin with probability of flipping tails as 0.99 and calculated entropy. 23
Figure 7: a) PMF of a rolling a fair die and calculated information entropy. b) PMF of a weighted coin with greater probability of rolling a 4. c) PMF of coin 97.5% likely to result in a 4 and calculated entropy. 24
Figure 8: Microstructural disorder as defined by fatigue damage evolution 27
Figure 9: Fatigue specimen geometry 31
Figure 10: Probability distribution of grain diameter for 375 measured grains 32
Figure 11: Servo-hydraulic MTS machine 33
Figure 12: Crack surfaces for 5A26 and 5A18 35
Figure 13: Circular segment dimensions 38
Figure 14: Optical microscope images during fatigue of specimen 5A26 39
Figure 15: AE noise amplitude with and without mechanical damping 42
Figure 16: a) Mechanical damping method. b) Complete experimental setup. 43
Figure 17: Likely and unlikely AE hits based on applied load 45
Figure 18: AE signals at their associated loads versus time for 5A26. No apparent AE noise. 47
Figure 19: Applied load at instant of AE signals at their arrival times for 5A22. Filterable noise. 48
Figure 20: Applied load at recorded AE signals and their arrival times for 5A20. Unfilterable AE noise. 48
Figure 21: Feature entropy calculation from AE signals 54
Figure 22: Updated entropy calculation from AE signals 56
Figure 23: Temporally weighted entropy calculation from AE signals 59
Figure 24: Entropy evolution for three examples of AE signals for each formulation 60
Figure 25: Crack growth through grains and inclusions 61
Figure 26: Brittle and ductile regions of fatigue crack growth 62
Figure 27: Fatigue striations in the brittle region 62
Figure 28: Highly disordered ductile region with no striations 62
Figure 29: Experimental S-N plot with theoretical and experimental S-N curves 65
Figure 30: Raw modulus degradation for 8 experiments at various damage levels 66
Figure 31: 5A25 fracture surface showing two displaced regions at notch 68
Figure 32: Measured damage for 8 experiments at various damage levels 70
Figure 33: Cumulative AE counts versus fatigue cycles until fracture 74

Figure 34: Cumulative AE energy versus fatigue cycles until fracture 77
Figure 35: Cumulative feature entropy versus fatigue cycles until fracture 78
Figure 36: Updated entropy versus fatigue cycles until a 1 mm crack and fracture... 81
Figure 37: Temporally weighted entropy versus fatigue cycles until a 1 mm crack and fracture 82
Figure 38: Normalized cumulative counts, energy, and feature entropy with respect to measured damage where a one-to-one relationship is desired..... 85
Figure 39: Example of deviations between ideal and experimental trends 86
Figure 40: Deviation factor for AE counts, energy, and feature entropy for all experiments 87
Figure 41: Normalized updated and temporally weighted entropy against measured damage 88

List of Abbreviations

AE – Acoustic emission

CV – Coefficient of variation

LEFM – Linear elastic fracture mechanics

MaxEnt – Principle of maximum entropy

NDE – Nondestructive evaluation

PMF – Probability mass function

PSBs – Persistent slip bands

SHM – Structural health monitoring

STLP – Short-Term Loading Process

Chapter 1 – Introduction

1.1 Motivation and Background

Virtually all engineered structures undergo some form of cyclic fatigue. For example, mechanical gears can experience tooth fracture while rotating mechanical shafts can fail due to repeated torsional loading. Systems with such components are often permitted to fail when the safety risk is minimal and the components can be replaced at a relatively low cost. However, structures such as bridges and aircraft include critical components where extensive safety risks and monetary losses are a concern upon failure. In turn, estimating when a failure may occur is imperative and inspecting these structures for fatigue damage is common practice.

Specifically for aircraft, decades of research and experience have produced guidelines for estimating ideal service life. There are two main approaches for determining retirement time of military aircraft referred to as damage tolerant and safe-life. The United States Air Force adheres to the damage tolerant approach which assumes the structure has inherent defects and predicts the instance when these defects grow to become cracks of critical length [1]. In contrast, the safe-life approach assumes a new structure has no flaws and retires an aircraft based on recorded loading data and estimated crack initiation time. The United States Navy uses this approach because of the extreme loading conditions of taking off and landing on aircraft carriers with relatively short runways. Aircraft are retired once a crack is estimated to initiate and extend to a 0.25 mm length based on extensive and time-consuming, full-scale fatigue tests [1]. While the lower damage threshold of the safe-life approach reduces the likelihood of catastrophic failure, the high safety

factors tend to lead to premature retirement and a lower return on investment for aircraft owners [2].

Rather than basing retirement time solely on estimated crack initiation and full-scale testing, structural health monitoring (SHM) and nondestructive evaluation (NDE) methods can be used to estimate the actual material damage due to fatigue. While SHM is most desirable in that the entire structural health is continuously monitored, NDE methods that evaluate structural health during discrete inspection periods are more practical and often implemented. Traditional NDE methods include visual, eddy current, ultrasonic, and radiographic testing [3]. Each of these inspection techniques can assess damage within a structure to a degree of certainty when the probable damage location is known.

Another technique that can be used is acoustic emission (AE). Acoustic emission is a technique by which elastic stress waves that propagate through a material at sources of stress are recorded as electrical signals [4]. In contrast to the other NDE methods which detect geometric discontinuities when actively positioned in anticipated damage locations, AE is a potential SHM technique that passively and continuously records microstructural movements even prior to a visible crack. Despite this advantage, however, AE is susceptible to extraneous noise. Distinguishing between noise and damage-related signals is a critical obstacle that has limited the practical SHM application of AE. Instead, AE can be used as an NDE method when noise signals can be filtered in a controlled testing environment.

While AE research over the past few decades has proven effective in estimating visible cracks and crack growth rate, detecting fatigue damage at the

earliest instance using AE is most desirable. This goal motivated the current research which is the first of two stages. The first stage is identifying AE precursors attributed to cyclic slip and microcracks prior to visible damage. These precursors are then characterized as damage increases within a structure during constant high-amplitude loading. Once damage precursors and their behaviors are completely investigated during normal conditions, the second stage seeks to quantify the changes in these behaviors during a short-term, high-frequency excitation loading referred to as a Short-Term Loading Process (STLP). The STLP concept is depicted in Figure 1 where $d\alpha/dN$ is the evolution of the precursor's behavior. In these experiments, a constant high-amplitude load will be applied to a structure. This loading will then be interrupted at several instances throughout the fatigue life to measure the known changes in the identified fatigue damage precursors due to the STLP. By knowing the evolution of precursor behavior during a STLP at various degrees of damage, the fatigue damage of a structure with unknown loading history could potentially be estimated by a simple STLP.

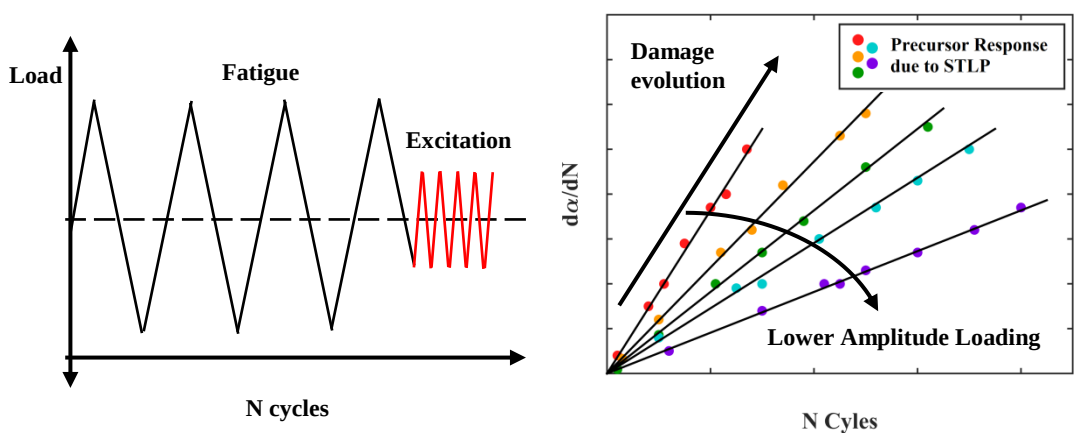

Figure 1: Proposed Short-Term Loading Process (STLP) where constant high-amplitude loading is interrupted by small excitation loading to observe response of damage precursor parameter

1.2 Research Objectives and Methodology

The objectives of this work are listed as the following:

1. Assess the validity of using instantaneous elastic modulus as a measure of the true microstructural damage in metallic structures.
2. Develop quantitative statistics that reflect the information carried within AE signals.
3. Investigate how features and information from AE signals correlate to fatigue damage prior to a visible crack and compare the utility of these various AE damage parameters.
4. Discuss advantages and limitations of AE damage parameters and suggest damage precursors to be used in STLP testing.

In order to achieve these objectives, a series of fatigue experiments were performed on Al7075-T6, a commonly used material in aerospace structures. The local strain around a semicircular notch and the acoustic signals emitted from microstructural damage were measured during the experiments. Unlike previous studies in which fatigue damage is easily measured based on visible crack growth, this work assumes that instantaneous elastic modulus can be an estimate of the unobservable microstructural damage. Subsequently, AE features and information from AE signals are correlated to modulus degradation in order to estimate damage prior to a visible crack.

Both traditional AE features like AE counts and AE energy are investigated as well as various formulations of information entropy from AE signals to correlate to fatigue damage. Information entropy is the measure of the disorder of any probability distribution. In turn, it is hypothesized that the information entropy from probability

distributions of AE signals reflect microstructural disorder and therefore fatigue damage. Several different methods of representing AE signals as probability distributions are developed from which several measures of information entropy are derived. The strengths and weaknesses of each of these measures in regards to correlating with true fatigue damage are discussed.

1.3 Contributions

The contributions of this work are listed as the following:

1. Techniques to reduce extraneous AE noise through development of mechanical damping apparatus and justified post-process filtering.
2. A procedure to measure damage based on elastic modulus degradation.
3. Processes to derive three different proposed information entropy measurements from individual AE signals.
4. Comparison of the traditional AE features and information entropy formulations in regards to fatigue damage.

1.4 Outline of Thesis

The rest of this thesis is divided into five chapters. First, Chapter 2 details theory, background, and previous research related to fatigue damage in metals, AE, and information entropy. Chapter 3 describes the experimental procedure including specimen design, data measurement systems, the mechanical damping apparatus, and the characteristics of each fatigue experiment performed. Next, Chapter 4 explains the post-processing methods to reduce AE noise, calculate instantaneous elastic modulus, and derive three different formulations of AE information entropy. Then, results pertaining to crack behavior, stress-life analysis, measured damage from elastic

modulus degradation, AE features, and AE information entropy metrics are discussed in Chapter 5. Finally, conclusions and recommendations for future work are provided in Chapter 6.

Chapter 2 – Literature Review

2.1 Fatigue Damage in Metals

2.1.1 Stages of Fatigue

Fatigue is the gradual degradation and eventual failure of a material that occurs due to cyclic loading lower than the material's static strength. Research pioneered by August Wöhler during the mid-19th century led to the conclusion that materials can fail due to repeated stresses that are below the yield strength [5]. Since this time, many other instances of fatigue in mechanical components have been documented and inspired subsequent investigations. An extensive history of fatigue in metals between 1837 and 1994 is given by Schütz [6].

Fatigue is often characterized as three phases of damage: crack initiation, stable crack growth, and unstable crack growth until fracture. This fatigue process is illustrated in Figure 2 and thoroughly explained by Schijve [7]. Fatigue damage begins very early in fatigue life as invisible microcracks nucleate at persistent slip bands (PSBs). These PSBs are a result of moving dislocations within the material due to applied stress. Dislocations move along the direction with greatest shear stress, which varies within a material based on size, shape, crystallographic orientation, and elastic anisotropy of grains [7, 8]. Also, because surface grains are less constrained than subsurface grains, slip bands are more likely to occur at surface grains where the shear stress is often more significant and where dislocations move towards. Once a slip band occurs at a surface grain and a new surface is exposed to air, oxygen is absorbed causing local decohesion of the slip step [8]. This phenomenon causes sites for microcrack initiation.

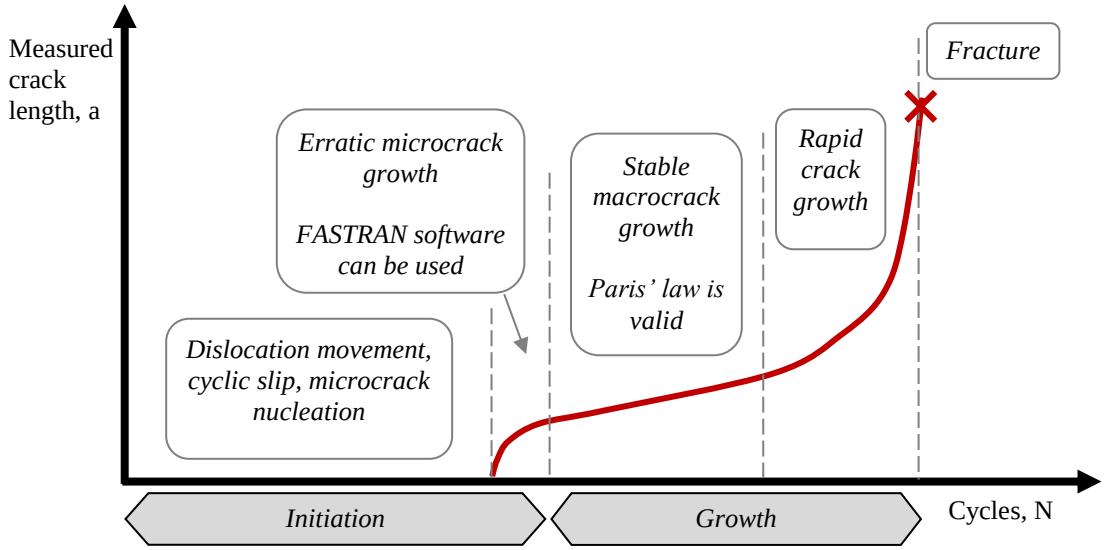

Figure 2: Crack development and phases of fatigue life

The initiated microcrack will grow depending on the surrounding microstructure. As a crack grows through the first grain, it will approach an adjacent grain with its own crystalline orientation and ideal slip system direction. The crack in the first grain will then deviate from its original propagation direction based on the second grain's slip system. Because each grain impedes the crack growth to a varying degree, crack growth rate for microcracks is erratic and dependent on grain boundaries. The microcrack will continue to grow through subsequent grains and inclusions changing its propagation path each time.

Once the microcrack has created a large crack front spanning numerous grains, the crack will propagate at a more consistent rate. This is when a crack transitions from a small crack to a large crack. This transition is often determined based on whether the crack growth rate can be characterized by Paris' law [9]. Introduced in 1961, Paris [9] proposed that the crack growth rate is related to the material's stress intensity factor range by means of a power relationship. This relationship is recounted in Equation (2.1) where da/dN is the crack growth rate, ΔK

is the stress intensity factor range, and C and m are constants dependent on the material. Once a large crack reaches a certain length, the crack will rapidly propagate and cause fracture.

$$\frac{da}{dN} = C\Delta K^m \tag{2.1}$$

2.1.2 Literature on Crack Nucleation, Initiation, and Small Cracks

A main research topic related to fatigue in metals is differentiating between small cracks and large cracks and attempting to model crack initiation and small crack growth. Crack growth rates for large cracks can be predicted by linear elastic fracture mechanics (LEFM) models including Paris' law. For LEFM to be valid, the plastic zone around the crack tip should be small relative to the entire crack length. Moreover, this plastic zone should enclose a sufficient number of grains and inclusions for the crack growth rate to be stable [10, 11, 12]. Other sources have further differentiated small cracks into microstructurally small and physically small. While the exact differentiation between small crack phases is unclear, most agree that microstructurally small cracks are about the size of a few grain diameters and physically small cracks are those between several grain diameters and 1 mm. Table 1 summarizes multiple sources' definitions of crack phases. As previously mentioned, the U.S. Navy retires aircraft once a small crack exceeds 0.25 mm [1]. In turn, this work will focus on fatigue damage prior to a 0.25 mm crack to match U.S. Navy criteria as well as until such a crack reaches 1 mm to agree with common small crack length definitions.

Table 1: Various definitions of crack phases

Source	Crack phases			
[5]	**Short cracks**		**Long cracks**	
	• Length = less than 1 mm • Inclusions and grain boundaries influence growth		• Length = greater than 10 mm • Microstructure and loading ratios have little influence	
[7]	**Crack nucleation**	**Microstructurally short cracks**	**Mechanically short cracks**	**Macrocracks**
	• Length = 1 nm – 1 µm • Influenced by surface roughness and microstructure	• Length = 1 nm – 100 µm • Crack growth is stunted by microstructural barriers	• Length = 100 µm – 1 mm • Crack growth is stunted by changes in crack tip stress field	• Length = greater than 1 mm • Bulk material phenomenon
[8]	**Microstructurally short cracks**	**Mechanically short cracks**	**Physically short cracks**	**Long cracks**
	• Length = a few grain diameters • Strong influence of microstructure and surface roughness	• Length = several grain diameters • Little influence of the microstructure • Large plastic zone ahead of crack	• Length = less than 0.5 mm • Small plastic zone ahead of the crack tip relative to crack length • LEFM is applicable	• Length = greater than 0.5 mm • Completely developed • Paris' law is applicable
[11]	**Crack nucleation**	**Microstructurally small cracks**	**Physically small cracks**	**Dominant long cracks**
	• Length = Unspecified • Crack propagation through zone of the micro-notch root influence	• Length = less than 3 times the characteristic length scale of microstructural interactions (MS) • Affected by the grain orientation	• Length = 300-800 µm, between 3MS and 10MS • Affected by the grain orientation	• Length = less than greater than 20MS • Cyclic plastic zone is small relative to crack length • LEFM is applicable
[10, 22, 24]	**Microstructurally short cracks**	**Physically short cracks**	**Long cracks**	
	• Length = similar to grain size • Continuum mechanics is questionable	• Length = on the order of a grain or less • Reduced crack-closure effect	• Length = greater than 0.5-1 mm • Paris' law holds	
[14, 15]	**Small cracks**		**Long cracks**	
	• Length = less than 1 mm • Nonlinear crack growth so LEFM is not applicable		• Length = greater than 1 mm • LEFM is applicable	
[16]	**Small cracks**		**Long cracks**	
	• Length = on the order of a grain or less • LEFM is not applicable		• Length = larger than a few grains • LEFM is applicable	

Researchers have continually attempted to model the erratic behavior of crack initiation and small crack growth. One notable researcher in this field is James C. Newman, a former NASA engineer. He developed the FASTRAN software that predicts fatigue life using plastically-induced crack-closure models [13]. In 1998 and 1999, Newman, Wu, and their coworkers [14, 15] published work on small crack growth, defined as between 10 μm and 1 mm in length, and fatigue life predictions for Al 7075-T6 and LC9cs clad alloy. The objective was to determine a "single analysis method that was applicable to all crack sizes". Fatigue experiments along with finite element analyses and weight function analyses assessed the validity of estimating small and large crack growth rates with the FASTRAN software. In turn, the proposed model was able to predict fatigue life to an acceptable degree of accuracy. Newman [16, 17, 18] has continued researching small crack growth using FASTRAN models over the past decade.

While FASTRAN software has proven to be a vital tool for predicting fatigue life, greater accuracy is achieved when the current microstructural damage is known. FASTRAN is based on fatigue experiments where cyclic loading was paused so that the material's surfaces could be replicated. The size and shape of small cracks were then identified from scanning electron microscope images of the replicas. This process, however, cannot be implemented on a large scale. Observing fatigue damage on a microstructural level is ideal, but the replica method cannot easily be implemented as an NDE method. This limitation encourages investigations of other practical NDE methods that can estimate the fatigue damage on a microscopic level.

Another prominent researcher of fatigue and fracture mechanics of small cracks is Hael Mughrabi. Similar to Newman, he focuses on estimating fatigue damage based on microstructural changes. Several of his papers [12, 19, 20] discuss microstructural fatigue mechanisms such as cyclic irreversibilities and PSBs in α-iron polycrystals and α-brass single crystals. In addition, other authors have been published notable works [10, 21, 22, 23, 24, 25] that discuss microscale fatigue damage in Al7075-T6 and Ti-6Al-4V, both materials used in aerospace structures. Despite progress in microstructure-based models of fatigue, Mughrabi [12] noted that "a full understanding of the underlying damage mechanisms and the relationship to the fatigue life is difficult to achieve and still lacking". Again, while a microstructurally-based fatigue model for crack nucleation, initiation, and small crack growth is desired, it is best to develop more practical methods of measuring microstructural fatigue damage through NDE techniques.

2.2 Acoustic Emission Background

2.2.1 AE Theory

AE has become a recognized NDE method commonly used to detect flaws in mechanically loaded structures. Other NDE procedures such as ultrasonic and radiographic testing measure a component's response to an actively applied external source. In contrast, AE is a passive method that senses minute surface displacements due to propagating internal elastic waves from sources of stress as shown in Figure 3. Theoretically, acoustic waves due to damage are continuously propagating through a structure when under repeated stress. Once the applied stress causes permanent deformation, stored elastic strain energy is released partly in the form of an acoustic

wave. For each instance of deformation, an acoustic wave is emitted. Consequently, AE has the potential to measure fatigue damage from dislocation motion to crack initiation and to large crack propagation. However, the ability to measure AE is limited by noise. Noise can come from many sources including mechanical vibrations from the testing machine and electrical interference with the instrumentation [4]. In turn, an amplitude threshold is often established. While this threshold allows the system to reject unwanted noise signals, AE signals related to damage and below the noise amplitude will not be detected. As a result, AE transducers cannot monitor in-flight aircraft structural health, but they can rather be used as an inspection method used in a controlled environment.

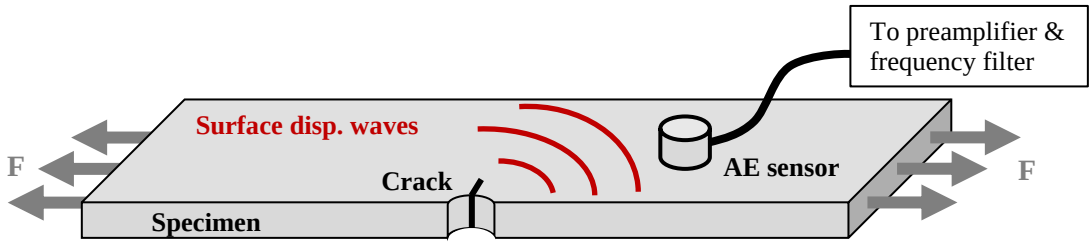

Figure 3: AE sensor recording surface displacement waves from damage region

2.2.2 AE Instrumentation and Terminology

The measurement of acoustic emissions began with Joseph Kaiser in 1950 [4]. Since then, standardized AE instrumentation including sensors, preamplifiers, and acquisition systems have been developed. Sensing the elastic wave within in the structure is the first step in measuring and recording AE signals. Most AE sensors are piezoelectric transducers which utilize the piezoelectric effect. These sensors contain a piezoelectric crystal that produces a change in electrical voltage when under mechanical strain. Therefore, when these materials are fastened to a deforming surface, the mechanical wave is transformed into an electrical signal. While the

electrical signal's size and shape is dependent on the elastic wave, it is also influenced by the frequency behavior of the piezoelectric sensor. There are two general types of sensors; resonant and wideband. Resonant sensors operate in a narrow band near the sensor's resonant frequency while wideband sensors are damped in order to detect a broader range of AE signal frequencies. Resonant sensors are often preferred because they are generally more sensitive and less expensive than wideband sensors [26]. While wideband sensors are able to reconstruct the elastic wave more accurately in regards to frequency spectrum, they are less sensitive.

Once an AE piezoelectric sensor converts a surface displacement into an electrical voltage signal, the signal is passed through a preamplifier and band-pass filter. The preamplifier should be set to properly amplify the signals, and frequency filter characteristics should be selected to match the sensor's attributes. Typically, the preamplifier is set between 20 dB and 60 dB, and the band pass filter is set between 1 kHz and 2 MHz [26]. The filter will be able to reject noise signals that often have a low frequency and capture damage-related AE signals which typically have frequencies in the range of 150-300 kHz [4].

Also, it is important to note that the recorded AE signals will have a drastically different waveform shape compared to the actual elastic wave. This phenomenon is due to the transformations between an AE source and the acquisition module and is referred to as the signal shaping chain as depicted in Figure 4 [4]. The source of the elastic wave is assumed to be one sudden peak with a smooth frequency distribution. The wave within the structure then attenuates and reflects off of the structure's boundaries, distorting the wave in the time and frequency domains. Then,

because the AE sensor has its own time and frequency response, the electrical signal is an altered form of the propagating elastic wave. Finally, the signal is transformed again after being amplified and filtered. Even though the recorded AE signal is not in fact the exact AE wave within the structure, one can deduce aspects of the AE source from the recorded signal since all AE waves go through the same transformation.

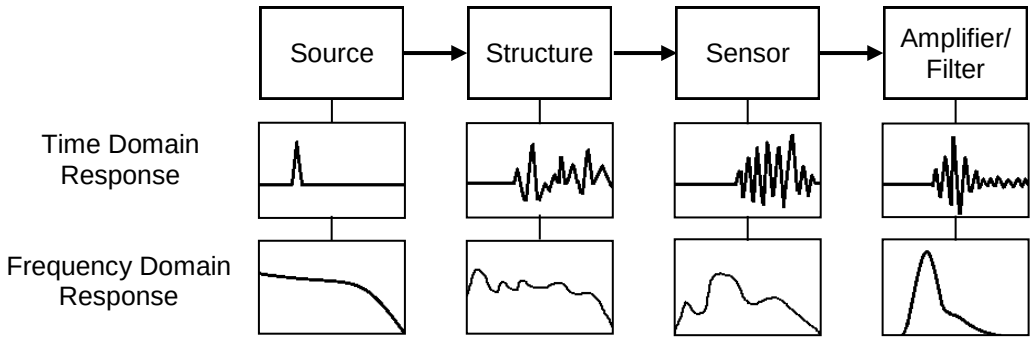

Figure 4: Transformation of AE signal due to signal shaping chain. Adapted from [4].

An example of an AE waveform is given in Figure 5. As one can see, the beginning of the signal has a voltage that oscillates close to 0 volts identified as background noise. After a damage-related elastic wave propagates to the AE sensor, the AE signal's amplitude then increases to a peak amplitude. Subsequently, the signal attenuates back to the background noise behavior.

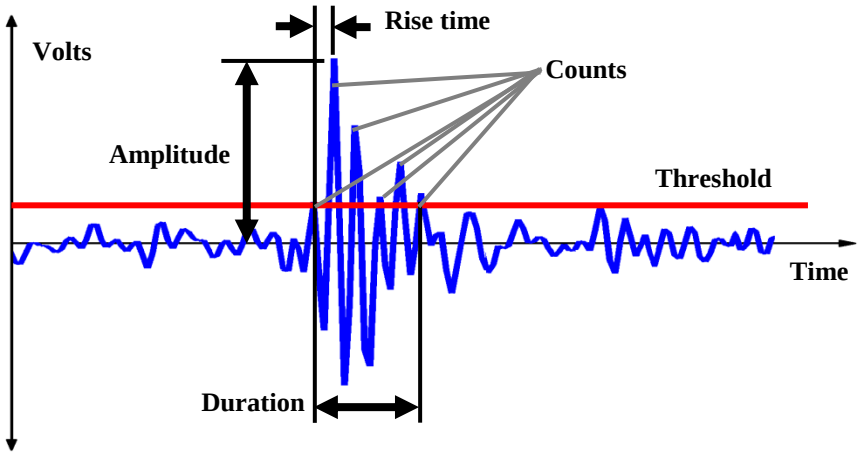

Figure 5: AE voltage waveform with labelled features

Two important duties an AE acquisition needs to perform is 1) to divide the continuous and complex AE signal into individual waveforms that can be processed and 2) to extract relevant features from these waveforms. For the first task, a series of parameters is often set depending on the structure's material and geometry. These are described in Table 2 [27].

Table 2: User defined AE parameters and their descriptions [27]

User-Defined AE Parameters	Description
Threshold	Voltage value in units of dB that records an AE waveform as a hit when the waveform exceeds this value. Variable that controls the sensitivity.
Sampling rate	The rate at which the acquisition board samples waveforms on a per second basis. Value is described in units of megasamples per second (MSPS) where 1 MSPS means a sample is taken for every 1 µs.
Pre-trigger	Value that tells the software how long to record the AE waveform prior to the first voltage threshold crossing. Units are in microseconds. Can be set from 0 µs to the hit length divided by the sample rate.
Hit length	Value that determines the waveform length. This value can range between 1k and 15k where k = 1024 values. The length of time recorded over the hit is found by dividing the hit length by the sampling rate. For example, k for a 1 MSPS sampling rate means 1024 values will be measured, 1 for every µs, and the waveform will span a time of 1024 µs.
Peak definition time (PDT)	Ensures correct identification of the signal peak for rise time and peak amplitude measurements. For small metal specimens, the recommended value is 300 µs.
Hit definition time (HDT)	Ensures each AE signal from the structure is reported as one and only one hit. For small metal specimens, the recommended value is 600 µs.
Hit lockout time (HLT)	Extraneous measurements during the signals decay are excluded based on this value. For small metal specimens, the recommended value is 1000 µs.

For the second duty of an acquisition system, numerous AE features are now common place. These features are labeled in Figure 5 and described below in Table 3 [4, 27].

Table 3: Commonly extracted AE features and their descriptions [4, 27]

Commonly Extracted AE Features	Description
Amplitude	The largest voltage value present in the waveform and measured in dB using Equation (2.2). For a signal to be recorded, the amplitude needs to be above the threshold.
Counts	The number of times the voltage signal crosses the threshold. One of the easiest measurements of the signal and often used in analysis. Value usually is between a single count to a few hundreds.
Duration	Length of time from the first count to the last count and measured in microseconds. A long duration means the signal is drawn-out while a short duration implies a burst-type signal.
Rise time	The time between the first count and the count with the greatest amplitude. Units are in microseconds.
Energy	The area under the voltage-time envelope. This feature is a common measure for discussing AE signals in regards to structural damage.
Absolute energy	Measured value of the squared voltage signal divided by a reference resistance over the duration of the AE waveform used by particular AE acquisition systems. Units are in attojoules (10^{-18} joules).
Average frequency	A calculated feature reported in kHz that measures the number of counts over the duration of the signal.
Frequency centroid	Reported in kHz, this value is derived in real time from the Fast Fourier Transform of each signal.
Peak frequency	Frequency of the signal when the maximum amplitude occurs. This frequency feature is also reported in kHz.

$$dB = 20\log_{10}\left(\frac{V_{max}}{10^{-6}\ volts}\right) - Preamplifer\ Gain\ in\ dB \qquad (2.2)$$

Within this section, the theory and instrumentation for the AE method has been detailed. Now that AE background has been covered, recent literature on estimating structural damage with AE can be summarized.

2.2.3 Estimating Fatigue Damage with AE

Over the past few decades, researchers have had success correlating AE signals and their features to fatigue crack propagation in metals. Specifically, many people have been able to relate AE count rate to crack propagation rate using a power relationship similar to Paris' law. This relationship is given as Equation (2.3) where a is crack length, c is AE counts, the derivatives of a and c with respect to N cycles are the crack growth rate and AE count rate, and α_1 and α_2 are model parameters.

$$\frac{da}{dN} = \alpha_1 \frac{dc}{dN}^{\alpha_2} \tag{2.3}$$

In 1973, Morton [28] tested this relationship on Al 2024-T831. He concluded that *dc/dN* appeared to be better correlated to the stress intensity range, ΔK, than between *dc/dN* and *da/dN* or *da/dN* and ΔK. Bassim [29] performed fatigue tests on several railway steels to test this hypothesis in 1994 while Berkovits and Fang [30] performed their own experiments on Incoloy 901 a year later. Both studies looked to correlate AE features to the earliest instance of fatigue but had more success relating AE hits once a crack was propagating. Berkovits and Fang noted that "conventional test methods, based on the crack propagation test, cannot accurately measure the initial length of the initial crack because of the impossibility of determining the critical initiation onset in real time". In the end, both studies countered Morton's claim and supported a strong relationship between *dc/dN* and *da/dN* that followed Equation (2.3). Since this time, other researchers [31, 32, 33, 34, 35, 36, 37] have looked to expand on relating AE counts to crack growth rate.

In addition to correlating AE counts to fatigue damage, studies have investigated how other AE features such as energy, rise time, duration, and frequency transform as fatigue damage progresses. Results presented by Han [35] show AE hits that occur during stable crack propagation generally have higher rise times and lower amplitudes compared to AE hits during unstable propagation and fracture. Vanniamparambil and coworkers [38] performed tensile tests on Al2024 specimens and reported that amplitude, absolute energy, counts, and count rate were the most sensitive AE features to crack growth. Vanniamparambil [39] continued investigating these AE features and concluded that the onset of a crack is associated with a shift

from low frequency to high frequency waveforms. AE signals can also be classified based on rise time, amplitude, energy, and average frequency where all of these features increase near 90% of fatigue life [40]. In addition, Keshtgar [36] proposed that the ratio between the signal amplitude and the threshold amplitude scaled by the number of counts in the signal could be used as another AE damage-related feature. Because several AE features have proven to be able to classify AE signals throughout structural damage, this current study will also consider these features during fatigue tests.

While estimating crack growth rate based on AE signals is a profound accomplishment, estimating crack damage at the smallest possible scale is most desirable. This idea has motivated many people to look at possible AE sources at the atomic scale to better understand wave dynamics within measured AE signals. One technique is to perform tensile and compression experiments on crystals and compare results with theoretical wave equations. James and Carpenter [41] were two such researchers who investigated AE count rate during compression tests on several different crystals. They reported AE counts were generated from dislocation breakaway from pinning points and that AE count rate could be related to dislocation velocity. Polyzos and Trochidis [42, 43, 44] modeled the interaction between dislocations and transverse acoustic waves in copper crystals during tensile tests. They concluded that both nonstationary dislocation motion and annihilation of dislocation kink-antikink pairs are mechanisms for AE signals. Researchers at the Institute of Thermomechanics [45, 46] developed molecular dynamic simulations to calculate stress and local kinetic energies during dislocation motion and twinning in

body-centered cubic iron crystals. Overall, studies have confirmed that AE waves within structures propagate due to dislocation motion.

While observing and modeling acoustic waves within single crystals is vital to understanding AE mechanisms, studying AE sources within impure, polycrystalline materials is far more challenging but more applicable to real world situations. Due to precipitates, inclusions, and various grain orientations in metallic alloys, pinpointing the exact AE mechanism is often hypothesized but rarely proven. Despite the difficultly, many researchers have looked to correlate AE signals to microstructural changes.

AE mechanisms within variously-aged 9Cr-1Mo steel during crack initiation and growth were investigated by Chaswal [47]. This work suggested that crack nucleation took place at the precipitate-matrix interfaces, sudden bursts of hundreds of low amplitude AE signals in a short time correspond to micro-cleavage of ligaments, and extended periods of inactivity correspond to dislocation pile up. Rahman [48] performed rolling contact fatigue tests on rail steel with AE and concluded AE count rate can detect incipient damage and is related to damage size and confirming previous findings [49]. Similarly, Elforjani and Mba [50] concluded there is a relationship between AE counts, energy, and amplitude to detecting incipient cracks in slow speed shafts. During tensile tests of Al7075, Lugo and coworkers [51] reported that much AE activity was recorded in the initial stage compared to later stages and hypothesized that most inclusions cracked in the early deformation stages. Finally, other recent studies [35, 36, 39, 52, 53, 54, 55] hypothesized when crack initiation occurred based on AE signals, but they did not

directly correlate early damage to a microstructural level. Overall, researchers concluded that AE activity is present during initial damage due to microcracks and dislocation movement, and various AE features can be correlated to damage.

Researchers studying AE over the past six decades have investigated how AE signals and their features correlate to microstructural damage. Some promising damage-related features include counts, count rate, amplitude, rise time, energy, and frequency. These features provide information about the structural damage measured by AE. Rather than using AE features as sources of information, one can rely on the actual information content, a scientifically defined term, carried within the signal. The measure of information, referred to as information entropy, from AE signals will be further investigated, and its effectiveness of detecting fatigue damage will be compared with commonly used AE features. In the following section, background and applications of information entropy will be summarized.

2.3 Information Entropy Background

2.3.1 Understanding Information Entropy

Entropy refers to the amount of disorder within a system. Often times, a reader's first exposer to entropy is to thermodynamic entropy which is the amount of energy not available to do work and related to temperature of a system. However, there are other forms of entropy including *information entropy*. Rather than having origins in thermodynamics, information entropy is founded on probability, statistical, and communication theory. Connections between information entropy and thermodynamic entropy have been researched, but no concrete conclusion has been

made [56]. Fundamentals of information theory and their applications can be found from several reference books [57, 58].

Information theory began in 1948 after Claude E. Shannon proposed limits on data compression for transmitting and recording communication signals in his paper, "A Mathematical Theory of Communication" [59]. Within this paper, he proposed information entropy, also referred to as Shannon entropy, as a measure of disorder or uncertainty in a message that is calculated based on Equation (2.4). In this equation, H is the information entropy, K is a constant that dictates the units, and $p(x_i)$ is the probability a certain value, x_i, present within the message with n possible values. It should be noted that the probabilities need to sum to 1 meaning a probability distribution should be defined for the signal. In addition, we will let $K = 1/\log(2)$ so that the logarithm will have a base of 2 to yield entropy in units of bits [58].

$$H = -K \sum_{i=1}^{n} p(x_i) * \log\ (p(x_i)) \tag{2.4}$$

To better understand the information entropy of a signal, it's best to see a few examples of calculating information entropy from various probability distributions. Two examples will be presented: 1) flipping fair and biased coins and 2) rolling fair and weighted dice. The examples are depicted in Figure 6 and Figure 7, respectively.

First, consider the probability distribution of flipping a fair coin where flipping heads or tails is equally likely. A person flipping this coin has little information and is very uncertain about whether the outcome will be heads or tails.

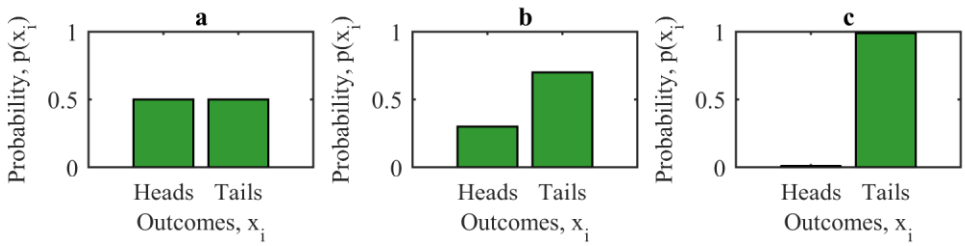

$$a.\ \ S = -\sum_{i=1}^{n=2} p(x_i)\log_2 p(x_i) = -0.5\log_2(0.5) - 0.5\log_2(0.5) = 1.00 \text{ bits}$$

$$b.\ \ S = -\sum_{i=1}^{n=2} p(x_i)\log_2 p(x_i) = -0.3\log_2(0.3) - 0.7\log_2(0.7) = 0.88 \text{ bits}$$

$$c.\ \ S = -\sum_{i=1}^{n=2} p(x_i)\log_2 p(x_i) = -0.01\log_2(0.01) - 0.99\log_2(0.99) = 0.08 \text{ bits}$$

Figure 6: a) Probability mass function (PMF) of flipping a fair coin and calculated information entropy. b) PMF of a biased coin with probability of flipping tails as 0.70 and calculated entropy. c) PMF of a biased coin with probability of flipping tails as 0.99 and calculated entropy.

Let heads be outcome x_1, tails be outcome x_2, and the probabilities for each outcome be $p(x_1) = 0.5$ and $p(x_2) = 0.5$. From this probability distribution, the information entropy can be calculated based on Equation (2.4). Subsequently, the entropy is found to be 1.000 bits. This is depicted in Figure 6a. Now consider a biased coin that results in tails 70% of the time. A person flipping the coin now has a bit more information and is less uncertain about the possible outcomes. A new probability distribution can be constructed to reflect the biased coin and the entropy of this distribution is less than before at 0.8813 bits as recorded in Figure 6b. Finally, consider a biased coin that is tails 99% of the time when flipped. A person flipping the coin is now almost certain that the outcome will be tails. This probability distribution is represented in Figure 6c and results in an even lower entropy of 0.0808 bits. This scenario exemplifies that more uniform probability distributions representing a highly disordered and more uncertain variable will result in a higher

value for information entropy. In other words, the greater the uncertainty and disorder, the greater the entropy will be.

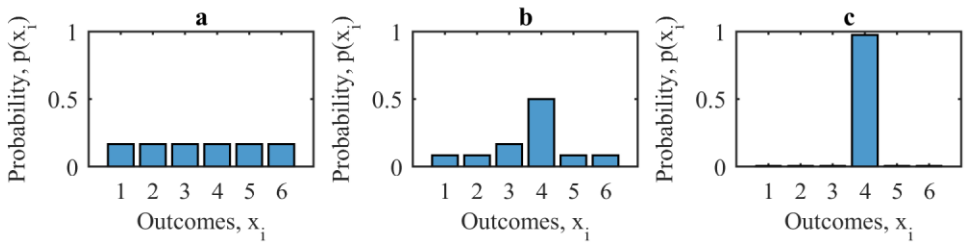

$$a.\ \ S = -\sum_{i=1}^{n=6} p(x_i)\log_2 p(x_i) = 2.59 \text{ bits}$$

$$b.\ \ S = -\sum_{i=1}^{n=6} p(x_i)\log_2 p(x_i) = 2.13 \text{ bits}$$

$$c.\ \ S = -\sum_{i=1}^{n=6} p(x_i)\log_2 p(x_i) = 0.23 \text{ bits}$$

Figure 7: a) PMF of a rolling a fair die and calculated information entropy. b) PMF of a weighted coin with greater probability of rolling a 4. c) PMF of coin 97.5% likely to result in a 4 and calculated entropy.

Similarly, one can see how information entropy varies with different probability distributions of fair and weighted dice. First, consider a fair die where rolling any number 1 through 6 is equally likely with probability of 1/6. This distribution is pictured in Figure 7a and results in an entropy value of 2.5850 bits. This value is greater than the entropy for a fair coin. This is because a die with 6 outcomes has greater disorder and uncertainty than a coin with 2 outcomes. Therefore, it can be concluded that the entropy value is dependent on the number of possible outcomes; when more outcomes are possible, entropy will be greater. Now, consider an unevenly weighted die that has the following probability distribution: $p(1) = p(2) = p(5) = p(6) = 1/12$, $p(3) = 1/6$, $p(4) = 1/2$ meaning 3 and 4 are more favored outcomes. The entropy calculated from this distribution is 2.1258 bits, a

lower value than if all outcomes were equally likely and reflects less disorder. This is shown in Figure 7b. Lastly, for a die that results in a 4 for 97.5% of the rolls, the person rolling is almost certain that the outcome will be a 4. Therefore, the entropy should be lower and is calculated to be 0.2267 bits as shown in Figure 7c.

In the end, given any variable or signal that is represented by a probability distribution, one can calculate information entropy using Equation (2.4) as a measure of the disorder or uncertainty carried within this signal. The maximum entropy will be from a distribution with equally likely outcomes while the minimum entropy of 0 bits will be from a distribution when only one outcome from a sample space is possible.

2.3.2 Application of Information Entropy to Fatigue and AE

The disorder measured by information entropy can be calculated from any probability distribution and has found applications in signal processing and communication [57, 60]. In addition, attempts have been made to apply information entropy techniques to fatigue damage.

Several studies have estimated fatigue damage models with information entropy since it is a measure of uncertainty. One common idea in the modeling field is the principle of maximum entropy referred to as MaxEnt. First pioneered by Jaynes [61, 62] in 1957, MaxEnt suggests that when selecting a model to fit a probability distribution, the one that best represents the current knowledge is the one with maximum entropy. The model with maximum entropy is the one with the most uncertainty, is the “least biased given the information”, and “is maximally noncommittal with regard to missing information” [61]. Recently, fatigue damage

prognosis models with limited or uncertain data have been developed by utilizing the MaxEnt principle and Bayesian inference with much success [63, 64, 65].

Other researchers have implemented information entropy techniques to estimate structural damage unrelated to MaxEnt. Li [66] identified damage in infrastructure using artificial neural networks, Dempster-Shafer evidence theory, and information entropy. Unlike MaxEnt, Li selected decisions within the neural network that had smallest entropy and the lowest uncertainty. In the end, the accuracy improved when this information entropy technique was employed. Another study [67] implemented information entropy in order to estimate optimal maintenance time of pipeline systems. For a new pipe, the maximum pressure the pipe can accommodate is often known with little uncertainty. As a pipeline corrodes, however, the burst pressure decreases and the uncertainty about this critical value increases. In turn, information entropy was used to measure this uncertainty and led to deriving the optimal maintenance intervals during instances with maximum entropy.

So far, several papers have been presented that use information entropy as a measure of model uncertainty in structural damage prognosis. These methods, however, do not measure the disorder within a structure that is subjected to damage but only model uncertainty. First, microstructural disorder should be defined in terms of fatigue damage.

As previously explained, fatigue damage progresses as dislocations move and create microcracks near inclusions which coalesce to form macrocracks. A structure with minimal damage prior to fatigue loading would then have a series of defects. These defects and microcracks are considered to be disorder within the structure and

thus, fatigue damage will be synonymous with microstructural disorder throughout this work. This correlation is exemplified in Figure 8 where microstructural disorder is equated to fatigue damage. Initially, a metallic material has minimal defects among its grains, inclusions, and precipitates. Then, as more cyclic stresses are applied, inclusions crack, microcracks nucleate, and microcracks coalesce to form macrocracks. In the end, the microstructural disorder increases as fatigue damage increases and is attempted to be quantified by AE signals in this work as well as in previous studies.

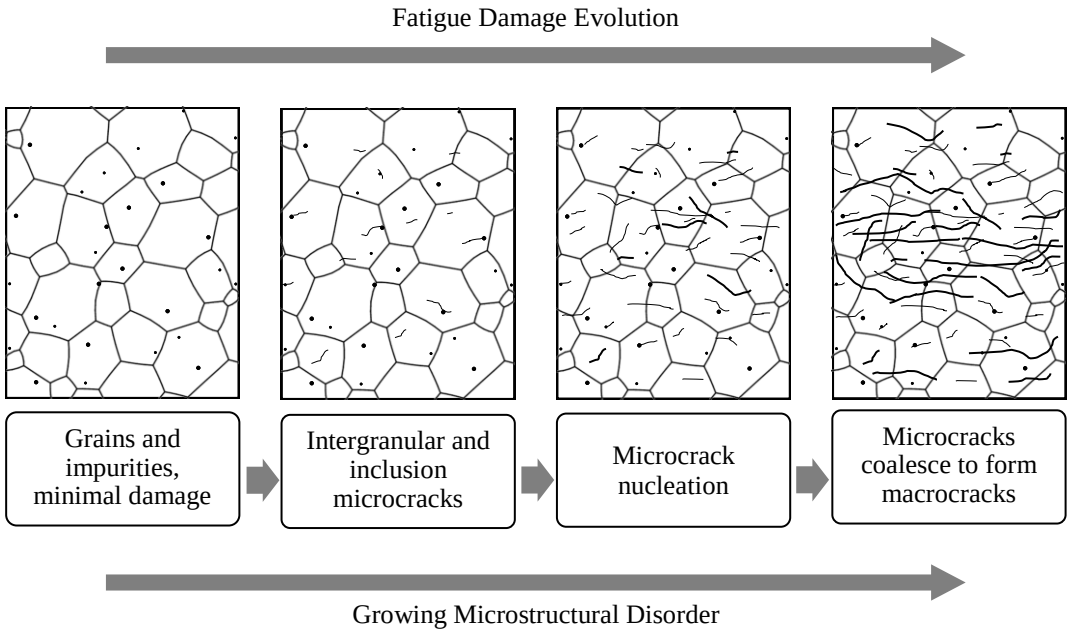

Figure 8: Microstructural disorder as defined by fatigue damage evolution

A few researchers have looked into estimating information entropy of AE signals during fatigue experiments. Unnthorsson and coworkers [68] estimated two time-domain entropies and two frequency-domain entropies from AE signals recorded during composite fatigue tests. The entropies were calculated from discrete probability distributions of the amplitude and frequency measured for 1 fatigue cycle

every 5 minutes of testing. In the end, the entropy evolutions were similar to AE count trends, and it was proposed that entropy from AE signals could be used a measure of microstructural disorder.

Qi [69] also focused on deriving entropy from AE amplitude distributions to be used as a measure for microstructural damage. Tensile tests were performed on various cements and the updating distributions of AE amplitudes for recorded signals were used when calculating entropy. In this study, the entropy value was calculated based on Equation (2.4) without the negative coefficient before the summation. Therefore, entropy values were reported as negative with a minimum possible value of -2.3 when all AE signals are of a single amplitude and a maximum value of 0 when amplitudes are uniformly distributed. Results showed that the entropy from the AE amplitude spectrum became less negative as the stress increased and then remained constant or decreased slightly near fracture. This is because AE signals often have low amplitudes initially and then more signals at various and higher amplitudes are recorded as damage progresses. Thus, this study proved that measured disorder from AE amplitude distributions increases as damage also increases.

Modarres and coworkers [70,71] built off of these studies to estimate entropy from AE counts during fatigue tests of aluminum and titanium alloys. Results showed that information entropy derived from counts mirrored the evolution of counts throughout the test [70], and the cumulative information entropy from counts may be constant at failure [71]. The commonality between this research and Unnthorsson's and Qi's work is that the entropy was calculated from AE feature distributions over certain intervals of time where several AE signals have been collected. Rather than

using features from several AE hits at a time, one could look at the amplitude distributions of each individual AE waveform. This method would theoretically utilize more information carried in an AE signal compared to summary statistics like the number of counts, the peak amplitude, or the average frequency. This is the fundamental basis of this thesis; to extract information entropy from every individual AE signal during fatigue tests in order to estimate damage evolution. The effectiveness of this method to detect damage both prior to and after an observable crack will be explored.

Three different topics were reviewed in this chapter in regards to background and previous literature; fatigue damage in metals, acoustic emission methods and instrumentation, and information entropy as a measure of uncertainty and disorder. The following chapter details the experimental procedure in order to measure the fatigue damage and information entropy from AE signals.

Chapter 3 – Experimental Procedure

3.1 Specimen Preparation

Specimens used for this study were aluminum alloy 7075-T6 referred to as Al7075-T6 throughout this work. This specific alloy is used in aerospace structures such as stringers, skins, bulkheads, rivets, and extruded sections [3]. The supplied material from Kaiser Aluminum came from the same lot number ensuring maximum microstructural continuity between all fatigue specimens. The material's composition and mechanical properties were provided by the manufacturer and presented in Table 4. To confirm the mechanical properties such as elastic modulus, yield strength, ultimate yield strength, and percent elongation, two tensile tests were performed. Results from these tests implied that the specimens may have slightly higher strength and more ductility than reported by the manufacturer.

Table 4: Composition and mechanical properties for Al7075-T6

Element	Al	Zn	Mg	Cu	Cr	Fe	Mn	Si	Ti	V	Zr	Other
Composition (wt %)	89.72	5.7	2.6	1.4	0.20	0.15	0.08	0.06	0.02	0.01	0.01	0.05

Material Property	Ultimate Strength (MPa)	Yield Strength (MPa)	% Elongation	Modulus of Elasticity (GPa)
Manufacturer-Provided Value	579	513	13.7	Not given
Measured Value from Tensile Tests	587	538	24.0	67.8

The raw material was machined into specimens designed according to ASTM standard E466 [72]. Several iterations of the geometries were performed in order to accommodate an extensometer, sensors, and mechanical damping apparatus, which will be explained in subsequent sections. In the end, five different geometries were designed until the final design was selected. The dimensioned geometry is shown in

Figure 9. A 1 mm radius edge notch is located at the center of the gauge length and acts as a stress concentrator. This intentional flaw ensures that fatigue damage and crack initiation will occur at this location. Based on a stress concentration handbook [73], the stress concentration factor of the notch is estimated to be 2.61. Within this work, the specimens are referred to as 5A1 through 5A26 where 5 represents the geometry iteration number, A means the grain direction is parallel to loading direction (as opposed to B which means the grain direction is perpendicular to loading direction), and the proceeding numbers are the specimen numbers.

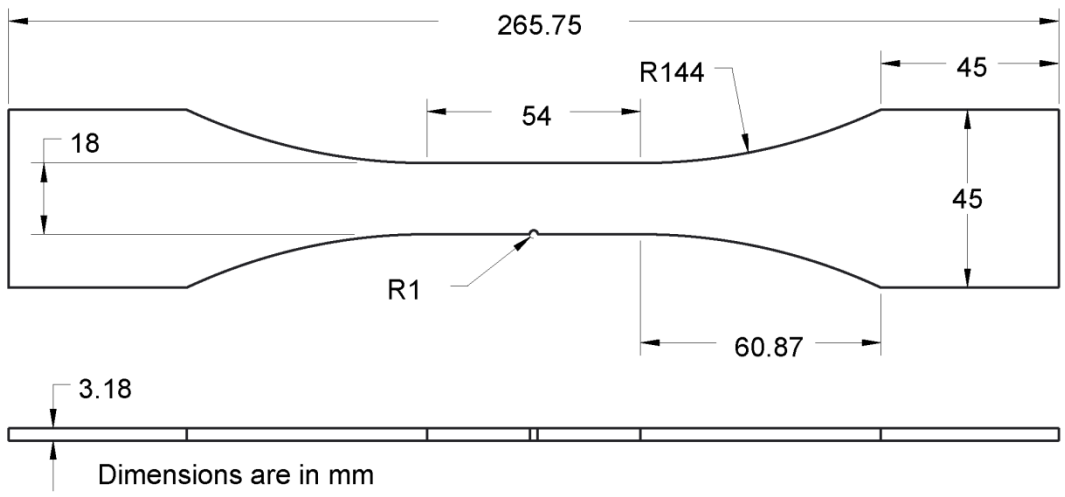

Figure 9: Fatigue specimen geometry

Once the specimens were machined, one side of the specimen's gauge length was polished so that grain boundaries could be seen under an optical microscope. In addition, crack initiation is influenced by surface roughness so it is best to ensure all specimens had similar surface roughness values. The polishing process began by sanding the surface with 1000 grit sandpaper followed by 2000 and 3000 grit sandpaper. Then a 3 µm alumina solution was used followed lastly by etching the surface with Keller's etchant solution. In turn, the grain boundaries could be seen

clearly under magnification. The distribution of the grain sizes were estimated by measuring the area of 125 grains from three dogbone specimens and deriving the average diameter for the total 375 grains. Figure 10 displays the distribution where the grains varied between 0.04 mm and 0.27 mm with a mean of 0.124 mm and standard deviation of 0.037 mm. According to ASTM standard E112-12 [74], the grain size number is approximately 3.0.

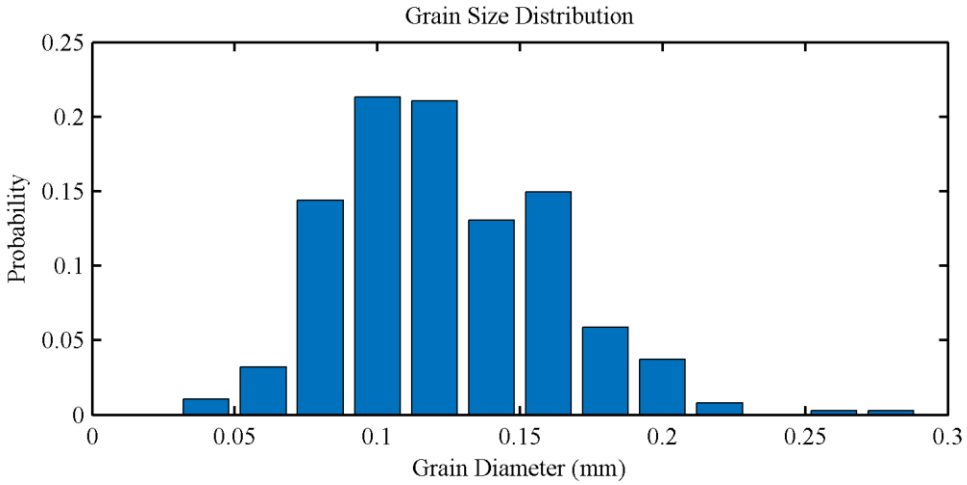

Figure 10: Probability distribution of grain diameter for 375 measured grains

3.2 Loading Conditions

A servo-hydraulic Materials Testing System (MTS) machine retrofitted with an Instron 8800 controller was used to perform the fatigue tests. The machine's maximum load is 100 kN and the load cell used has an uncertainty between 0.13% and 0.54% of the applied load. A computer connected to the load frame is used to specify the loading conditions within the WaveMatrix software program. The load frame is pictured in Figure 11.

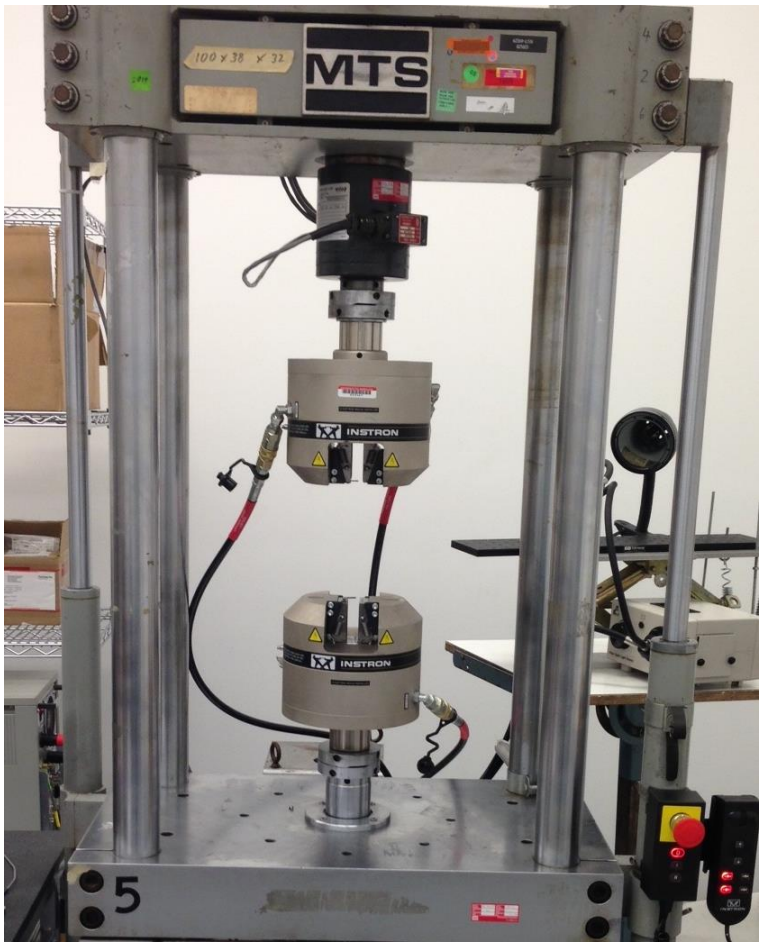

Figure 11: Servo-hydraulic MTS machine

A total of 26 tension-tension fatigue experiments were performed with loading ratio of 0.1 and loading frequency of 5 Hz. The maximum applied load varied between 8 and 15 kN in order to see the differences between low-cycle and mid-cycle fatigue on detecting microstructural damage prior to a visible crack. The theoretical maximum applied stress can be estimated by dividing the load by the gauge-length cross-sectional area, 57.15 mm^2, and multiplying by the stress concentration factor, 2.61. The maximum applied load and estimated applied stress at the notch for each experiment is listed in Table 5. Similarly, the tests for each loading condition are listed in Table 6.

Table 5: Loading conditions for each experiment

Specimen Name	Max. Applied Load (kN)	Est. Notch Stress (MPa)
5A1	13	593.7
5A2	12	548.0
5A3	11	502.4
5A4	11	502.4
5A5	10	456.7
5A6	10.5	479.5
5A7	9	411.0
5A8	10.5	479.5
5A9	10.5	479.5
5A10	11	502.4
5A11	13	593.7
5A12	9	411.0
5A13	9	411.0

Specimen Name	Max. Applied Load (kN)	Est. Notch Stress (MPa)
5A14	8	365.4
5A15	12	548.0
5A16	12	548.0
5A17	8.5	388.2
5A18	8.5	388.2
5A19	14	639.4
5A20	15	685.0
5A21	10	456.7
5A22	13	593.7
5A23	9	411.0
5A24	12	548.0
5A25	9	411.0
5A26	10	456.7

Table 6: Experiments for each loading condition

Max. Applied Load (kN)	Est. Notch Stress (MPa)	Specimen Names
15	685.0	5A20
14	639.4	5A19
13	593.7	5A1, 5A11, 5A22
12	548.0	5A2, 5A15, 5A16, 5A24
11	502.4	5A3, 5A4, 5A10
10.5	479.5	5A6, 5A8, 5A9
10	456.7	5A5, 5A21, 5A26
9	411.0	5A7, 5A12, 5A13, 5A23, 5A25
8.5	388.2	5A17, 5A18
8	365.4	5A14

However, it was found that a crack grew away from the notch for low loading conditions. Crack initiation location can be determined based on the brittle regions of a crack's surface. A crack will initiate and grow due to brittle fracture until the crack reaches unstable growth where ductile failure will occur. Figure 12a shows the crack surfaces of 5A26 that properly failed at the notch while Figure 12b depicts 5A18 crack surfaces that failed away from the notch. It can be seen the brittle region for 5A26 is at the edge of the notch while the brittle region for 5A18 was near the specimen's face. This finding suggests the maximum stress was in fact at the face rather than at the notch.

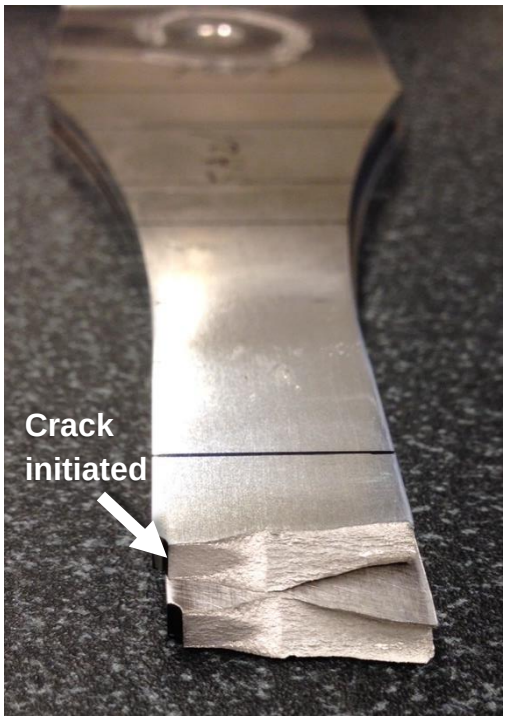

Figure 12a: Crack initiated as expected at notch edge for 5A26

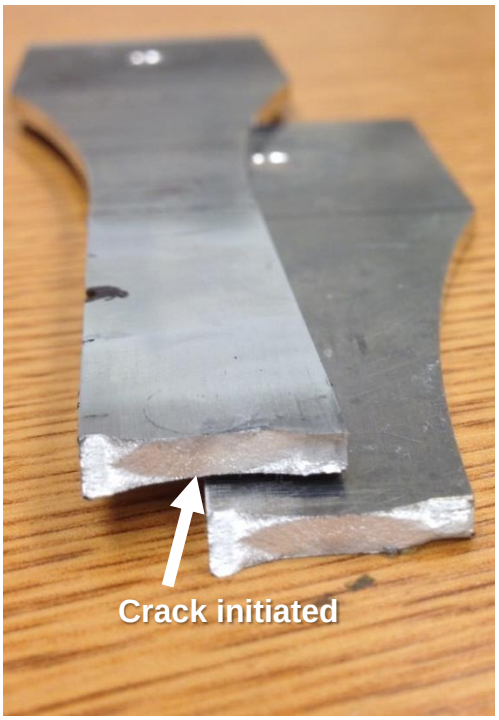

Figure 12b: Crack initiated unexpectedly at specimen face for 5A18

Figure 12: Crack surfaces for 5A26 and 5A18

One possible reason to explain this anomaly is that there seems to be is a slight misalignment between the testing grips which most likely applies a small bending moment on all specimens. At higher axial loads, the notch is the predominant stress concentrator and the bending moment has little effect on crack growth location. However, when the axial loading is low, the bending moment causes a greater stress then the notch. The experiments that failed away from the notch (5A14, 5A17, 5A18) are marked in Table 9 and were discarded.

3.3 Strain Measurement

In order to measure the strain around the edge notch, an extensometer was used. The Epsilon 3542 extensometer has a gauge length of 25 mm, and can measure between -10% and 10% strain. For the first 3 experiments (5A1, 5A2, 5A3), the

extensometer slipped slightly on the specimen because it was not securely fastened. In order to prevent this sliding or rubbing during testing, rubber bands were used to fasten the extensometer to the specimen for subsequent experiments. The extensometer slipped for a few subsequent experiments (5A4, 5A6, 5A10, 5A13). In addition, the extensometer was not applied for 4 other tests (5A8, 5A9, 5A11, 5A12) and confirmed that unusual AE signals were not due to the extensometer sliding on the surface. These tests are also marked in Table 9. One drawback to the extensometer is it measures the strain over 25 mm of gauge length as opposed to exactly and only the area around the notch. Because the notch acts as a stress concentrator, most of the deformation is expected to be around the notch, but the extensometer measures a greater area. In turn, the extensometer is assumed to be less sensitive than a strain measurement technique that is more localized.

Other techniques to measure strain were also investigated. First, strain gauges were used and placed near the middle of the notch. While the strain gauges seemed to be quite accurate and had the ability to measure localized strain around the notch, the gauges were susceptible to detaching from the specimen as a crack initiated and grew. In addition, as soon as a strain gauge began to detach, unwanted AE signals were produced. Another technique tested for its effectiveness was Digital Image Correlation (DIC). DIC calculates strain based on how a surface pattern changes on a loaded structure due to applied stress. While this technique had the potential to measure strain around the notch more closely than the extensometer and not cause AE noise signals, the image processing speed of the DIC system used was too slow to capture strain accurately and frequently. Fatigue tests were performed at 5 Hz and the

maximum sampling rate of the available DIC was 10 Hz meaning at most 2 measurements of strain were saved per cycle. For this testing, a 10 Hz strain sampling rate was too low compared to the 200 Hz extensometer sampling rate. In addition, the DIC prevented the optical microscope from being used to capture crack initiation and growth. Compared to the optical microscope images, the DIC images of crack initiation were far less clear. The advantages and disadvantages of the strain measurement techniques are summarized in Table 7.

Table 7: Strain measurement techniques and associated attributes. Advantages are in green, disadvantages are in red.

	Extensometer	Strain Gauge	DIC
Strain region around notch	+/- 12.5 mm	+/- 1mm or greater	+/- 1 mm and greater
Sampling rate	High, 200 Hz used	High, 200 Hz used	Low, less than 10 Hz
Measure strain through crack initiation?	Yes	No	Yes
Effect on AE	No to little interference	High interference	No interference
Effect on crack monitoring	No interference	No interference	High interference

3.4 Crack Monitoring System

In order to monitor the initiation of a crack and its growth, an optical microscope with an attached time-lapse camera captured images throughout testing. An external Meiji dual-arm fiber optic light source illuminated the specimen. The microscope encompassed about a 1.5 mm by 2.0 mm area around the notch where a circular segment of the notch is shown on the left side of each image. In order to measure the small crack length, ImageJ software was used to estimate the picture scales (the number of pixels per millimeter) and the number of pixels the crack spanned based on the circular segment. The geometric relationship between the radius, chord length, and height of the segment was employed to estimate the picture scales. This relationship is depicted in Figure 13. By measuring the chord length, c,

and height of the segment, h, in pixels, the radius in pixels can be estimated. Since the radius is known to be 1 mm, the picture scale can therefore be estimated using Equation (3.1). Finally, crack length is then measured in millimeters by measuring the number of pixels spanned and converting to millimeters with the picture scale.

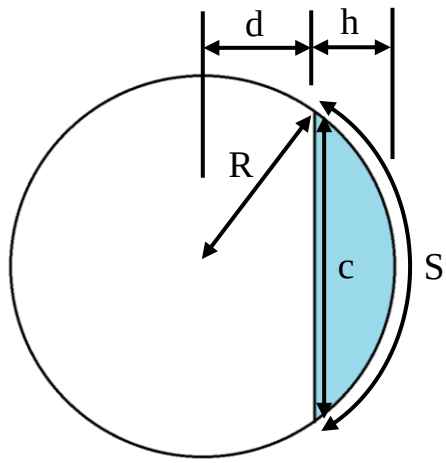

Figure 13: Circular segment dimensions

$$Picture\ Scale = \frac{R\ in\ pixels}{R\ in\ mm} = \frac{\left(\frac{c^2}{8h}+\frac{h}{2}\right) pixels}{1\ mm} \tag{3.1}$$

Pictures were taken every 5 seconds. However, because the specimen was moving during cyclic fatigue loading, about one-half of the images were too blurry and had to be discarded. Figure 14 shows four typical images captured from the optical microscope. Figure 14a shows the area around the notch before cyclic loading was applied. Figure 14b and Figure 14c show slightly blurry and very blurry images, respectively, during the fatigue process before a crack initiated. Finally, Figure 14d is an image once a crack has grown. The crack monitoring system worked well except for one test (5A5) in which the camera stopped recording images. This experiment is marked in Table 9**.**

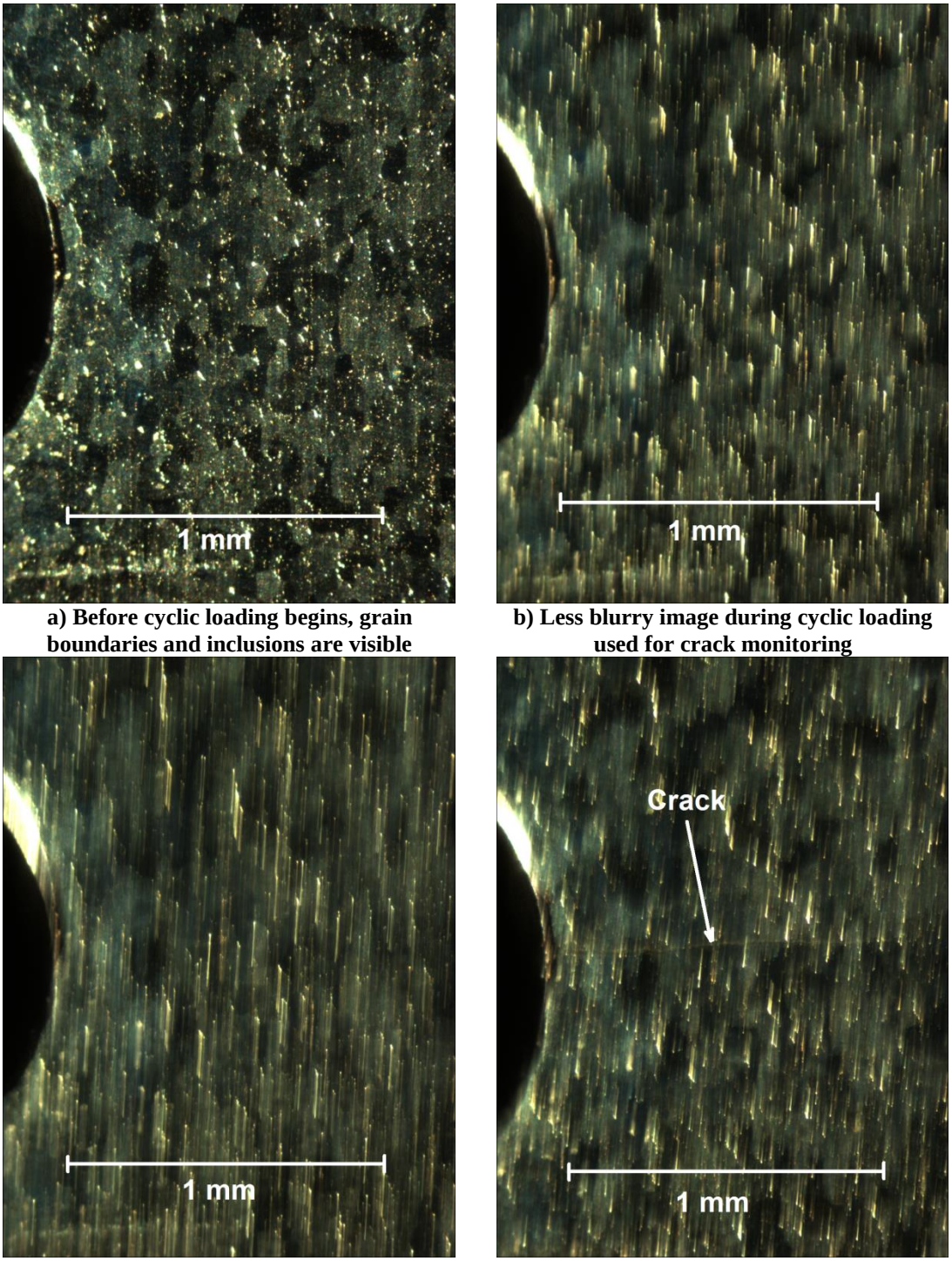

a) Before cyclic loading begins, grain boundaries and inclusions are visible

b) Less blurry image during cyclic loading used for crack monitoring

c) Very blurry image that cannot be used

d) Image after crack has initiated

Figure 14: Optical microscope images during fatigue of specimen 5A26

3.5 Acoustic Emission Instrumentation

AE signals were recorded with a PCI-2 Based AE system supplied by the MISTRAS Group. Two resonant Micro30s AE sensors with a frequency range of 150-400 kHz and resonant frequency of 225 kHz were used. The sensors were mounted to one side of the specimen 23 mm above and below the center of the notch. Ultrasonic gel was used as a couplant, and electrical tape fastened the sensors to the surface. The AE signals passed through a 40 dB preamplifier before reaching the data acquisition module where AEwin software then plotted and extracted the AE signals. The AE acquisition system also received load and extension data as analog inputs from the testing machine. This feature enabled the AE signals to be paired with the applied load and is crucial to post-process filtering. AE signals are recorded as voltage values ranging between -10 and +10 volts with smallest divisions of 0.000305 volts. Other user-defined settings that control how the AE signals are collected are summarized in Table 8. These parameters were selected based on pencil lead break tests [75], a common standard that produces repeatable artificial AE waves with similar characteristics to damage-related AE signals.

Table 8: AE software settings

Parameter	Value
Peak definition time (PDT)	300 µs
Hit definition time (HDT)	600 µs
Hit lockout time (HLT)	1000 µs
Sampling rate	1 MSPS

Parameter	Value
Pre-trigger length	256 µs
Hit length	2048 µs
Band pass filter	1 kHz – 3 MHz

3.6 Mechanical Damping Apparatus

3.6.1 Why Mechanical Damping?

A crucial part of the fatigue experiments is collecting AE signals. One of the first AE settings to be prescribed is the amplitude threshold. As previously explained,

only AE signals that exceed the threshold will be collected, and the threshold should be set to slightly above the noise amplitude. During initial experiments, the background noise reached amplitudes of 65 dB. Typically, an acceptable AE threshold is about 45 dB while lower thresholds of 40 dB or 35 dB are desirable. In this case, the threshold would have had to be greater than 65 dB meaning most, if not all, AE damage signals would not be detected.

Servo-hydraulic machines are known to produce AE background noise of similar frequency and amplitude to damage-related AE signals making filtering the noise a difficult process. Researchers have filtered noise based on signal arrival times [51, 54] and on frequency [35, 52], but neither of these methods proved effective for this particular test setup. Instead, attempts were made to actively limit the noise signals from propagating through the specimens. In turn, a mechanical damping apparatus inspired from Miller's work [76] and numerous damping configurations was designed.

3.6.2 Damping Techniques

When a specimen was fixed to the machine and AE was recorded, the AE amplitude seemed to decrease when two fingers pinched the specimen. In addition, Dr. Ron Miller, an expert in AE and former engineer at the MISTRAS Group, implemented a damping technique for servo-hydraulic fatigue tests during his graduate work at Purdue University [76]. Thus, fastening damping materials to the specimen seemed to be a promising method. Several different configurations and materials were tested and the AE background noise amplitude was observed. In the

end, the specimen geometry was altered several times to allow sufficient room for damping material and a final damping design was selected.

The final apparatus consists of four sets of clamped, 1/4" thick, styrene-butadiene rubber blocks and four tightly-wrapped, 1/16” thick, neoprene strips attached to areas between the testing grips and specimen gauge length. These elastomers inhibit mechanical vibration and reduced the background noise to below 41 dB for an AE sensor attached on the surface above the notch allowing for a threshold of 45 dB. For these experiments, a second AE sensor was attached on the surface below the notch but experienced noise of 45 dB and the threshold had to be set slightly higher than 45 dB. Only AE signals from the upper sensor were analyzed while the AE signals from the lower sensor were used to validate the upper sensor’s behavior. The amplitude spectrum during 20 seconds of recorded AE noise signals with and without the damping material is depicted in Figure 15 showing a 20 dB decrease in noise amplitude.

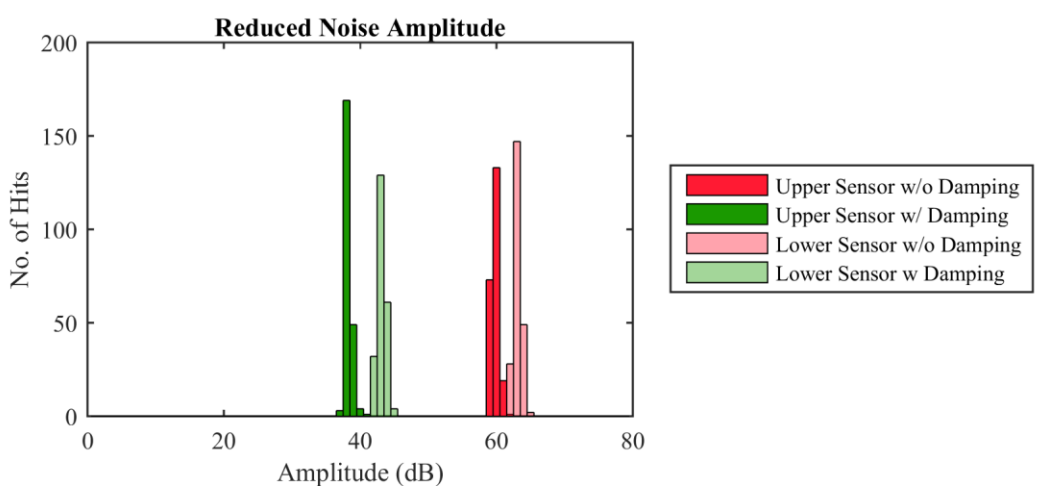

Figure 15: AE noise amplitude with and without mechanical damping

The schematic of the damping apparatus on the specimen is pictured in Figure 16a, and the entire test setup is depicted in Figure 16b. In addition, several of the first

experiments did not have the final damping apparatus applied but instead preliminary iterations. Therefore, the damping configurations initially used did not damp the noise amplitude to below 45 dB and the threshold was set to values ranging between 46 and 52 dB. Table 9 lists the AE threshold values applied for each test.

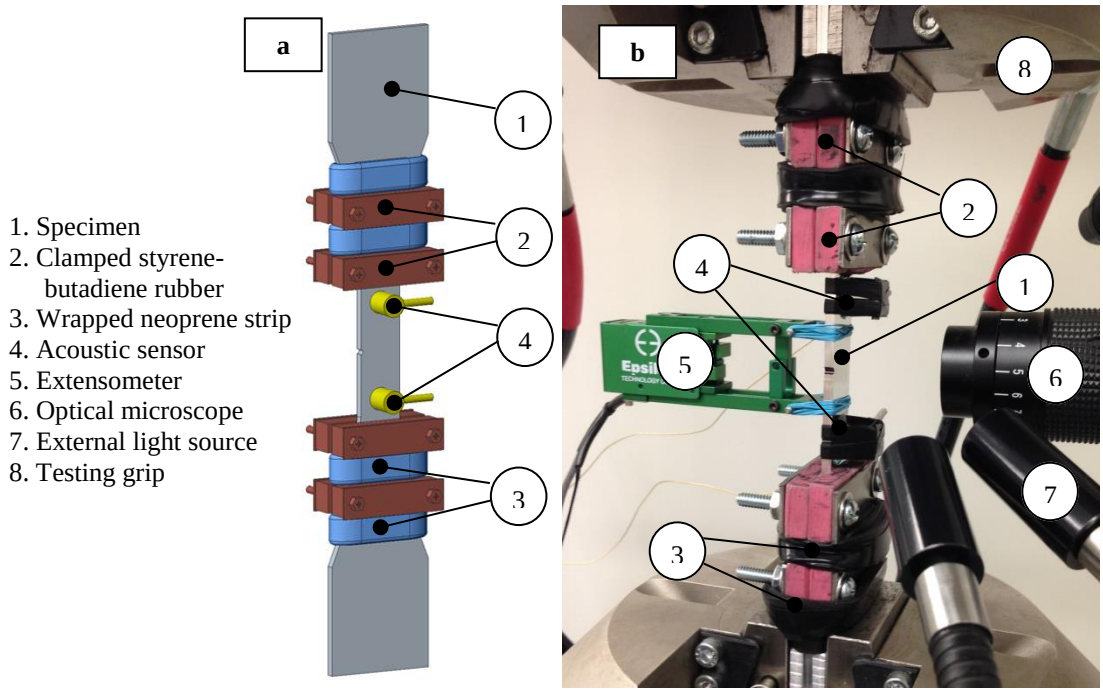

Figure 16: a) Mechanical damping method. b) Complete experimental setup.

In the future when an AE sensor system is developed for NDE of aircraft structures, reducing and filtering the noise will inevitably be a problem that would need to be solved. In these experiments, the noise was damped by constraining material away from the inspection sites with viscoelastic materials. Likewise, the use of dampers may have to be considered to effectively use AE as an NDE technique.

3.7 Details of Individual Fatigue Experiments

Of the total 26 experiments, several had slightly different experimental setups. Three specimens failed away from the notch during low loading, eleven experiments

did not have the extensometer fastened securely or was not attached, and the optical microscope camera failed to record images for one experiment. These 15 experiments were discarded and not used in data analysis. In addition, because of the damping apparatus iterations, the AE threshold setting varied for initial experiments. The AE threshold has an effect on AE results, but tests with an AE threshold greater than 45 dB are discarded due to extensometer performance. The details for each experiment are noted in Table 9.

Table 9: Experiment details. Tests with any detail in red are discarded.

Specimen Name	Max. Applied Load (kN)	Est. Notch Stress (MPa)	Crack Location	Extensometer performance	Images of Crack?	Upper Sensor AE Threshold
5A1	13	593.7	Notch	Slipped	Yes	52 dB
5A2	12	548.0	Notch	Slipped	Yes	52 dB
5A3	11	502.4	Notch	Slipped	Yes	52 dB
5A4	11	502.4	Notch	Slipped	Yes	46 dB
5A5	10	456.7	Notch	Nominal	No	48 dB
5A6	10.5	479.5	Notch	Slipped	Yes	48 dB
5A7	9	411.0	Notch	Nominal	Yes	47 dB
5A8	10.5	479.5	Notch	Not attached	Yes	46 dB
5A9	10.5	479.5	Notch	Not attached	Yes	47 dB
5A10	11	502.4	Notch	Slipped	Yes	47 dB
5A11	13	593.7	Notch	Not attached	Yes	47 dB
5A12	9	411.0	Notch	Not attached	Yes	47 dB
5A13	9	411.0	Notch	Slipped	Yes	47 dB
5A14	8	365.4	Grip	Nominal	Yes	47 dB
5A15	12	548.0	Notch	Nominal	Yes	48 dB
5A16	12	548.0	Notch	Nominal	Yes	45 dB
5A17	8.5	388.2	Extensometer	Nominal	Yes	45 dB
5A18	8.5	388.2	Sensor	Nominal	Yes	45 dB
5A19	14	639.4	Notch	Nominal	Yes	45 dB
5A20	15	685.0	Notch	Nominal	Yes	45 dB
5A21	10	456.7	Notch	Nominal	Yes	45 dB
5A22	13	593.7	Notch	Nominal	Yes	45 dB
5A23	9	411.0	Notch	Nominal	Yes	45 dB
5A24	12	548.0	Notch	Nominal	Yes	45 dB
5A25	9	411.0	Notch	Nominal	Yes	45 dB
5A26	10	456.7	Notch	Nominal	Yes	45 dB

Chapter 4 – Post-Processing Methods

4.1 Noise Reduction

Despite reducing the AE background noise to amplitudes below 45 dB with the mechanical damping method, it became evident during the 26 experiments that AE noise signals were still collected during some tests. Again, even though others have had success filtering AE signals based on frequency and arrival times [35, 51, 52, 54], this technique proved ineffective. Instead, another filtering technique based on applied load at the instant of AE signals was implemented. AE signals are emitted due to fatigue damage, and it is assumed that the AE signals will most likely occur when a structure is applied with maximum stress [28, 34, 36, 52]. For a fatigue cycle with minimum load of 1 kN and maximum load of 10 kN, this means that an AE signal would tend to occur between 7 and 10 kN rather than 1-7 kN. Five cycles with instances of potential AE hits are depicted in Figure 17 with hits marked in red to be likely AE hits and those in blue to be unlikely.

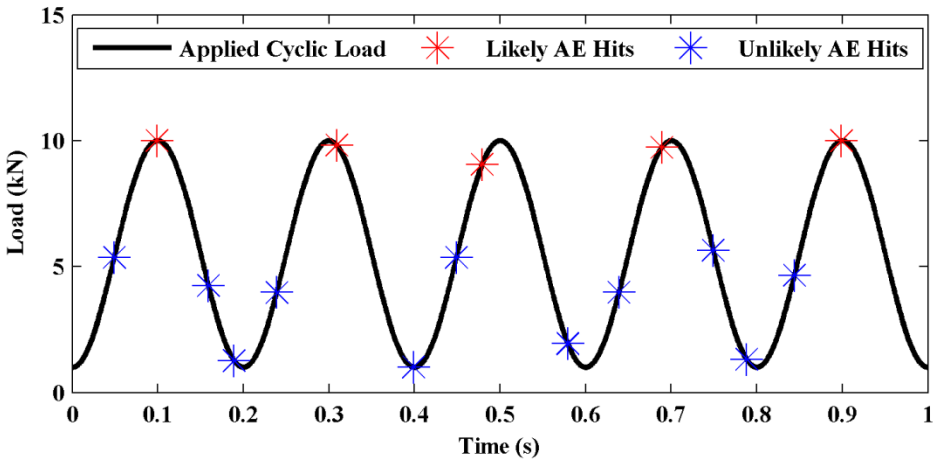

Figure 17: Likely and unlikely AE hits based on applied load

Of the 11 experiments that had no errors in regards to extensometer performance, crack monitoring, or crack location, AE signals were inspected for unwanted noise signals based on load. The expected AE signal behavior can be described in accordance with the stages of fatigue damage. First, the initial few fatigue cycles are assumed to cause sudden dislocation realignment within the structure which emit a few AE events. These events, while likely to occur during the upper half of the loading cycle, are often sporadic and can occur at any point in a loading cycle. Then, fatigue damage continues to progress and is believed to cause sparse and erratic AE signals at various applied loads. Eventually, the accumulated microstructural damage will result in a crack initiating and growing at an unstable rate. During this stage, more AE signals are expected to occur especially at high loads. Finally, several hundreds of AE signals are anticipated as a crack grows towards final fracture. This final series of hits can occur at any load because a crack can grow at any applied stress once it reaches a certain length and crack surfaces rub against one another during unloading.

Two of the 11 “good” experiments (5A25 and 5A26) exhibited the expected AE behavior with no apparent noise signals. The AE signals at the associated applied load are shown as red points in Figure 18 for one of these experiments, 5A26. AE signals occur sporadically and at various loads for the first three-quarters of fatigue life. These signals are most likely due to dislocation stacks unpinning and suddenly releasing stored strain energy. Damage continues to grow and more AE signals are recorded at high loads as a crack initiates. Then, AE signals occur at both high loads and middle-low loads during crack growth and specimen fracture.

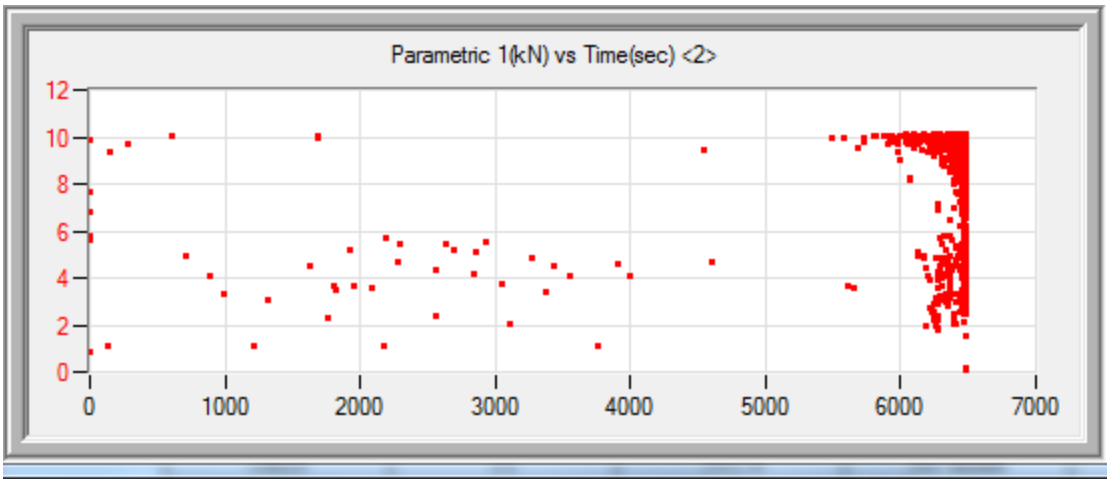

Figure 18: AE signals at their associated loads versus time for 5A26. No apparent AE noise.

The other 9 experiments of the 11 "good" tests showed both the expected AE behavior and another behavior that is believed to be unwanted noise. This unwanted behavior is characterized by AE signals continuously occurring at mid-range loads forming clusters when plotted against their associated load and arrival time. These clusters suggest either strain energy is released consistently away from the maximum load or that mechanical noise is generated at certain points of the loading cycle. The latter is assumed to be more likely, and therefore, these signals should be excluded. A possible cause of the mechanical noise could be the servo-hydraulic piston rubbing against another component or changes in piston acceleration at specific points during a loading cycle. This phenomenon could develop later in a fatigue test and then dissipate resulting in clusters or trends on AE associated applied load versus arrival time scatter plots.

Of the 9 experiments tainted with AE noise signals, seven could be filtered (5A16, 5A19, and 5A21–5A24). The scatter plot of applied load at the instant of AE signals and their arrival times for one such test, 5A22, is pictured in Figure 19. Too many noise signals were recorded for the other three tests (5A7, 5A15, and 5A20) and

the expected AE behavior and noise could not be confidently differentiated. Figure 20 shows the applied load at AE hits versus time for 5A20 as an example of noise that proved impossible to separate from the assumed damage-related AE hits. Scatter plots of AE signal arrival time and associated applied for all 11 of these tests are given in Appendix A – Applied Load vs. Signal Arrival Time Scatter Plots.

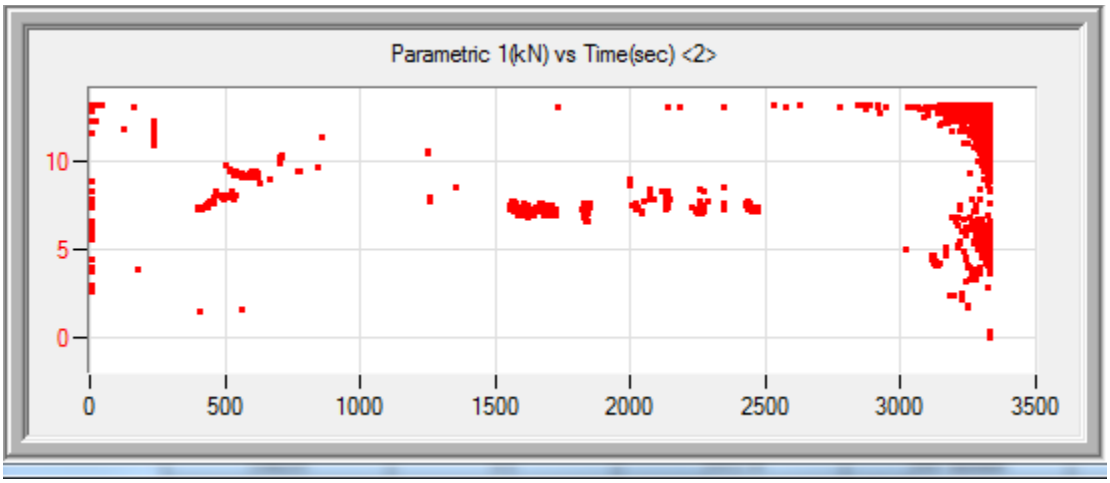

Figure 19: Applied load at instant of AE signals at their arrival times for 5A22. Filterable noise.

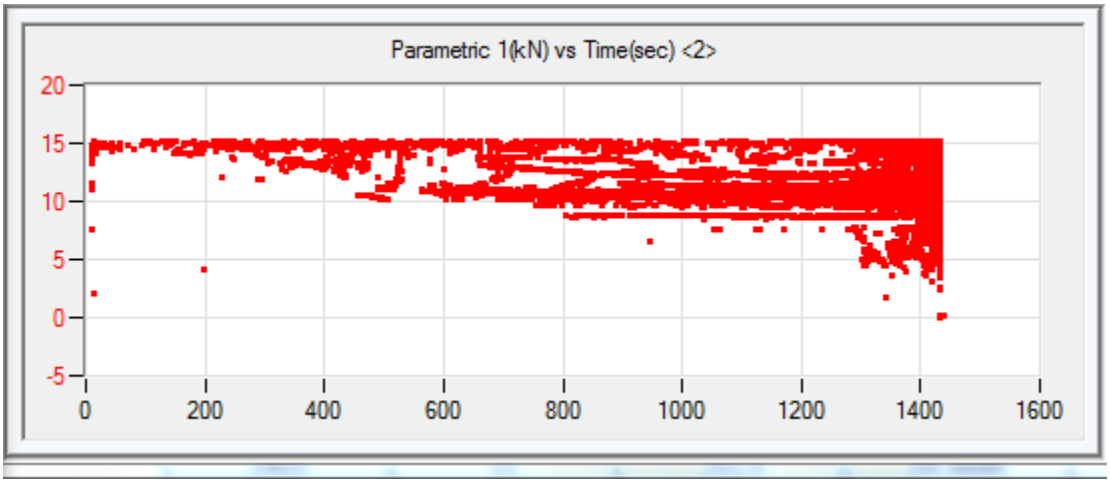

Figure 20: Applied load at recorded AE signals and their arrival times for 5A20. Unfilterable AE noise.

Table 10 lists the 11 tests with no previous experimental errors and summarizes the recorded AE signal behaviors. The table also notes the number of AE signals collected from the upper AE sensor for tests with no noise and tests after possible filtering. Each test with no or filterable noise has less than 2700 AE signals

while tests that were not filtered had more than 22,000 signals. Therefore, it is believed that at least 87% of the signals from the unfilterable tests were due to noise.

Table 10: AE noise behavior for each test with an acceptable test setup

Specimen Name	Max. Applied Load (kN)	Est. Notch Stress (MPa)	AE Noise?	No. of AE Signals Collected
5A7	9	411.0	Unfilterable noise	160024
5A15	12	548.0	Unfilterable noise	55445
5A16	12	548.0	Filterable noise	2108
5A19	14	639.4	Filterable noise	1915
5A20	15	685.0	Unfilterable noise	22087
5A21	10	456.7	Filterable noise	2617
5A22	13	593.7	Filterable noise	1222
5A23	9	411.0	Filterable noise	2311
5A24	12	548.0	Filterable noise	2403
5A25	9	411.0	No noise	1478
5A26	10	456.7	No noise	1865

Of course, significant assumptions were made during the filtering process. Other researchers may disagree with whether specific AE signals should be attributed to noise or are in fact damage related. However, the filtering method was kept consistent in that clusters of AE signals at low loads were removed. Tests that would have required questionable noise filtering were discarded.

4.2 Instantaneous Elastic Modulus Calculations

Another post-processing step to perform is to estimate the elastic modulus for each fatigue cycle. Crack length is the common metric for fatigue damage. However, the goal of this work is to estimate damage prior to an observable crack where microscopic cracks are unnoticeable during fatigue loading even with the aid of an optical microscope. Microstructural damage could be accurately quantified if fatigue loading was repeatedly interrupted and the notch was examined under higher magnification. This is undesirable though because many testing conditions could differ including specimen alignment, precise AE sensor location, and AE background

noise behavior. Instead, it is assumed that structural degradation is reflected as a decrease in the structure's elastic modulus. Dislocations move and microcracks grow such that the material becomes less stiff and will elongate more for the same applied load as fatigue loading progresses. Initial moduli values are expected to differ slightly between specimens but should all be near the anticipated elastic modulus of 67.8 GPa as noted in Table 4. Despite variations, a consistent modulus decline and degradation trend between specimens is expected.

The modulus degradation is approximated by Equation (4.1). Here, E is the modulus, ΔP is the difference between the maximum and minimum applied load, L_o is the extensometer gauge length, Δl is the difference between the extension at the maximum and minimum loads, and A is the cross-sectional area. The MATLAB code for calculating the cyclic modulus from the loading data recorded by the testing machine is given in Appendix B – Code for Modulus Evolution.

$$E = \frac{\Delta\sigma}{\Delta\varepsilon} = \frac{\Delta P \times L_o}{\Delta l \times A} \tag{4.1}$$

The measurement uncertainty in instantaneous elastic modulus can be estimated from the uncertainty in extension, load, and cross-sectional area and by utilizing error propagation equations, Equation (4.2) and Equation (4.3). The uncertainty in the extensometer and the load cell are taken from the calibration records while the uncertainty in the cross-sectional area comes from the uncertainty of the calipers used to measure the specimens' thicknesses and widths. With this information, the elastic modulus uncertainty can be estimated with Equation (4.4). Table 11 provides a summary of the error propagation results while all intermediate steps are shown in Appendix C – Error Propagation. In the end, the initial modulus

values vary between 67.6 and 71.0 GPa with an uncertainty of between 2.6 and 3.7 GPa.

$$For\ c = a + b\ or\ a - b,\ \delta c = \sqrt{(\delta a)^2 + (\delta b)^2} \tag{4.2}$$

$$For\ c = a * b\ or \frac{a}{b},\ \delta c = |c|\sqrt{\left(\frac{\delta a}{|a|}\right)^2 + \left(\frac{\delta b}{|a|}\right)^2} \tag{4.3}$$

$$For\ E = {}^{\Delta P * L_o}/_{\Delta l * A}, \delta E = |E|\sqrt{\left(\frac{\delta \Delta P}{|\Delta P|}\right)^2 + \left(\frac{\delta L_o}{|L_o|}\right)^2 + \left(\frac{\delta \Delta l}{|\Delta l|}\right)^2 + \left(\frac{\delta A}{|A|}\right)^2} \tag{4.4}$$

Table 11: Measurement uncertainty for 11 experiments

Specimen Name	Area, A (mm^2)	Change in Load, ΔP (kN)	Change in extension, Δl (mm)	Original length, L_0 (mm)	Initial Elastic Modulus, E (GPa)
5A16	57.1 ± 0.18	10.8±0.037	0.070 ± 0.0026	25 ± 0.002	67.6 ± 2.6
5A19	57.3 ± 0.18	12.6±0.043	0.079 ± 0.0026	25 ± 0.002	69.6 ± 2.3
5A21	56.9 ± 0.18	9 ± 0.031	0.057 ± 0.0026	25 ± 0.002	69.4 ± 3.2
5A22	56.8 ± 0.18	11.7±0.040	0.073 ± 0.0026	25 ± 0.002	70.6 ± 2.6
5A23	57.1 ± 0.18	8.1 ± 0.028	0.052 ± 0.0026	25 ± 0.002	68.2 ± 3.2
5A24	57.1 ± 0.18	10.8±0.037	0.069 ± 0.0026	25 ± 0.002	68.5 ± 2.6
5A25	57.1 ± 0.18	8.1 ± 0.028	0.050 ± 0.0026	25 ± 0.002	71.0 ± 3.7
5A26	57.2 ± 0.18	9.0 ± 0.031	0.056 ± 0.0026	25 ± 0.002	70.2 ± 3.3

4.3 Discrete Information Entropy Formulations

After AE noise has been filtered and elastic modulus degradation has been estimated, the disorder of AE signals representing fatigue damage can be quantified. Multiple methods of estimating AE signal disorder with information entropy will be presented and discussed. All of the formulations have one commonality; a probability distribution is formed based on voltage readings in individual AE waveforms. Again, this compares to AE features such as counts and energy that are acquisition system outputs that summarize AE waveforms. It is also believed that because information entropy is a measure of a random variable's disorder as described by its probability distribution, the AE information entropy directly reflects microstructural changes due to cyclic loading.

There are two general steps to estimating information entropy from AE signals no matter the formulation. A probability distribution of a random variable describing the AE signals must first be formed followed by quantifying the distribution's disorder via Shannon's entropy equation. Most of the effort is devoted to developing the probability distribution. In this case, the chosen random variable is the signal amplitude expressed in units of voltage. The idea is that the AE voltage probability distribution represents the microstructural disorder, and the distribution is evolving as fatigue damage progresses. The underlying continuously-changing probability distribution is estimated based on received AE signals.

During the beginning of a fatigue experiment, the "true" AE voltage probability distribution is completely unknown until a first AE signal is recorded. Let this AE signal be described by its 2048 voltage readings which are 2048 samples from the current underlying voltage probability distribution. Because we do not know the true AE voltage probability distribution, an imprecise distribution can be estimated from these 2048 voltage values. The disorder of this distribution can then be quantified by Shannon's equation in Equation (2.4).

When a second AE signal is received, the new set of 2048 voltage values provides new information about the voltage probability distribution and needs to be considered. Three different methods to account for this new information about the probability distribution have been investigated and yield three formulations of AE information entropy.

4.3.1 Feature Entropy

First, one can assume that the underlying AE voltage distribution is constantly changing and independent between all time steps. Therefore, a new probability distribution of the second AE signal's 2048 voltage values should be created to estimate the true distribution at that particular instant. With every new AE signal, a new probability distribution is constructed to represent the constantly-changing underlying distribution. The information entropy calculated from each of these distributions is referred to as *feature entropy*.

The framework to calculate feature entropy is depicted in Figure 21. It can be seen that for each signal received, the voltage value is recorded at every microsecond for 2048 microseconds (Step a). The 2048 voltage values are then taken to form a normalized histogram or, in this case, a discrete probability distribution (Step b). Because the 16-bit data acquisition system can output values between -10V and +10V producing a resolution of 0.305 mV, the bin widths are set to 1 mV to encompass 3 or 4 possible voltage values. One could set the bin widths smaller or larger which would alter the entropy value but not the entropy trends. From this distribution, the entropy is calculated based on Equation (2.4) where x_i are the 1 mV bin ranges between -10V and +10V and $p(x_i)$ is the probability of receiving a voltage value within the specific bins. The entropies from these distributions are then plotted against the signal arrival time (Step c).

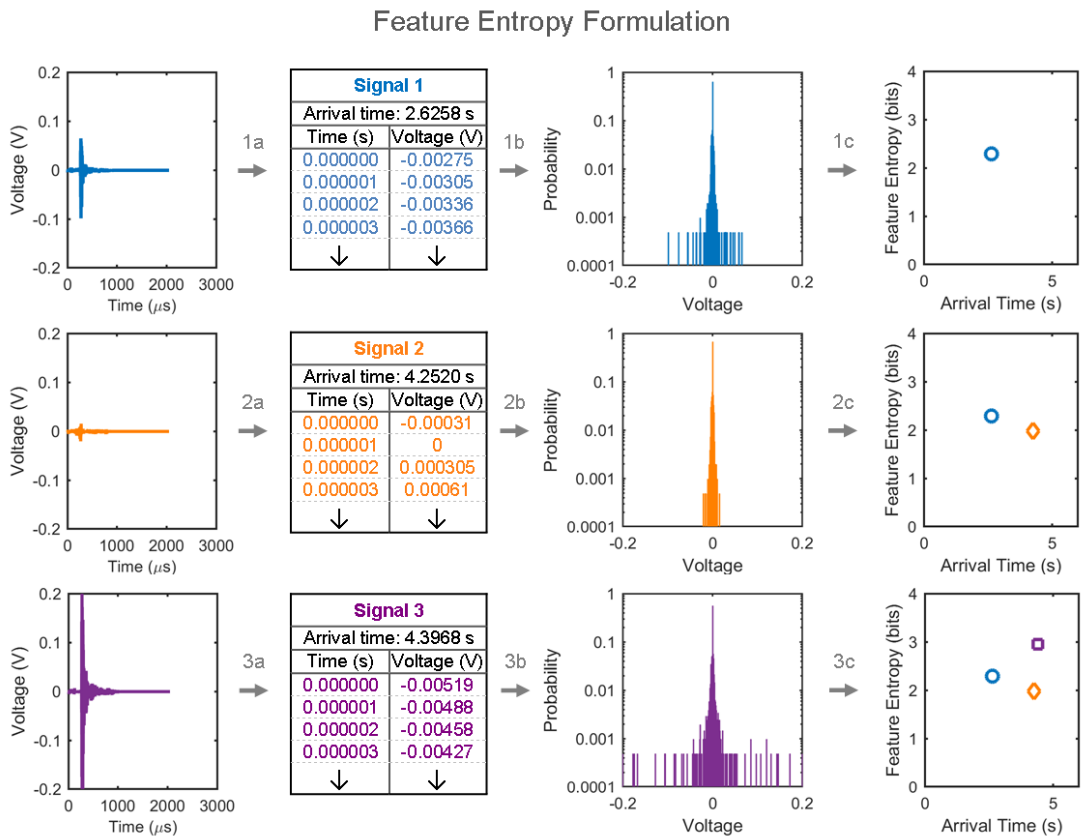

Steps are labeled as a number and then a letter. The number corresponds to the AE signal number while the letter corresponds to the transformation between the previous and next step. Steps a, b, and c are performed for each AE signal received.

- Start = Collect AE signal at a particular arrival time.
- Step a = Each continuous AE signal is saved as a text file containing voltage readings per microsecond for a total waveform length of 2048 microseconds.
- Step b = For each signal, create a normalized histogram for the voltage values with 0.001V bin widths. Highly disordered signals will have a wider distribution than one with low disorder. This is the current estimate of the underlying probability distribution.
- Step c = Calculate the information entropy of the voltage distribution based on Shannon's equation and plot this value against the signal's arrival time.
- Repeat for each signal.

Figure 21: Feature entropy calculation from AE signals

The feature entropy of the three example signals in Figure 21 quantifies the signals' disorders. One can predict that the second signal reflects an event during low microstructural disorder while the first and third signals are during higher disorder microstructural changes. Entropy quantifies this disorder in that the first signal has 2.29 bits, the second has 1.99 bits, and the third has 2.95 bits of entropy. In addition,

the cumulative form of feature entropy can be thought of as the total microstructural disorder as fatigue damage progresses. This form will be discussed in the results.

4.3.2 Updated Entropy

The second formulation is based on the theory that the underlying probability distribution changes very slowly, and the second AE signal received is from approximately the same distribution as the first AE signal. In turn, the 2048 voltage values from the first and second signal are combined, and a distribution is formed from the total 4096 values. As more AE signals are received, the new and previous AE voltage values are concatenated and the estimated probability distribution of the true underlying distribution is essentially updated. Another way to explain this process is that every AE signal's distributions are combined and have equal effect on the estimated distribution. The information entropy calculated from these updated distributions is referred to as *updated entropy*.

Figure 22 shows the process to calculate the updated entropy from AE signals. Similar to the feature entropy procedure, AE signals are received and saved as voltage values per microsecond for 2048 microseconds (Step a). Then, rather than forming a normalized histogram for each individual signal, the current voltage values are first concatenated with all the previous voltage values (Step b). From this series of 2048*i voltage values for i AE signals currently received, a normalized histogram with bin widths of 1 mV are constructed (Step c). Finally, Equation (2.4) is employed to yield entropy and can be plotted against signal arrival time (Step d).

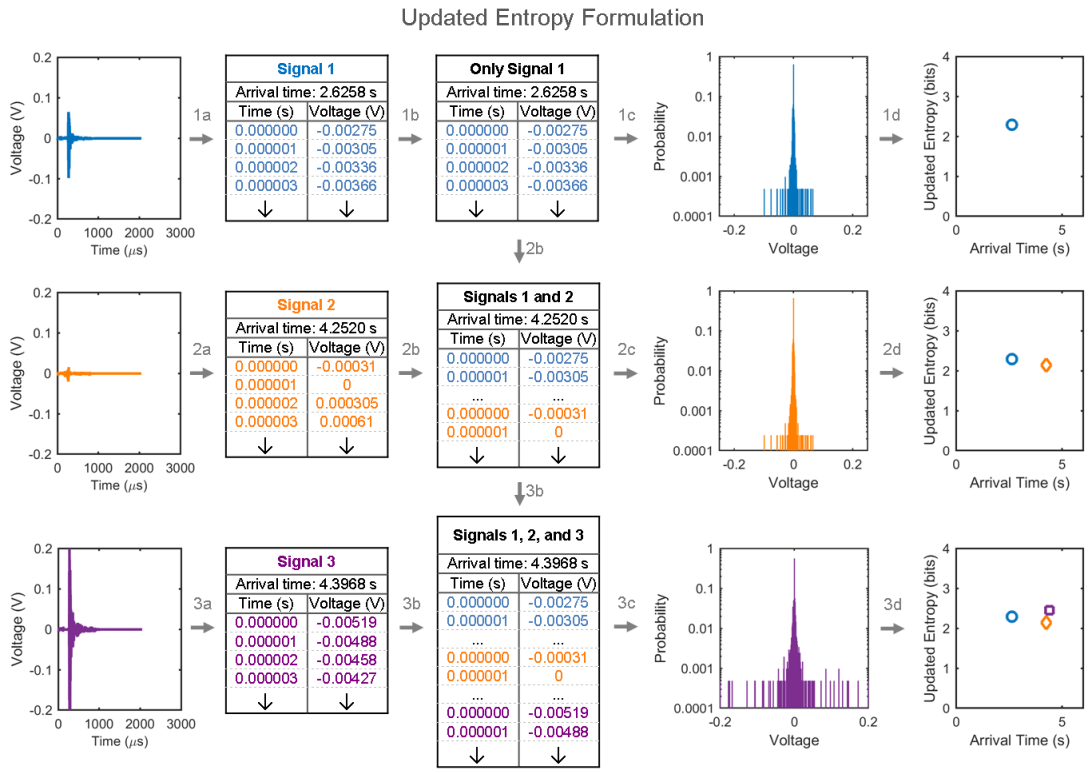

Steps are labeled as a number and then a letter. The number corresponds to the AE signal number while the letter corresponds to the transformation between the previous and next step. Steps a, b, and c are performed for each AE signal received.

- Start = Collect AE signal at a particular arrival time.
- Step a = Each continuous AE signal is saved as a text file containing voltage readings per microsecond for a total waveform length of 2048 microseconds.
- Step b = For each signal, combine both the 2048 voltage readings from the current signal with the voltage readings of all other previous signals.
- Step c = Create a normalized histogram for the entire series of collected voltage values which is the estimate of the true AE voltage probability distribution.
- Step d = Calculate the information entropy of this continually updated distribution based on Equation 2 and plot this value against the signal's arrival time
- Repeat for each signal

Figure 22: Updated entropy calculation from AE signals

The updated entropy of the three example signals in Figure 22 quantifies the disorder of the approximated underlying AE voltage distribution. One can predict that the first and third signals advocate for a wider, more-disordered true voltage distribution while a thinner, less-disordered true distribution is more probable according to the second signal. Subsequently, the updated entropy values for the first, second, and third signals are 2.29, 2.15, and 2.45 bits, respectively. Compared to feature entropy, updated entropy values are dependent on the previous distributions

and are therefore more inertial rather than sporadic. Because of the dependency between current and previous signals, one cannot simply relate the cumulative updated entropy to cumulative fatigue damage and it is best to analyze the scatter plot of updated entropy versus arrival time.

4.3.3 Temporally Weighted Entropy

Finally, the third formulation is based on a slowly-evolving true probability distribution of AE voltage values similar to updated entropy, but assumes recent AE signals are more representative of the underlying distribution than past AE signals. When a second AE signal is received, a distribution of the 2048 voltage values is formed similar to the procedure for feature entropy. Then, the first and second signal's distributions are combined in such a way that the second signal's distribution is weighted more than the first. When subsequent AE signals are received, new distributions are formed where the most recent AE signal has the greatest weight on the updated distribution. The specific weights are determined based on arrival time and are calculated using Equation (4.5) where the weight vector, w, and arrival time vector, AT, are 1 x n vectors and n is the current number of recorded AE signals. For example, if the first AE signal occurs at 2 seconds and the second is recorded at 4 seconds, then the first signal's distribution will have one-half of the weight of the second signal's distribution. The information entropy calculated from these weighted and updated distributions is referred to as *temporally weighted entropy*. It should be noted that references in literature to weighted entropy or temporal entropy are not related to this proposed formulation.

$$\vec{W} = \frac{\overrightarrow{AT}}{\sum_{i=1}^{n} AT_i} \tag{4.5}$$

The procedure to find temporally weighted entropy from AE signals is shown in Figure 23. As with the other methods, the first step is to record AE signals as time and voltage data (Step a). Then, the probability distributions of each of the signals are found by creating normalized histograms with 1 mV bin widths (Step b). Next, the temporal weights are found based on arrival time following Equation (4.5) in which the sum of the weights is 1. The individual signal distributions are then multiplied by their appropriate weights and added together to form an estimate of the true voltage distribution (Step c). The entropy of this temporally weighted distribution is then calculated using Equation (2.4) and plotted against signal arrival times (Step d).

Updated entropy equally weighs all signal distributions and combines them into an estimate of the underlying voltage distribution while temporally weighted entropy weighs current signals more than past signals. Of many possible methods to determined distribution weights, the weighting used in this configuration is simply linearly proportional to signal arrival time. The temporally weighted entropy of the three example signals in Figure 23 quantifies the disorder of the approximated underlying AE voltage distribution as signals are received. Subsequently, the temporally weighted entropy values for the first, second, and third signals are 2.29, 2.11, and 2.48 bits, respectively. Temporally weighted entropy seems to be very similar, yet slightly less inertial than updated entropy. This is expected because previous signals will have less of an effect on the estimated distribution.

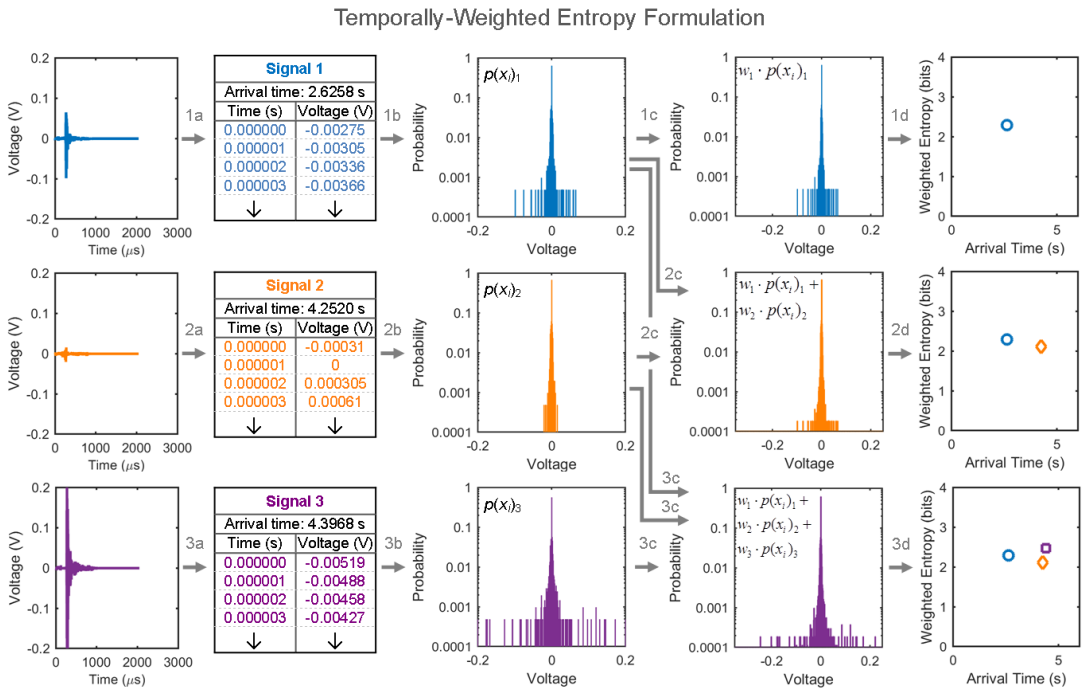

Steps are labeled as a number and then a letter. The number corresponds to the AE signal number while the letter corresponds to the transformation between the previous and next step. Steps a, b, and c are performed for each AE signal received.

- Start = Collect AE signal at a particular arrival time.
- Step a = Each continuous AE signal is saved as a text file containing voltage readings per microsecond for a total waveform length of 2048 microseconds.
- Step b = For each signal, create a normalized histogram for the voltage values with 1mV bin widths. Highly disordered signals will have a wider distribution than one with low disorder. This is the current estimate of the underlying probability distribution.
- Step c = Combine the current AE signal's distribution with all the previous distributions where the signal distributions are weighted proportional to the arrival time. The vector of weights is found from the following equation.

$$\vec{w} = \frac{\overrightarrow{AT}}{\sum_{i=1}^{n} AT_i} \qquad Ex\text{: } [w_1 \quad w_2 \quad w_3] = \frac{[AT_1 \quad AT_2 \quad AT_3]}{AT_1 + AT_2 + AT_3}$$

- Step d = Calculate the information entropy of the voltage distribution based on Shannon's equation and plot this value against the signal's arrival time.
- Repeat for each signal where weight vector is continuously updated.

Figure 23: Temporally weighted entropy calculation from AE signals

4.3.4 Summary of Entropy Formations

Three methods to estimate information entropy from AE signals have been proposed; *feature*, *updated*, and *temporally weighted entropy*. All procedures seek to quantify the microstructural disorder due to fatigue damage as reflected in an evolving AE voltage distribution. While the exact underlying AE voltage distribution is unknown, estimates of this distribution are assumed to be the voltage distributions from collected AE signals. The particular procedure to incorporate newly received AE signals into the voltage distribution estimate is dictated by the specific entropy

formulation. The MATLAB code to derive the entropies from the AE signals is provided in Appendix D – Code for AE Entropy Formulations.

An explicit comparison of the entropy results depending on formulation method is shown in Figure 24 for the three example signals. Feature entropy which produces independent entropy values is the most erratic, updated entropy has the most inertial trend, and temporally weighted entropy is similar to updated entropy with more significance placed on current signal's feature entropy. Table 12 summarizes assumptions and best estimate for the AE voltage distribution for each formulation.

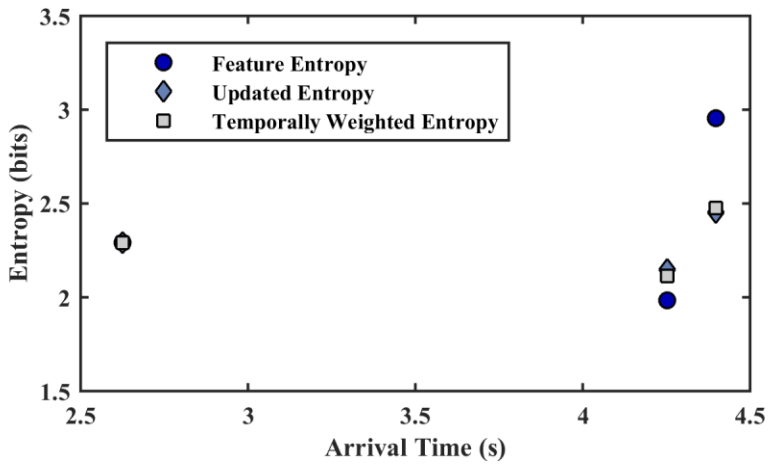

Figure 24: Entropy evolution for three examples of AE signals for each formulation

Table 12: Summary of entropy formulations

Entropy Formulation	Assumption about "true" AE voltage distribution	How best to estimate "true" AE voltage distribution
Feature entropy	Ever-changing and independent between time steps	Independent distributions from each received AE signal
Updated entropy	Slowly changing where changes are assumed to occur with received AE signals	Combine all received AE signal distributions such that all signals have equal weight on estimate
Temporally weighted entropy	Slowly changing where changes are assumed to occur throughout fatigue life	Combine received AE signal distributions such that recent signals have more weight on the estimate than previous signals

Chapter 5 – Results and Discussion

5.1 Crack Growth and Fracture Surface Images

As mentioned in Section 2.1.1 beginning on page 7, fatigue crack growth is known to follow three stages of growth: crack initiation, stable crack growth, and unstable growth to fracture. Depending on the microstructure and loading conditions, cracks may grow through inclusions, grains, or grain boundaries [7]. Small cracks grow at persistent slip bands after crack initiation and form a brittle fracture surface with fatigue striations [8]. Once a crack is of a sufficient length, the crack will propagate rapidly and cause ductile fracture.

These assumptions were investigated with high-magnification images. First, an optical microscope captured images of one of the specimen faces to determine how fatigue cracks grew through the microstructure. Figure 25 is an example of three stitched images that show a crack grew through the grains and often through inclusions. This phenomenon was found for all imaged specimens.

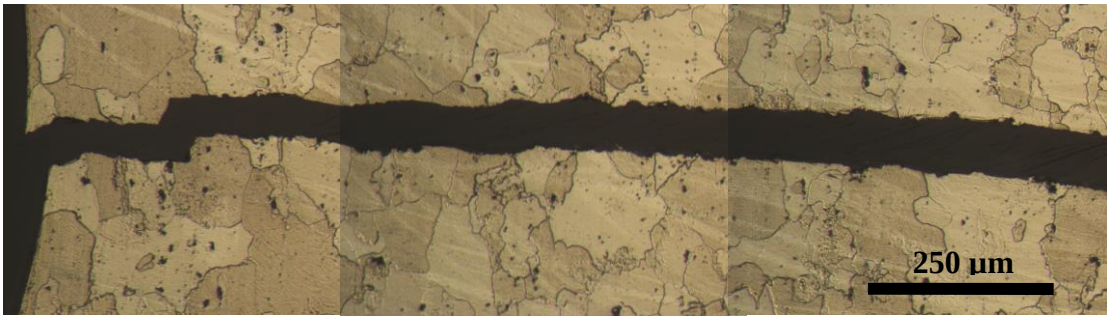

Figure 25: Crack growth through grains and inclusions

Next, fracture surface differences between brittle and ductile crack growth were captured with a scanning electron microscope. Figure 26 depicts the two different regions with 77x magnification. Even higher magnification images in these

two different regions were then taken. Figure 27 in fact shows the fatigue striations in the brittle region at 5740x magnification while Figure 28 shows a more disordered fracture surface during final ductile fracture. Overall, these images proved that cracks generally grew through grains and inclusions and orderly and consistent fatigue striations are present in the brittle fracture region.

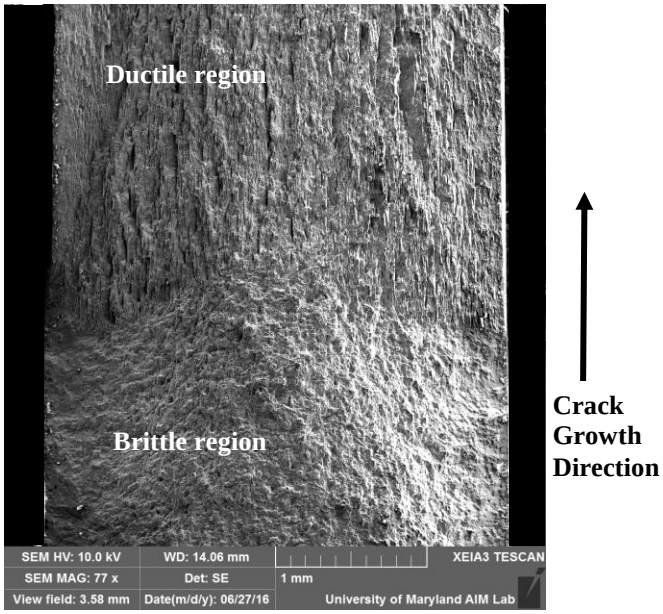

Figure 26: Brittle and ductile regions of fatigue crack growth

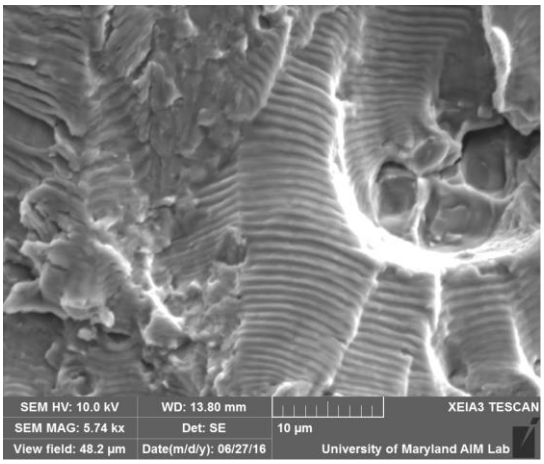

Figure 27: Fatigue striations in the brittle region

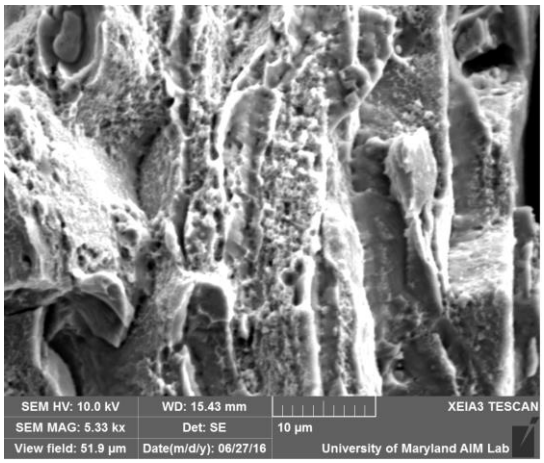

Figure 28: Highly disordered ductile region with no striations

5.2 Stress-Life Analysis

The experiments performed were stress-controlled, constant-amplitude sinusoidal fatigue tests. The specific loading conditions varied between experiments in order to study microstructural damage for low-cycle and mid-cycle fatigue tests. The stress life can be summarized by plotting the nominal stress amplitude against the cycles to failure known as an S-N curve. As mentioned before, 26 tests were performed while issues with the extensometer, crack monitoring system, and AE noise reduced the number of analyzable tests down to eight. However, the cycles to failure were not affected by these errors other than the three tests that failed away from the notch at low loads. Therefore, all tests excluding the three that failed away from the notch can be used to form the experimental S-N curve.

It is assumed that the S-N curve follows a power relationship between the cycles to failure and the stress amplitude given by Equation (5.1) where σ_f' is the stress amplitude for failure near 0 cycles, N_f are the cycles to failure, and m is the exponential parameter. Here, m is related to stress intensity factor (K_t), notch sensitivity (q), surface roughness (k_{SF}), loading factor (k_L), and effective diameter (k_{size}) of a notched specimen and is approximated by Equation (5.2) – Equation (5.6) [77].

$$Stress\ Amplitude = \frac{\Delta\sigma}{2} = \sigma_f'(N_f)^m \tag{5.1}$$

$$\sigma_f' = 1.62 * \sigma_u \tag{5.2}$$

$$m_{notch} = m_{no\ notch} - \frac{\log\left(\frac{K_f}{k_{SF}k_L k_{size}}\right)}{\log(N_{FL})} \tag{5.3}$$

$$K_f = 1 + (K_t - 1)q \tag{5.4}$$

$$q = \frac{1}{1+\frac{0.5\ mm}{\rho}} \tag{5.5}$$

$$k_{size} = \left(\frac{d}{7.62\ mm}\right)^{-0.1133} \tag{5.6}$$

The theoretical S-N curve can be determined for the particular specimen geometry and material used in this study. All parameters used to find the theoretical S-N curve are listed in Table 13 after implementing Equation (5.2) – Equation (5.6). Here, the theoretical curve has an intercept of 950.5 MPa and an exponential parameter of -0.242.

Table 13: Parameters for theoretical S-N curve for particular Al7075-T6 specimen

Parameter Name	Parameter symbol	Value
Intercept	$\sigma_f{}'$	950.5 MPa
Exponential parameter with notch	m_{notch}	-0.242
Exponential parameter without notch	$m_{no\ notch}$	-0.176
Ultimate tensile strength	σ_u	587 MPa
Stress concentration factor	K_t	2.61
Notch radius	ρ	1 mm
Notch sensitivity factor	q	0.667
Notch factor	K_f	2.073
Effective diameter	d	18 mm
Size factor	k_{size}	0.907
Surface roughness factor for polished surface	k_{SF}	1.000
Axial loading factor	k_L	0.923
Assumed fatigue limit cycles	N_{FL}	10^6

The experimental S-N curve was determined by plotting the nominal stress amplitude against cycles to failure for the 23 experiments that had a crack grow at the notch. Then, a power relationship was fit to the data to yield an experimental S-N relationship. Figure 29 displays the experimental S-N plot along with theoretical and experimental curves. In the end, the experimental data agreed well with the theoretical curve and only slight differences are evident between the theoretical and experimental equations.

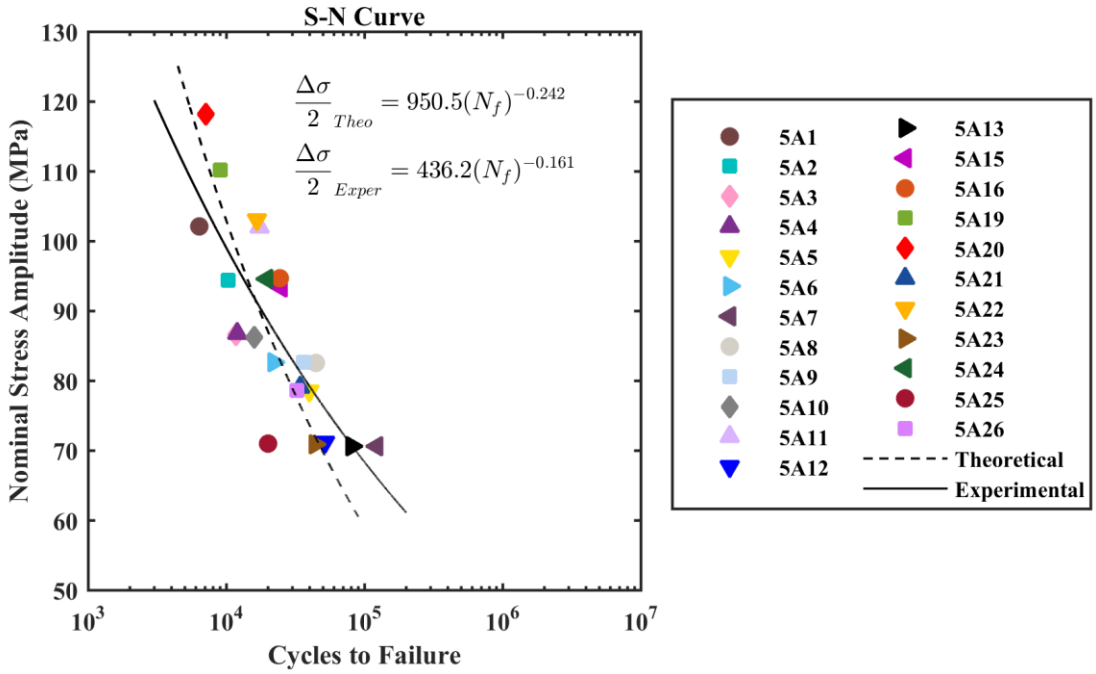

Figure 29: Experimental S-N plot with theoretical and experimental S-N curves

5.3 Measured Damage from Modulus Degradation

5.3.1 Modulus Trends

The statistic assumed to quantify true fatigue damage and therefore the parameter that AE features and entropy will be correlated to is elastic modulus degradation. Unlike visible crack growth where AE counts and features have often been correlated to crack length or crack growth rate, elastic modulus is expected to reflect the fatigue damage prior to crack initiation. First, the relationship between elastic modulus and fatigue cycles should be understood. Figure 30 shows the trends for the 8 experiments that had consistent experimental setups with the exception of the loading conditions. The figure is divided into four different plots showing the

modulus degradation at crack initiation, when a crack grows to 0.25 mm, then to 1 mm and then when the specimen fractures.

From this chart, three conclusions can be made. First, modulus does not decrease for the majority of life. In order to utilize elastic modulus as a measure of fatigue damage prior to a visible crack, the elastic modulus should change prior to crack initiation. However, this phenomenon is not apparent. In the first plot of Figure 30, it is proven that four experiments show a decrease in modulus at crack initiation while the other four do not. When a crack reaches 0.25 mm, the US Navy's retirement crack length [1], still there are two experiments that do not show a decrease in modulus. It is not until a 1 mm crack, defined as the transition between small and large cracks as noted in Table 1, that all tests prove to have a decrease in modulus.

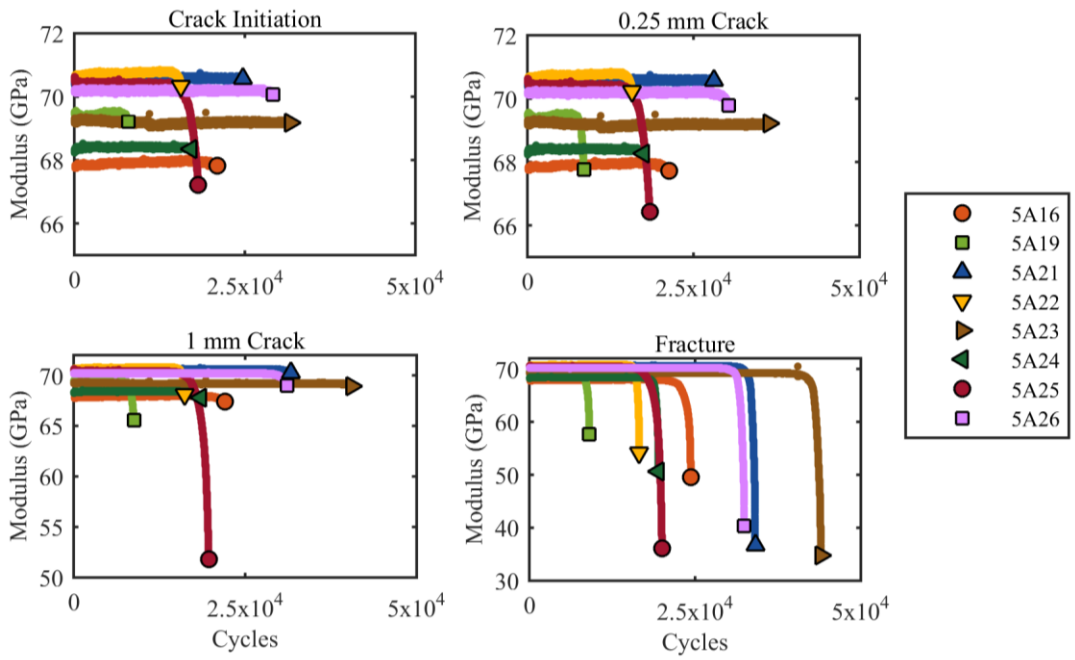

Figure 30: Raw modulus degradation for 8 experiments at various damage levels

A more sensitive measure of modulus may be achieved if the strain was measured within a smaller gauge length near the notch rather than the 25 mm extensometer gauge length. Despite this drawback, the measured damage from modulus degradation will be used to correlate AE features after a 1 mm crack.

The second finding, as expected, is modulus decreases near the cycles to failure as seen in the last plot of Figure 30. Of course, the particular number of cycles where modulus decreases is dependent on the applied load. For example, a 110 MPa stress amplitude was applied to 5A19 which experienced rapid damage near 10,000 cycles while 5A23 had a lower amplitude of 71 MPa with rapid damage occurring at a higher 44,000 cycles.

Finally, one can compare the final value of modulus. Theoretically, modulus should decrease towards zero as a specimen fractures. However, the modulus depends on the final extensometer extension immediately prior to when the specimen breaks. With the exception of 5A25, it seems the final modulus value is related to the cycles to failure where tests that last longer will have a lower final modulus value. This result is attributed to the idea that a crack grows more slowly for lower stress amplitudes with more cycles to failure. In this case, more elongation and therefore lower modulus is apparent prior to sudden ductile fracture.

Throughout the plots in Figure 30, 5A25 proved to have a greater change in modulus at all stages of fatigue prior to fracture than the other experiments. The reason to why the 5A25 modulus behaved in this manner can be explained by observing the fracture surface pictured in Figure 31. Typically, a fracture surface will be relatively flat and smooth at the site of crack initiation. However, two fracture

surface regions at the notch can be clearly seen. This suggests that a crack initiated at a notch corner but propagated along the specimen width rather than the thickness. In turn, this uneven crack propagation surface may have caused the specimen to elongate more prior to fracture.

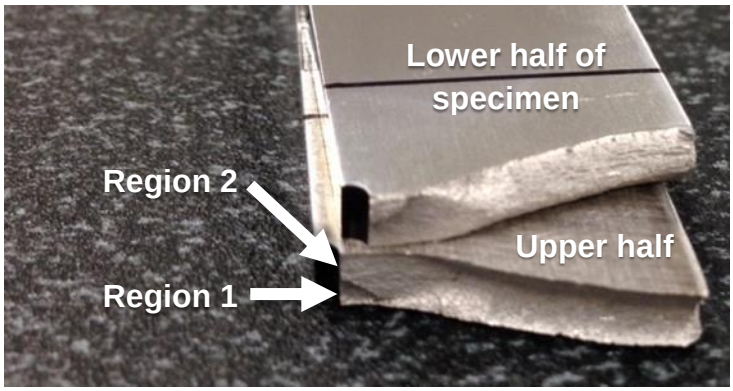

Figure 31: 5A25 fracture surface showing two displaced regions at notch

5.3.2 Normalizing Modulus to Produce Measured Damage

The raw modulus trends can be transformed into a normalized metric of damage referred to as *measured damage*. The correlation between AE parameters and this statistic allows data from all tests to be combined and analyzed together. In this case, damage is calculated based on Equation (5.7) where $E_{instant}$ is the modulus at each cycle, E_0 is the initial modulus, and E_f is the final modulus. This equation ensures the variations between the initial and final modulus of the experiments are reduced to near zero. A measured damage value of 0 refers to a pristine specimen while 1 is associated with specimen fracture.

$$Measured\ Damage = \frac{E_{instant} - E_0}{E_f - E_0} \tag{5.7}$$

Rather than plotting the raw measured damage data that has some scatter, curves can be fit to the data and approximate the trend between damage and cycles.

Because the measured damage stays approximately constant and then sharply increases near failure, the exponential model fits the data well. The general formula for the exponential model is given as Equation (5.8), where D is measured damage, N is cycles, and a and b are fitted parameters in this case. Fitted curves of each data series were found using MATLAB's built-in curve fitting toolbox. Fitted model statistics are noted in Table 14.

$$D = a * e^{b*N} \tag{5.8}$$

Table 14: Fitted models for measured damage

Test Name	a	b	SSE	R-square
5A16	3.01E-18	0.00166	3.240	0.981
5A19	1.82E-13	0.00324	0.965	0.989
5A21	4.32E-40	0.00266	0.796	0.994
5A22	1.79E-30	0.00413	0.615	0.994
5A23	9.28E-36	0.00184	0.600	0.997
5A24	1.46E-30	0.00353	0.482	0.995
5A25	1.93E-12	0.00135	2.057	0.992
5A26	2.68E-34	0.00239	0.233	0.999

The damage trends against cycles can be plotted for all experiments from these exponential models. Rather than observing the raw modulus degradation as in Figure 30, Figure 32 shows the damage trends up until crack initiation, a 0.25 mm crack, a 1 mm crack, and then final fracture. Since the fatigue damage trends are scaled so that the initial and final damage values are the same for all tests, one can more clearly observe that it is not until a 1 mm crack when all experiments prove to have a measurable increase in damage.

Another point of discussion is the value of damage at specific crack lengths. The measured damage should intuitively be the same for all tests at a consistent

damage level and crack length regardless of the paths (i.e., applied loading) to that damage. However, Figure 32 proves that the damage values vary between experiments at crack initiation, a 0.25 mm crack, and at a 1 mm crack. This unexpected outcome can potentially be attributed to measurement errors.

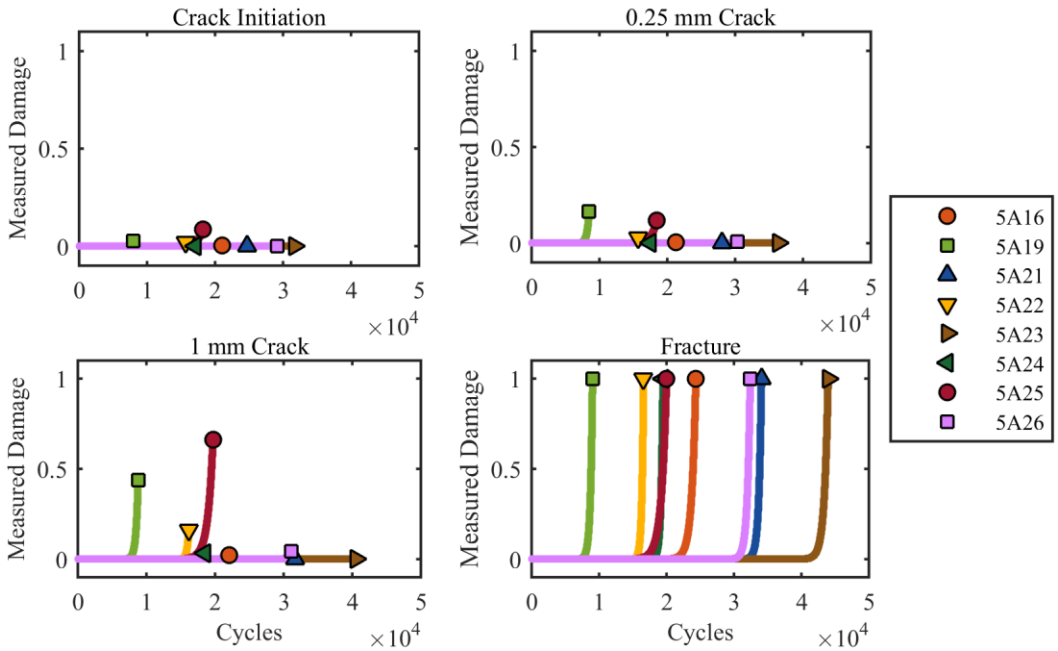

Figure 32: Measured damage for 8 experiments at various damage levels

There are two main variables that are uncertain; the cycles at which cracks reach 0.25 mm and 1 mm and the measured damage values at these cycles. First, accurately estimating the cycles is dependent on properly estimating the crack length. The exact points when a crack is at precisely 0.25 mm and 1 mm are most likely missed since crack monitoring images are taken every 25 cycles. Therefore, the nominal crack length measurement is assumed to be imprecise. Also, measuring the length of a crack from crack monitoring images has an uncertainty due to pinpointing the proper beginning and end of a crack as well as estimating the picture scale as introduced in Section 3.4. Table 15 shows a summary of the error propagation in

measuring the length of a 0.25 mm and 1 mm crack while more detailed steps are in Appendix C – Error Propagation. In the end, the average measurement for a 0.25 mm crack is about 0.258 mm ± 0.021 mm while the average measurement for a 1 mm crack is about 1.062 mm ± 0.083 mm from these inaccuracies.

Table 15: Error for crack length measurements

Specimen Name	Picture Scale (pixels/mm)	0.25 mm Crack (mm)	% Error at 0.25 mm	1 mm Crack (mm)	% Error at 1 mm
5A16*	24.7 ± 2.0	0.268 ± 0.084	31.3	1.078 ± 0.120	11.1
5A19	672.8 ± 46.3	0.272 ± 0.020	7.2	1.036 ± 0.072	6.9
5A21	725.8 ± 57.6	0.239 ± 0.020	8.3	1.011 ± 0.080	8.0
5A22	714.3 ± 51.3	0.249 ± 0.019	7.5	1.100 ± 0.079	7.2
5A23	651.0 ± 43.4	0.258 ± 0.018	7.1	1.041 ± 0.070	6.7
5A24	682.3 ± 76.5	0.262 ± 0.030	11.4	1.065 ± 0.120	11.2
5A25	600.8 ± 43.5	0.256 ± 0.020	7.7	1.094 ± 0.080	7.3
5A26	713.2 ± 52.2	0.260 ± 0.020	7.6	1.074 ± 0.079	7.3

* The DIC was used to monitor the crack growth in 5A16 and resulted in higher uncertainty measurements

With uncertainties in crack length, the cycles at which cracks reach such lengths are also uncertain and can be estimated from the approximate crack growth rate. For simplicity, the crack growth rate at a 0.25 mm crack is found by dividing the measured length by the difference in cycles between the 0.25 mm crack and initiation. Similarly, the growth rate at a 1 mm crack is found by dividing the difference between the measured 1 mm and 0.25 mm length by the difference in cycles between the 1 mm and 0.25 mm crack. Then, the uncertainty in cycles at the 0.25 mm and 1 mm crack are calculated by dividing the uncertainty in the measurement by the crack growth rate as shown in Equation (5.9). Table 16 displays the results of this process where the error in cycles at 0.25 mm is on average 110 cycles and the cycle uncertainty at 1 mm is about 170 cycles. Because the error in the cycles is relatively small compared to the failure cycles between 0.9×10^4 and 4.5×10^4, the uncertainty in

crack length measurement in fact does not cause a significant change in measured damage.

$$\delta cycles = \frac{\delta\ crack\ length\ in\ mm}{crack\ growth\ rate\ in\ mm/cycles} \tag{5.9}$$

Table 16: Error in cycles at measured crack lengths

Specimen Name	Cycles at Initiation	Cycles at 0.25 mm	Cycles at 1 mm	da/dN at 0.25 mm (mm/cyc)	da/dN at 1 mm (mm/cyc)	Error in Cycles at 0.25 mm	Error in Cycles at 1 mm
5A16	21000	21150	22050	0.00179	0.00090	47.0	162.1
5A19	7910	8485	8785	0.00047	0.00255	41.5	29.1
5A21	24750	28060	31715	0.000072	0.00021	273.6	392.2
5A22	15650	15725	16155	0.00332	0.00198	5.6	41.1
5A23	31645	36380	40495	0.000054	0.00019	335.1	378.3
5A24	17100	17525	18505	0.00062	0.00082	48.6	150.4
5A25	18190	18410	19695	0.00116	0.00065	16.9	125.6
5A26	29110	30335	31110	0.00021	0.00105	93.5	77.4

Another instance where significant measurement error is introduced is monitoring the crack length from only one side of the specimens. In a pure axial loading condition, a crack would grow evenly such that the crack length is the same on both specimen faces. However, cracks often grow unevenly due to a slight bending moment when the specimen is not perfectly aligned and can initiate on the side of the specimen opposite from the optical microscope. In this case, the modulus may significantly decline due to a propagating crack while a smaller crack length is measured. This situation is believed to be the main reason why the damage value is not comparable between tests at similar crack length measurements based on the previous discussion on 5A25 fracture surfaces. Experiments with measured damage near zero at certain crack lengths (5A16, 5A21, 5A23, 5A24, and 5A26) suggest the crack grew evenly or on the microscope specimen side while those with higher measured damage at these crack lengths (5A19, 5A22, and 5A25) suggest the crack grew unevenly or on the opposite side. In the end, the measured damage level that is

most certain is at fracture. Thus, the measured damage was normalized so that all experiments had a consistent value here while the other damage values vary between experiments and are assumed to be uncertain.

In summary, modulus was estimated for each cycle based on maximum and minimum values of stress and strain for all tests. The measured damage was then derived from normalizing the modulus data and fitted with exponential relationships using MATLAB's curve fitting toolbox. Measurement error was investigated to reconcile differences between experiments in measured damage at specific crack lengths. In the end, it is believed that there is high uncertainty in measured damage due to monitoring the crack growth on only one side of the specimen. As such, AE parameters including AE counts, energy, and entropy statistics will be compared to this normalized metric at specimen fracture where there is less uncertainty. Comparisons will be drawn between the AE parameters' correlations to measured damage.

5.4 AE Parameter Cyclic Trends

A first step to understanding AE parameter behaviors is to observe the trends with respect to fatigue cycles. In this section, the time-dependent trends for AE cumulative counts, AE cumulative energy, cumulative feature entropy, updated entropy, and temporally weighted entropy will be presented and discussed.

5.4.1 AE Counts

AE cumulative counts is an AE feature commonly correlated to fatigue damage. To reiterate, counts are the number of times an AE signal crosses the prescribed amplitude threshold. In this case, all tests had the same threshold of 45 dB

and specimens were fatigued until fracture producing comparable count results. Because of the uncertainty of measured damage during fatigue life, it is best to see the cumulative counts behavior until specimen fracture as reported in Figure 33. This graph shows that cumulative counts slightly increases initially, stays constant for the majority of life, and then begins to increases near 80% to 90% of fatigue life until final fracture. This trend proves to be similar to fatigue stages in which crack growth is relatively constant for almost the entirety of fatigue and then sharply increases once a crack has initiated.

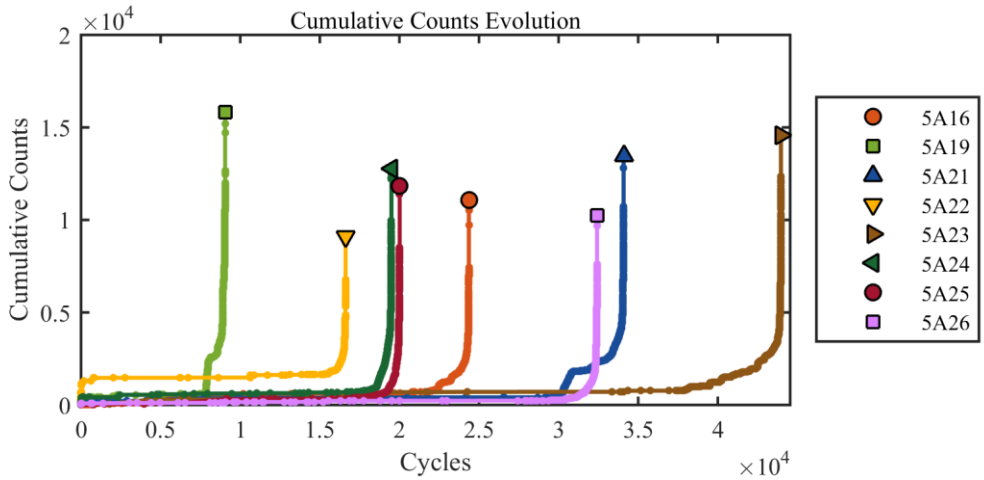

Figure 33: Cumulative AE counts versus fatigue cycles until fracture

Another point to consider from cumulative counts is the total cumulative counts at fracture. Theoretically, measures of damage should be approximately the same between identical structures that have been exhibited to the same level of fatigue loading. In other words, any metric that represents the cumulative fatigue damage within a structure should be similar for all specimens with cracks of equal lengths and at fracture. This idea as first discussed in terms of final modulus degradation at fracture can also be applied to cumulative AE counts, cumulative energy, and cumulative feature entropy.

It appears that the final cumulative AE counts for the experiments are similar with values ranging between 9,000 and 16,000 counts. The spread of this value can be quantified by the coefficient of variation (CV). The CV measures the relative standard deviation of a set of random numbers assumed to have come from a normal distribution. Equation (5.10) shows how to calculate the CV in percent, where σ is the sample standard deviation and μ is the sample mean. A CV of 0 suggests all values are the same with no variability (i.e., no uncertainties) while wider data scatters will have larger CV values. In this case, the mean and standard deviation of the final cumulative counts are 12,360 and 2,245 producing a CV of 18.2%.

$$\%CV = \frac{\sigma}{\mu} * 100\% \tag{5.10}$$

There are several potential causes of this variation in the final cumulative counts as well as other AE parameters at fracture. First, as discussed throughout this work, AE is susceptible to background noise. Despite applying a novel mechanical damping apparatus to the specimens to damp background noise, noise signals were filtered based on applied load during post-processing. However, this procedure was somewhat subjective given that only clusters of AE signals on the applied load versus fatigue cycle graphs were removed rather than a more consistent set of criteria (e.g., load threshold, frequency band). Therefore, damage-related signals within these clusters could have been unintentionally discarded or stand-alone noise signals were accepted without indication they were due to noise. Thus, the AE features could vary due to inaccuracies in classifying damage and noise signals.

Another reason why cumulative AE features could differ between specimens at failure is due to the sensor placement and attachment method. AE signals are

generated due to a sudden release of elastic strain energy which produces a propagating acoustic wave. Prior to reaching the AE sensor, the wave attenuates within the structure. If an AE sensor was placed closer to the fatigue notch, higher amplitude signals with generally more counts may be recorded since there would be less distance for the signal to travel and attenuate. In addition, the sensor is coupled to the specimen surface with an ultrasonic gel. If there were to have been any changes in the gel application method between experiments, the AE signal features may differ between specimens.

Finally, inherent microstructural differences may cause differences in AE signals and their features. AE signals are emitted as a crack grows through grains and inclusions. As dislocations pile up at grain boundaries and a crack suddenly overcomes obstacles, more elastic energy is expected to be released causing a high count, high energy AE signal. Specimens with more crystallographic variation where slip system orientations often change may have more significant AE signals. Likewise, structures with smaller and therefore higher grain density could be expected to have more significant AE signals.

Overall, cumulative counts as well as cumulative energy and cumulative feature entropy are expected to have similar final values at fracture with variation due to inaccurate AE noise reduction, variable sensor configuration, and microstructural differences.

5.4.2 AE Absolute Energy

Another commonly used AE feature to detect fatigue damage is absolute energy. Absolute energy is derived from the squared voltage signal and the signal's

duration. In addition, the cumulative form of absolute energy can be thought of as the total measureable acoustic energy expelled during cyclic fatigue. Figure 34 shows the cumulative absolute energy plotted against cycles until specimen fracture. Cumulative absolute energy, when plotted on a log scale, follows a similar trend to AE cumulative counts in that the energy initially increases, remains approximately constant, and then begins to increase once a crack initiates.

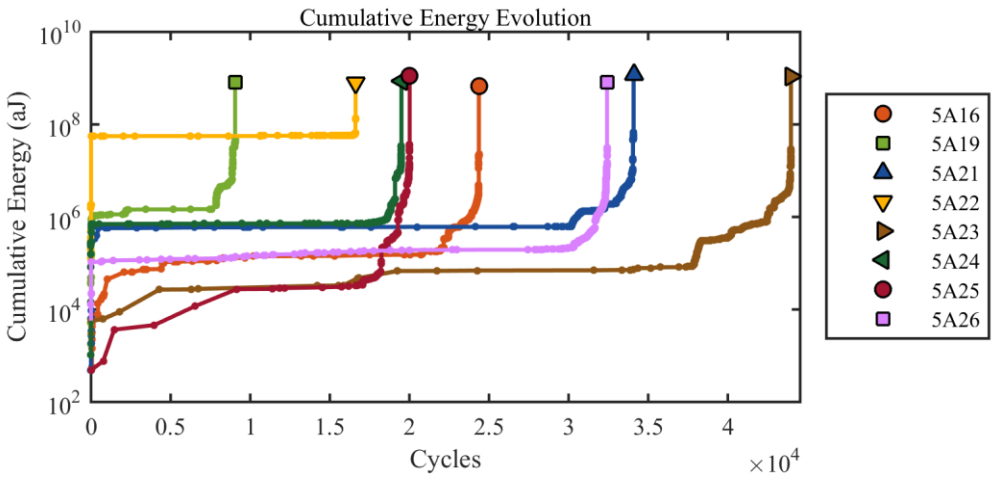

Figure 34: Cumulative AE energy versus fatigue cycles until fracture

Similar to cumulative counts, the final cumulative energy can be assessed. The mean of the final cumulative energy is 9.21×10^{8} aJ and the standard deviation is 1.87×10^{8} aJ resulting in a CV of 20.2% using Equation (5.10). This value suggests cumulative energy at the point of fracture is slightly more variable compared to the CV of cumulative counts at 18.2% meaning energy may be more susceptible to experimental inconsistencies that affect AE signals.

5.4.3 Feature Entropy

Feature entropy proposed in this thesis is calculated from AE signals by forming independent and new distributions of each individual AE signal's voltage

values and employing Shannon's equation to estimate the distributions' disorders. This entropy method is believed to reflect the disorder in each AE signal as well as the microstructural disorder due to fatigue damage. As such, the total disorder from AE signals is assumed to be measured by cumulative feature entropy. Cumulative feature entropy is plotted against cycles until fracture in Figure 35. Yet again, this statistic seems to be congruent with AE cumulative counts, AE cumulative energy, and fatigue damage stages where the disorder is found to increase initially, remain constant, and then increase sharply prior to a 1 mm crack and final fracture.

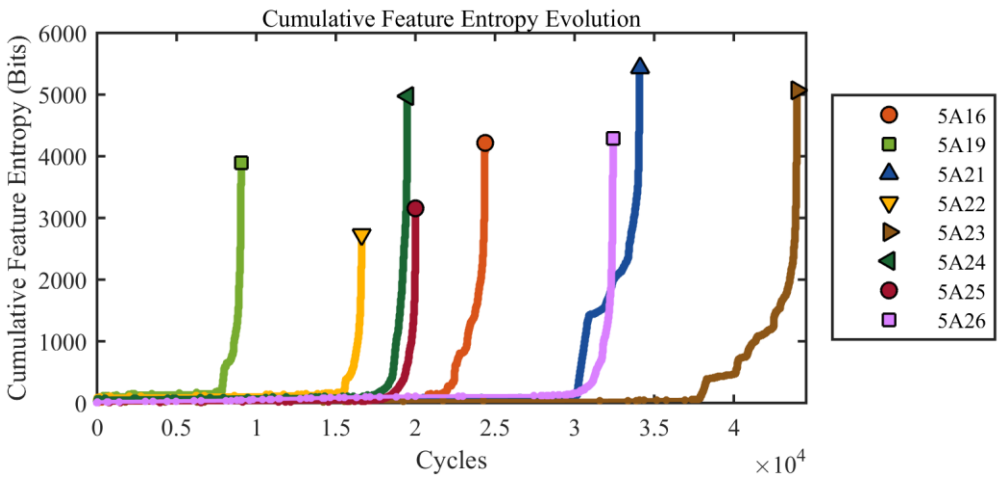

Figure 35: Cumulative feature entropy versus fatigue cycles until fracture

As with the two previous AE cumulative features, the final feature entropy at specimen fracture can be discussed. It is expected that the cumulative microstructural disorder at fracture is similar between specimens with some variation. The mean of the final cumulative feature entropy is 4221.6 bits and the standard deviation is 945.2 resulting in a CV of 22.4% from Equation (5.10). As such, this value suggests that cumulative feature entropy has the most variability at fracture as compared to cumulative counts and cumulative energy. Therefore, one could say feature entropy may be most susceptible to experimental differences compared to the other two

traditional AE features. While it may seem advantageous for a parameter to have a lower CV, the higher variation for feature entropy means that is it more sensitive to slight differences in AE signals. In other words, it could potentially be a better, more sensitive measure of damage if variations between experiments were reduced.

5.4.4 Updated Entropy

Rather than estimating the individual and independent disorders from each AE signal, the updated entropy was introduced in this thesis as the disorder that describes the current and underlying AE voltage probability distributions. An estimate of the true AE voltage distribution is continuously updated as new AE signals are received by weighing all AE signal distributions evenly. The disorders of the estimated distributions are then calculated based on Shannon's equation to yield *updated entropy*. Since updated entropy is found from a continuously updated distribution that utilizes all currently received AE signals, it is not necessarily logical to view updated entropy in a cumulative form. Instead, updated entropy should be plotted in its singular form. In turn, the final value of updated entropy is not expected to be consistent between experiments.

Updated entropy is meant to estimate the current distribution of possible AE voltage values. If significant and unique microstructural damage occurs within the structure, then it is expected that AE signals with large voltage amplitudes will be received and therefore the probability distribution will grow wider. In contrast, when small microstructural damages occur and emit small amplitude AE signals, the estimated voltage distribution will become thinner and concentrate at 0 volts.

The trend of updated entropy can be predicted based on this logic. First, signals received during crack initiation are assumed to be infrequent due to dislocation pile up [47] and have high disorder from the sudden release of energy when dislocations break away [41]. In addition, AE signals are received from numerous locations around the notch since a crack has not yet initiated and the exact location of crack initiation is uncertain. Therefore, it is hypothesized that the updated entropy prior to crack initiation will be relatively high-valued and sporadic due to the high energy and inconsistent AE sources. After a crack begins to initiate, previous work [47] suggests sudden bursts of low amplitude AE signals due to micro-cleavage will then be received. It is believed that these AE signals are of low amplitude because most AE signals now are emitted from the particular microcrack causing initiation rather than from multiple potential crack initiation sources leading to frequent, low-disordered AE waveforms. Thus, the entropy trend will decrease as a crack initiates and grows in an orderly manner. Finally, high amplitude AE signals are expected to be received once the crack propagates to a critical length and causes fracture. In turn, updated entropy will then increase near fracture.

To test this hypothesis, the updated entropy is plotted against cycles until both a 1 mm crack and until fracture in Figure 36. Results validate the hypothesized entropy trend. The updated entropy varies for the first few signals since the voltage distribution is not yet inertial and heavily dependent on these first initial signal distributions. Then, sporadic AE signals are received for the majority of life as dislocation pileups and breakaways occur at multiple potential crack initiation sources. After a crack initiates and continues to grow to 1 mm, the first plot of Figure

36 shows that the updated entropy sharply decreases. This finding confirms that entropy decreases after a crack has initiated and AE signals are more frequent and less disordered. The trend then increases as the crack grows towards fracture as seen in the second plot of Figure 36, again agreeing with the hypothesis. Thus, this entropy trend may be able to dictate when a crack initiates and grows to a small length characterized by a sharp decrease and when a specimen is near fracture described by a sharp increase.

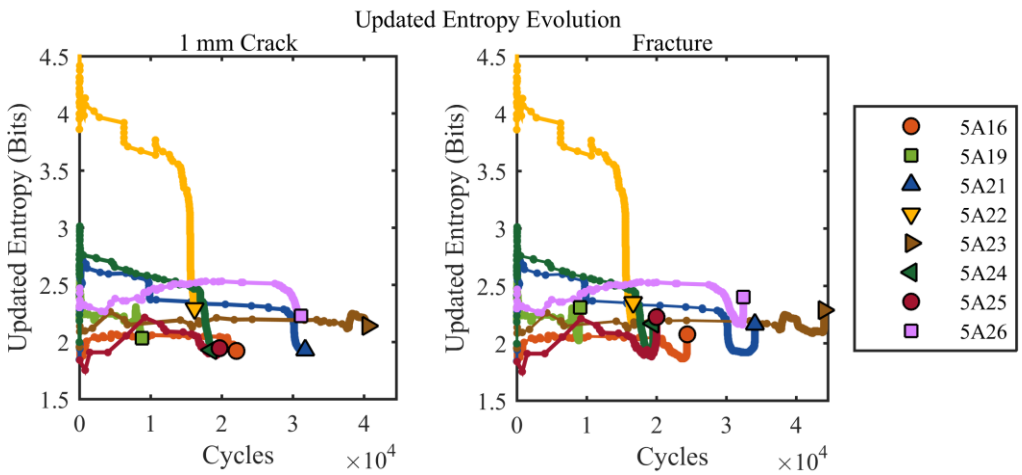

Figure 36: Updated entropy versus fatigue cycles until a 1 mm crack and fracture

5.4.5 Temporally Weighted Entropy

Finally, the last entropy statistic introduced in this thesis as a possible measure of microstructural disorder for AE signals is the *temporally weighted entropy*. This entropy is calculated based on the same idea as updated entropy where the underlying AE voltage distribution is estimated from all measured AE signals. Rather than weighing the individual signal distributions evenly, the signal distributions from recent signals are weighed more heavily than past signals. The weights are linearly proportional to the signal arrival times. Then, once the estimated underlying

distribution is updated as new signals are collected, Shannon's equation is employed to quantify the disorder.

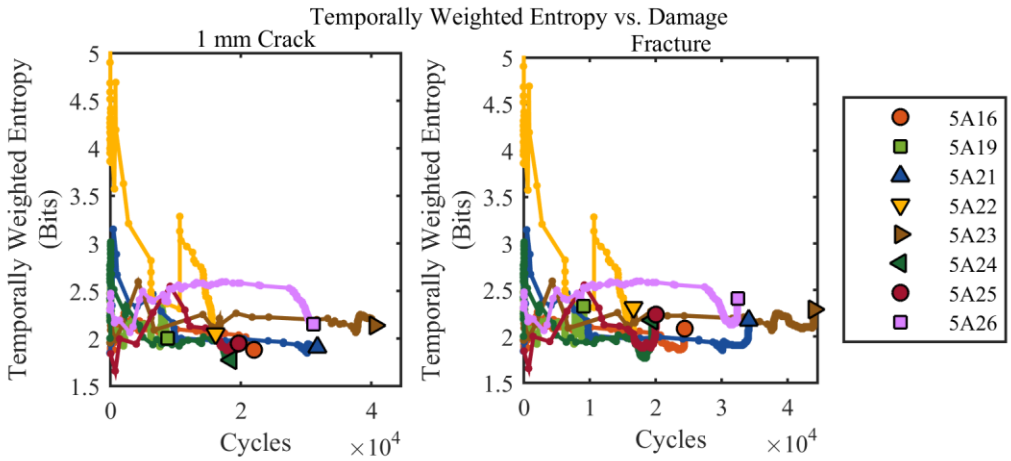

Figure 37: Temporally weighted entropy versus fatigue cycles until a 1 mm crack and fracture

Temporally weighted entropy is expected to follow the same trend as updated entropy yet be more influence by individual AE signal disorder. This thought is validated when plotting the temporally weighted entropy versus cycles for a 1 mm crack and fracture in Figure 37. The weighted entropy has the same general trend as updated entropy in all graphs but is more erratic during initial fatigue cycles. This is because few AE signals are collected prior to crack initiation and a 1 mm crack. When a signal is received 200 cycles after the most recent signal, for example, the disorder of the current signal will have a greater influence on the estimated distribution that the signal 200 cycles before. When two signals received are separated by only a few cycles, their contributions to the estimated distribution will be approximately the same and weighted entropy will change very slightly. In the end, there are slight differences between updated entropy and temporally weighted entropy, but both show a noticeable decrease prior to a 1 mm crack followed by an increase as the specimen fractures.

5.5 Normalized AE Parameters Compared to Measured Damage

The overall goal of this work is to investigate the ability of AE parameters to predict or correlate to fatigue damage. Now that each of the AE parameter trends with respect to cycles has been discussed, comparisons between the parameters with respect to damage can be drawn. The parameters will be normalized so that the variability between experiments is reduced and metrics are no longer scale-dependent. Parameters are normalized by Equation (5.11) where p is any AE parameter. As such, comparisons between the cumulative parameters (counts, energy, and feature entropy) with respect to measured damage will be first discussed followed by a comparison between updated and temporally entropy against damage. MATLAB code used to match the measured damage to the AE parameters at AE hits and to normalize AE parameters is given in Appendix E – Code for Matching Modulus and AE Hits Data.

$$p_{normalized} = \frac{p_i - p_{min}}{p_{max} - p_{min}} \tag{5.11}$$

5.5.1 Cumulative Counts, Energy, and Feature Entropy

Counts, energy, and feature entropy are assumed to reflect damage in a similar way. Progressing fatigue damage causes elastic strain energy to be suddenly released resulting in measured AE signals. When more significant microstructural changes occur, AE signals with higher counts, energy, and disorder are recorded. In turn, the cumulative forms of these parameters are expected to be metrics of cumulative fatigue damage.

While these three parameters are similar, one may ask what the differences between them are and which one represents the damage “better”. These questions can

be answered by considering the normalized parameters against the normalized metric of modulus degradation, measured damage. Based on the cyclic trends, it is expected that each parameter increases more at the beginning and end of damage and increases less for the majority of damage. However, normalized cumulative AE parameters with a constant relationship with measured damage would be ideal and suggest "perfect correlation". For every increase in damage, it is assumed in this case that there is an equal increase in cumulative AE damage parameters. In other words, it is assumed that cumulative AE features are best to predict damage if they have a one-to-one relationship on normalized scales in this specific context.

Figure 38 presents these graphs for the 8 experiments until specimen fracture along with the desired one-to-one relationship. All features show a greater increase at the beginning and end of damage compared to the middle damage values and deviate from the ideal relationship. More specifically, about 60% of the total increase in counts occurs near the point of fracture while about 50% of the cumulative energy occurs at initial damage. This result suggests that counts may be more responsive at the end of fatigue life and energy may be more responsive during initial damage. In contrast, feature entropy seems to be more equally responsive for all fatigue damage stages. This means that feature entropy may be better correlated to measured damage and has an advantage over counts and energy.

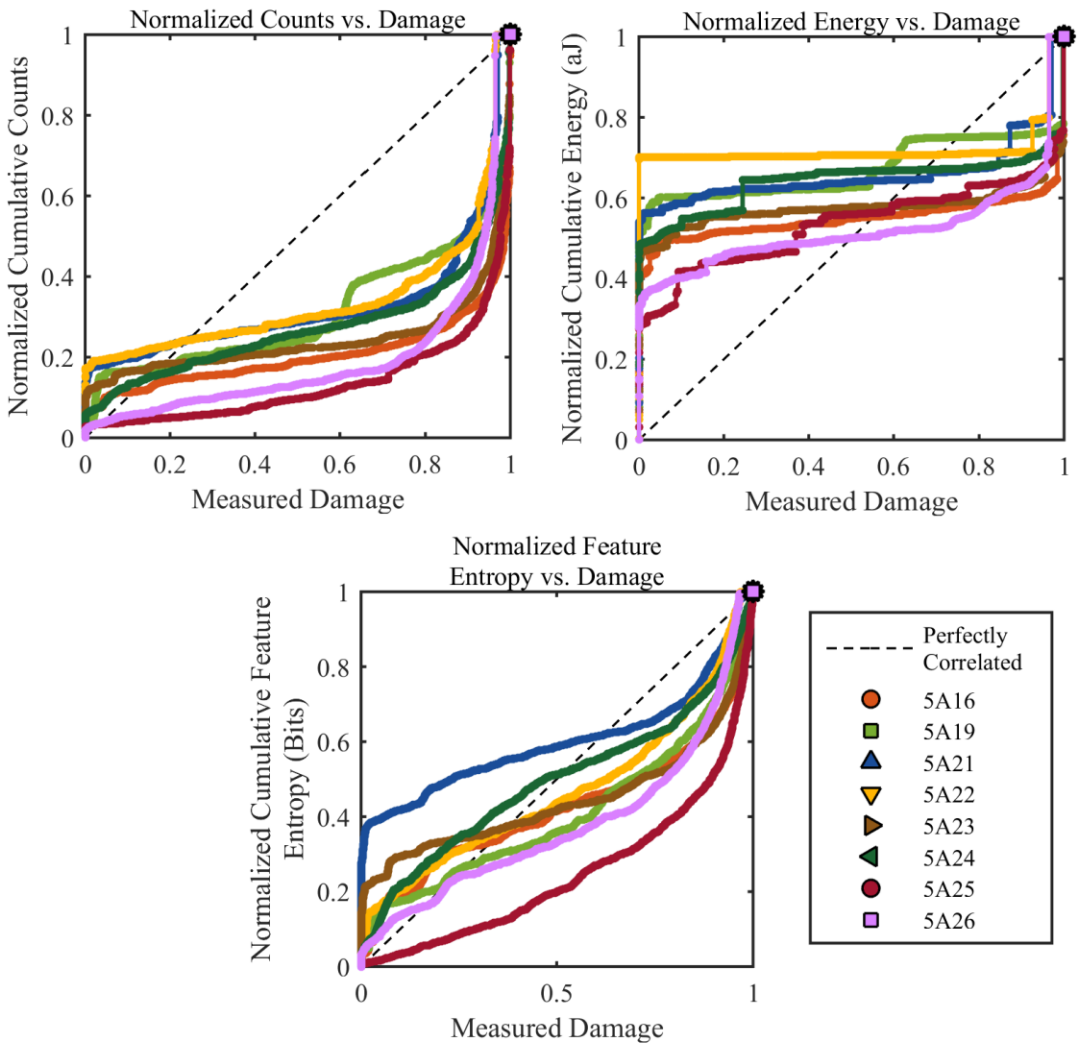

Figure 38: Normalized cumulative counts, energy, and feature entropy with respect to measured damage where a one-to-one relationship is desired

The differences between the cumulative AE parameters damage trends can be quantified by measuring the deviations from the one-to-one ideal relationship. The deviations are measured at each instance of an AE signal. Examples of several deviations are shown in Figure 39 for 5A16's normalized cumulative counts versus damage.

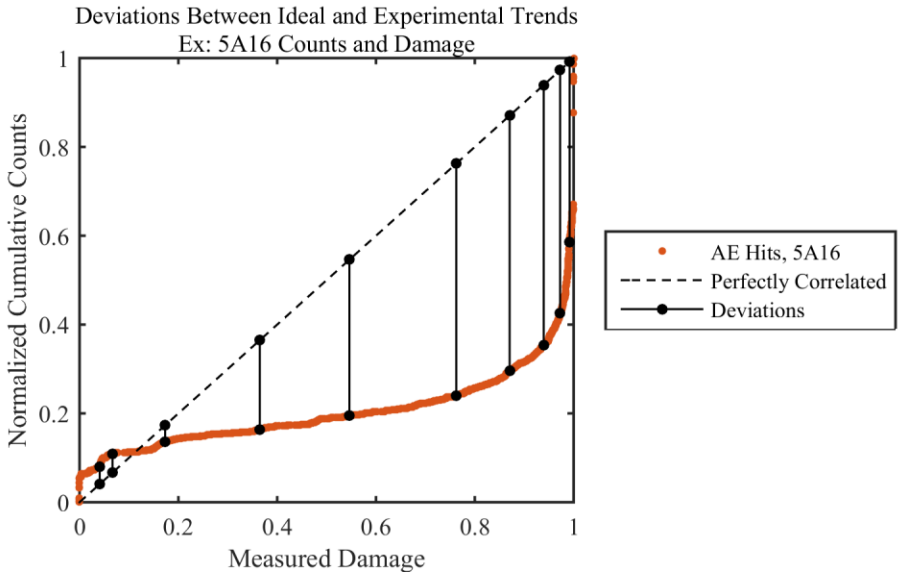

Figure 39: Example of deviations between ideal and experimental trends

The summation of these deviations, referred to as the *deviation factor*, can then be used as a goodness metric of the one-to-one model and compared between the AE parameters for each test. The AE parameter with the lowest deviation factor can be assumed to be a better representation of damage. It should be noted that the deviation factors can only be compared because all AE features are normalized to the same scale and the number of deviations are equal between parameters for each experiments. The deviation factors for each of the experiments and for each of the cumulative AE parameters were calculated and plotted in Figure 40. Results show the deviation factor for feature entropy is lowest for all but one experiment while deviation factors for counts and energy are inconsistently greater and less than one another. This means one could argue feature entropy may be a better statistic of measure damage compared to counts and energy.

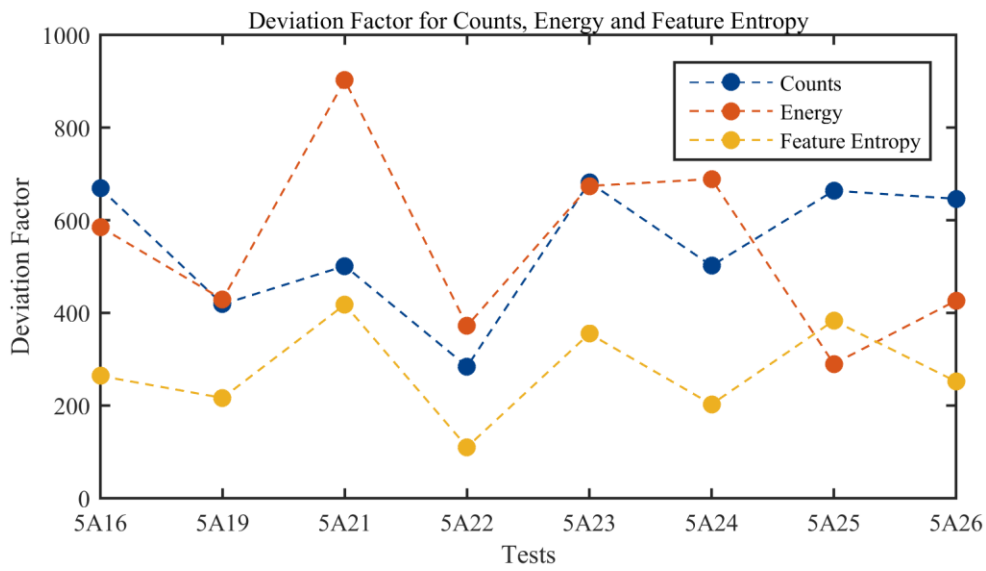

Figure 40: Deviation factor for AE counts, energy, and feature entropy for all experiments

Uncertainty in measured damage and the normalized AE parameters play a role in the experimental results and conclusions. However, if measurement errors were to be reduced in the future, feature entropy may remain a potentially better damage statistic than counts and energy. Overall, each of these cumulative AE parameters show different trends with measured damage meaning each feature contributes different information during various stages of fatigue damage. Therefore, improvements could be made if these three parameters were somehow combined into one metric in the future.

5.5.2 Updated and Temporally Weighted Entropy

The final two AE parameters, updated and temporally weighted entropy, can also be plotted on a normalized scale and compared to measured damage. Because these two types of entropy do not have monotonically increasing trends, it is not expected for these parameters to have a one-to-one relationship with damage. Rather, these plots show a further comparison between the two entropies as well as their

behavior against a normalized damage scale. As such, the plots are shown in Figure 41. One conclusion is that both entropies decrease near zero damage. This decrease is associated with damage prior to a 1 mm crack. Both entropies then increase throughout most of the measured damage which reflect the periods between a 1 mm crack and fracture. In addition, one can see there is more variability between experiments for temporally weighted entropy than updated entropy. This is attributed to temporally weighted entropy being influenced more by the current AE signal voltage distributions and therefore is generally more erratic.

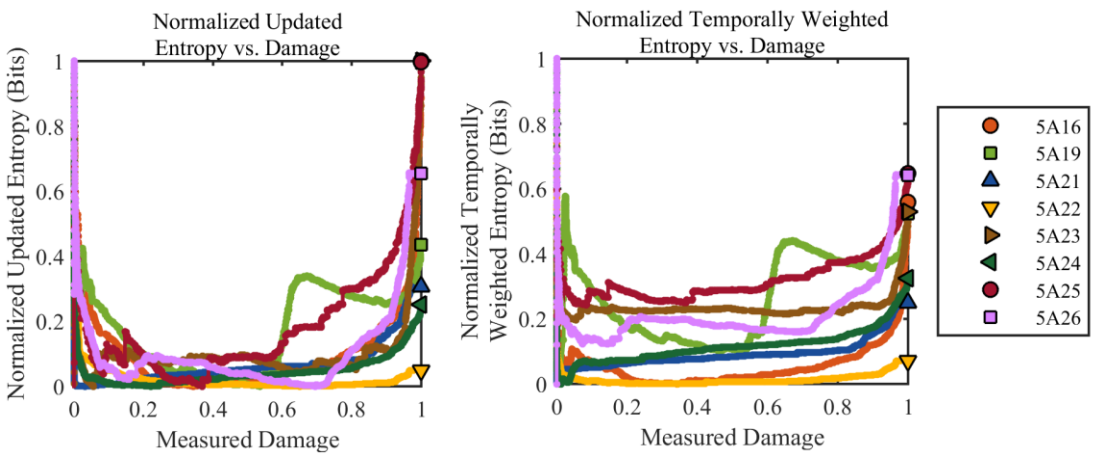

Figure 41: Normalized updated and temporally weighted entropy against measured damage

One could expect these trends to be consistent but more sensitive for future tests that have less measurement uncertainty. For example, if the extensometer was more sensitive to the strain around the notch during crack initiation, then a larger percentage of measured damage would be related to crack initiation rather than crack growth. Thus, the decrease in updated and temporally weighted entropies associated with fatigue damage prior to a 1 mm crack may be more apparent at low measured damage. In the end, updated and temporally weighted entropy are similar to one

another but provide a unique damage trend than the other previously discussed AE parameters.

5.6 Summary of Results

Several conclusions have been made from the experimental results. The following list summarizes all points discussed throughout this chapter.

1. Crack grew through grains and inclusions and caused fatigue striations during stable crack growth.
2. The stress-life trend of the fatigue experiments was fairly similar to the theoretical trend.
3. The instantaneous modulus degradation and its normalized form proved to be a measure of the true fatigue damage, but its utility is limited due to the measurement uncertainty.
4. Cumulative counts, energy, and feature entropy displayed similar cyclic trends with variable final values at specimen fracture. Overall, feature entropy had the most variation which could mean it is a more sensitive damage parameter.
5. Updated and temporally weighted entropy provide unique damage trends and may potentially be used to differentiate between small and large cracks.
6. When normalized and plotted against measured damage, the cumulative feature entropy seems to be better correlated with damage compared to the cumulative counts and energy.

Chapter 6 – Conclusions

6.1 Summary

Cyclic fatigue experiments were performed on Al7075-T6 to investigate potential damage indicators from AE signals prior to the presence of a crack. The experimental procedure was iteratively refined to reduce AE noise and ensure usable data. Two separate theories to measure fatigue damage prior to crack initiation were presented. First, it was assumed that elastic modulus degradation could reflect fatigue damage prior to crack initiation. Second, rather than correlating summary AE features such as AE counts and energy to fatigue damage, more formal measures of disorder inherent in the AE signals, known as information entropy, were developed.

Results showed that the modulus degradation was not significantly responsive to early fatigue damage and was susceptible to measurement errors. However, because AE signals were collected prior to crack initiation, it is likely that AE parameters may act as damage precursors, but their utility is limited by the accuracy in quantifying damage before a visible crack appears. If a more sensitive and more accurate measure of true damage were to be used, it is believe that the presented AE parameters could in fact be damage precursors.

Comparisons between information entropy metrics and traditional AE features concluded that the cumulative feature entropy is similar to cumulative counts and energy, but it may be a more sensitive parameter to experimental variations and be better correlated to damage throughout fatigue life. In addition, updated and temporally weighted entropy produce unique trends that can potentially differentiate between small and large cracks. Since all AE parameters proved to have unique

trends at various damage levels, combining all parameters into one damage metric in the future could be useful. In the end, all of these parameters should be considered in the future stage of STLP testing with more emphasis on feature entropy.

6.2 Contributions

Through the numerous cyclic fatigue experiments performed in this work, several findings were concluded in regards to estimating damage with novel information entropy measures derived from AE signals. The contributions of this work are listed as the following:

1. A major obstacle with using AE signals as an NDE technique is it's susceptibly to extraneous noise. As such, in this research a high-amplitude AE noise was effectively damped below a desired threshold by means of a mechanical damping apparatus and filtered with post-process noise reduction techniques.
2. The use of modulus degradation as a measure of damage prior to a crack was investigated and found to be unresponsive to damage prior to crack initiation. However, the sensitivity of elastic modulus depended on measuring notch strains with a 25 mm gauge length extensometer. As such, modulus degradation as a measure of damage remains a feasible option if a more sensitive method to measure strain was employed in the future.
3. Three different methods to estimate the information content or the disorder from AE signals were proposed. Rather than accepting AE summary statistics, such as counts and energy as fully informative damage measures, information entropy is calculated based on the raw voltage data from each recorded AE

signal. In turn, it is shown that the proposed feature entropy better correlates with the fatigue damage than the AE counts and energy, while the proposed updated and temporally weighted entropy methods provide a unique damage trend that could differentiate between small and large cracks.

6.3 Future Work

Numerous directions are possible to extend this research pertaining to both conclusively determining AE damage precursors as well as the second stage of the project. These are outlined below.

1. Damage prior to crack initiation needs to be accurately and repeatedly measured or estimated. While still acting on the idea that modulus degrades prior to crack initiation, improvements could be made to measuring the strain around the notch. This can be done with an extensometer with a smaller gauge length, using strain gauges if they are ensured to not interact with AE signals or detach during the tests, or a highly accurate and fast DIC. The uncertainty in measured damage at certain damage levels would decrease if the crack length could be better monitored by monitoring the crack from multiple perspectives.
2. Other methods of estimating damage prior to a fatigue crack could be explored. The replica method employed by Newman [16,17,18] could be an option in which cyclic loading is repeatedly paused, the notch region is replicated with silicon-rubber, and then observed under high magnification. Another method, which was based on replicas, is to model fatigue damage with FASTRAN software. This software was developed

for small cracks, so while damage prior to a crack may not be able to be estimated, very small cracks can be modeled. Finally, simulations similar to those proposed in [25, 45, 46] could be used to model the atomic interactions during fatigue and those estimate damage prior to a crack.

3. Error in the measured damage at supposedly consistent damage levels at certain crack lengths is mainly attributed to measuring crack lengths on one side of the specimen as cracks propagating unevenly. This phenomenon is believed to be caused by a slight bending moment applied to the specimens due to misalignment of test grips. To limit the bending moment effect on crack growth behavior in axially-loaded fatigue tests, thicker specimens could be designed and tested in the future.
4. Once one or a few accurate measures of damage prior to a crack are found, then experiments should be performed while damage is measured and AE signals are collected. Then, the various information entropy metrics should be calculated and correlated to the more accurate measured damage.
5. Rather than using resonant sensors to detect AE signals, wideband sensors could be used in the future. Wideband sensors better reconstruct the received acoustic wave with respect to the frequency behavior. Therefore, more analysis could be performed in the frequency domain similar to those in previous work [35, 39, 52].
6. Other damage precursors could be investigated along with AE signals including strain energy dissipation and thermodynamic entropy. These two

measures proved to be correlated to fatigue damage at crack initiation [78] and could be combined and compared with all AE damage parameters.

7. Fatigue damage precursors could be combined into one damage statistic in the future. One possible method is to use an extended Kalman filter which utilizes recursive Bayesian estimation to reduce uncertainty. It has been used successfully in combining AE counts and crack length inspections to better estimate crack growth rate [79].
8. Finally, altering the current experimental setup used for coupon testing to be used for larger-scale testing should be considered. Most notably, the damage apparatus was designed to limit the mechanical noise from the servo-hydraulic testing machine. However, in a different experimental configuration, one should expect that the AE background noise to be different and would need to consider how to account for noisy AE signals.

Appendices

Appendix A – Applied Load vs. Signal Arrival Time Scatter Plots

This appendix shows the applied load and time for each AE hit. These plots were used to filter noise. For tests with no filtering or unfilterable noise, only one plot is presented. For tests with filtering, before and after graphs are provided.

5A7 – Unfilterable

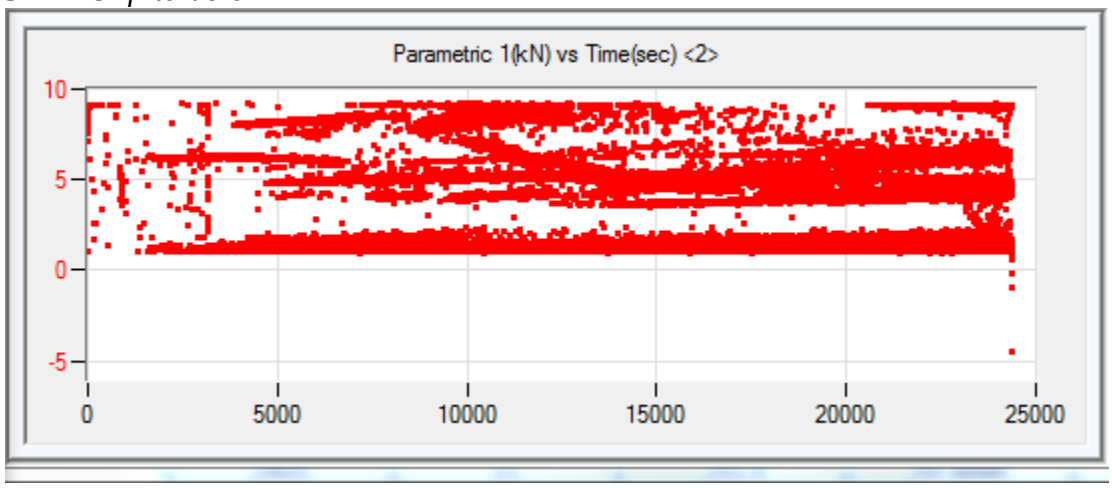

5A15 – Unfilterable

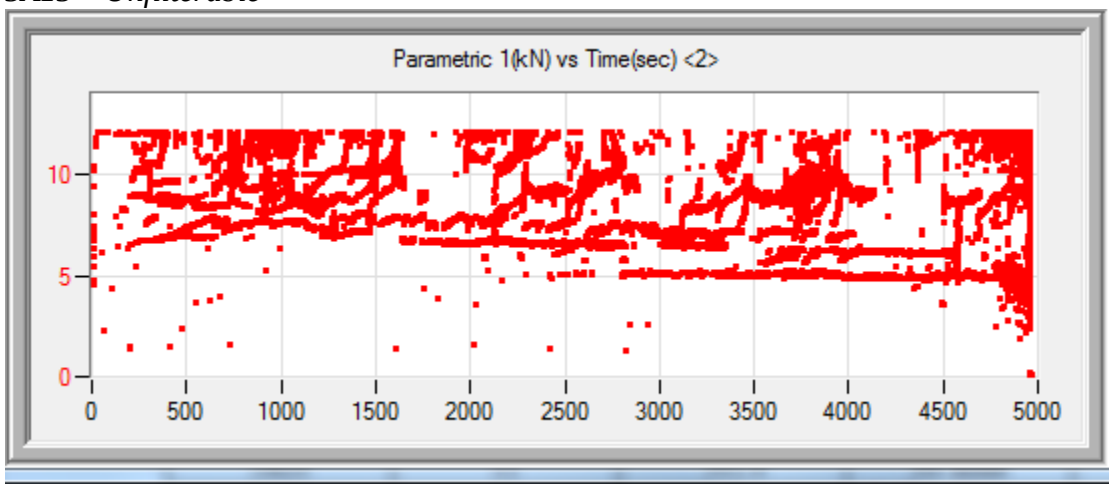

5A16 – Before Filtering

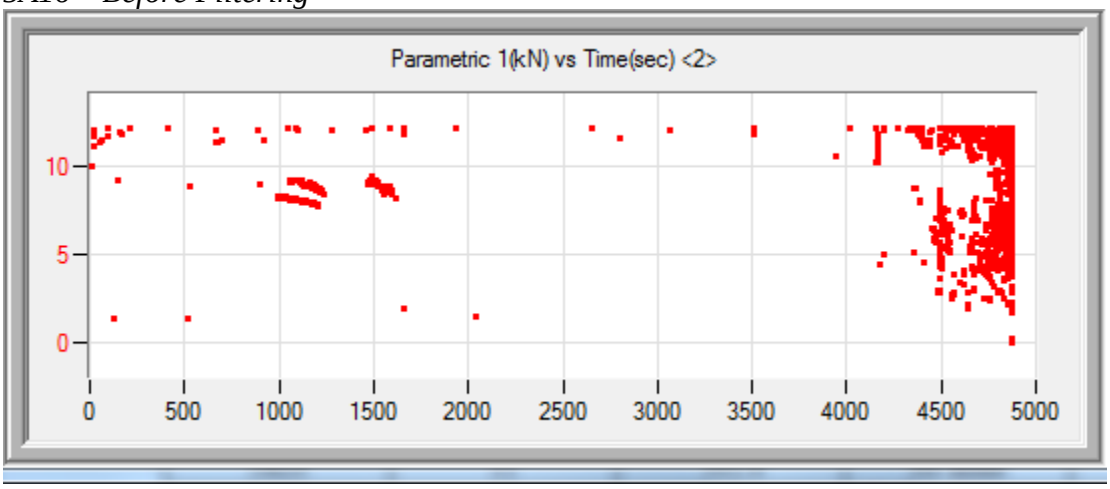

5A16 – After Filtering

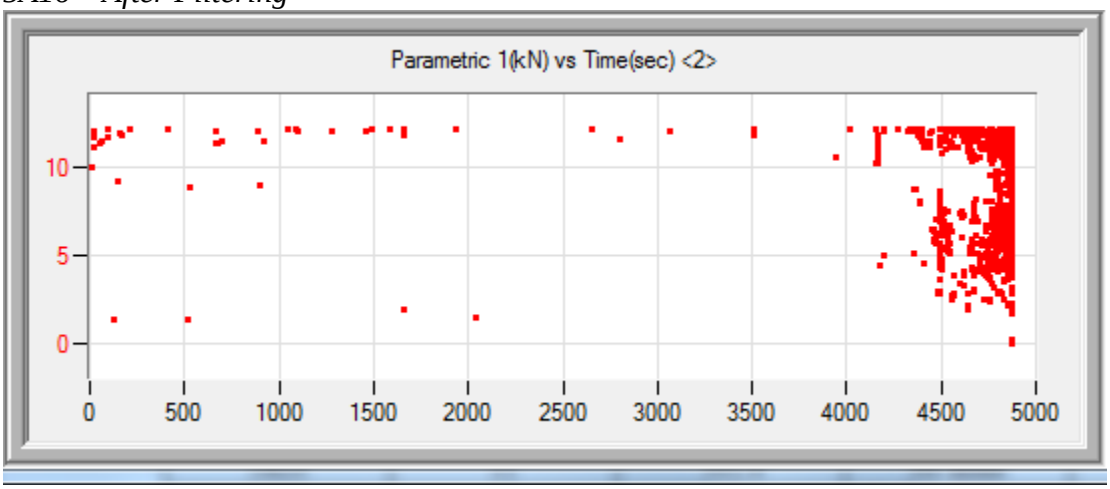

5A19 – Before Filtering

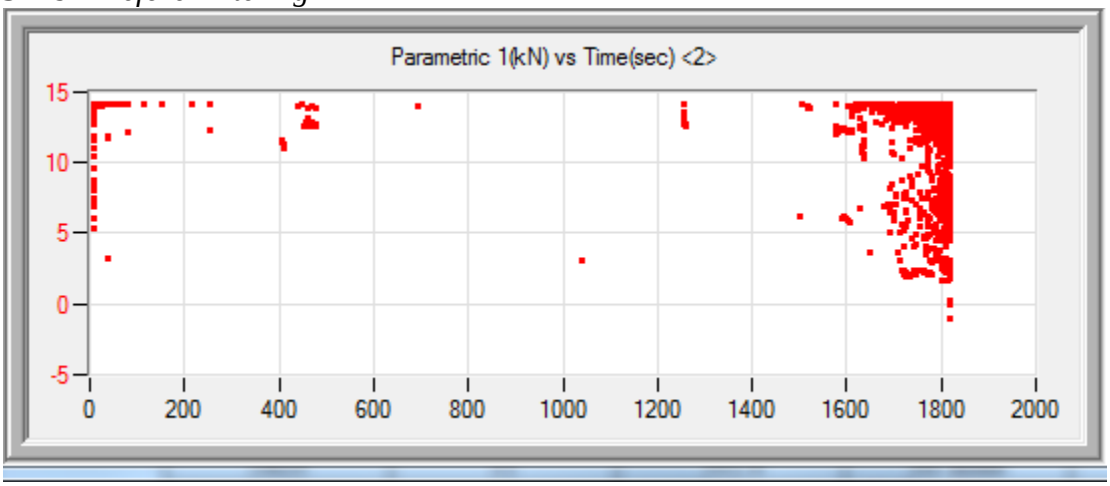

5A19 – After Filtering

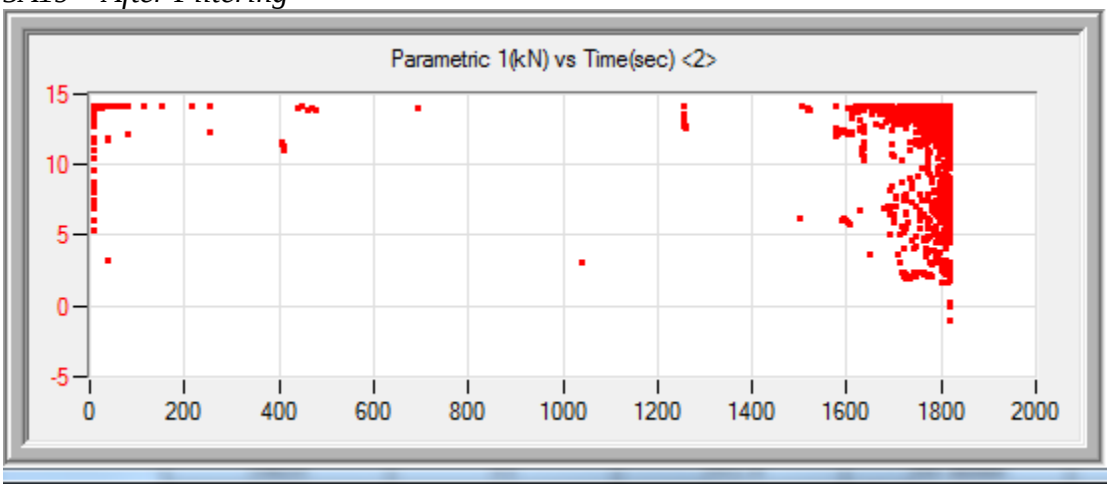

5A20 – Unfilterable

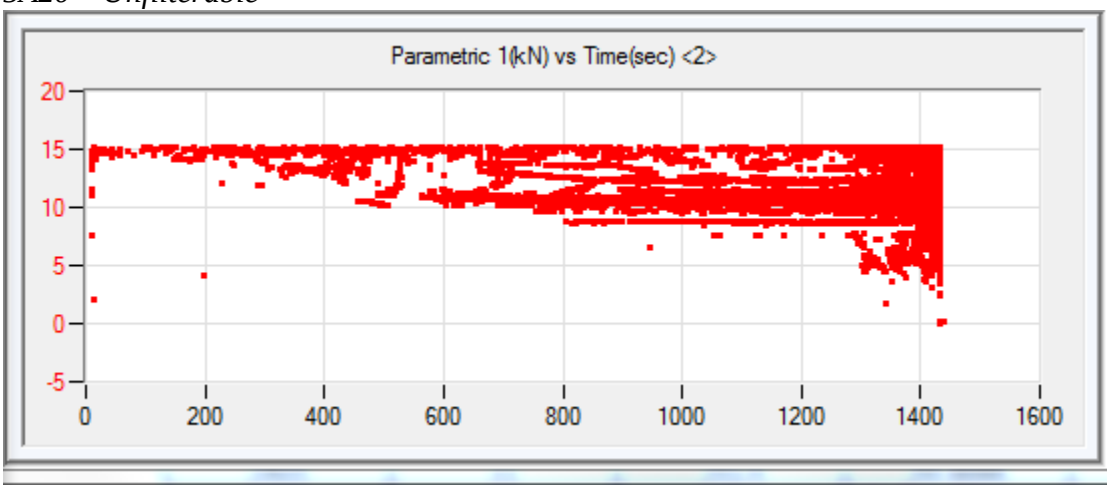

5A21 – Before Filtering

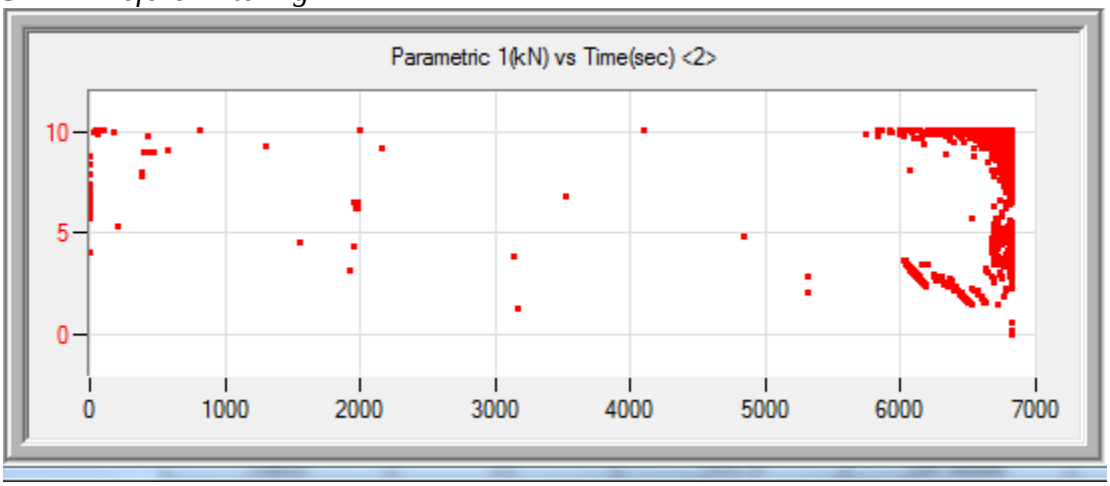

5A21 – After Filtering

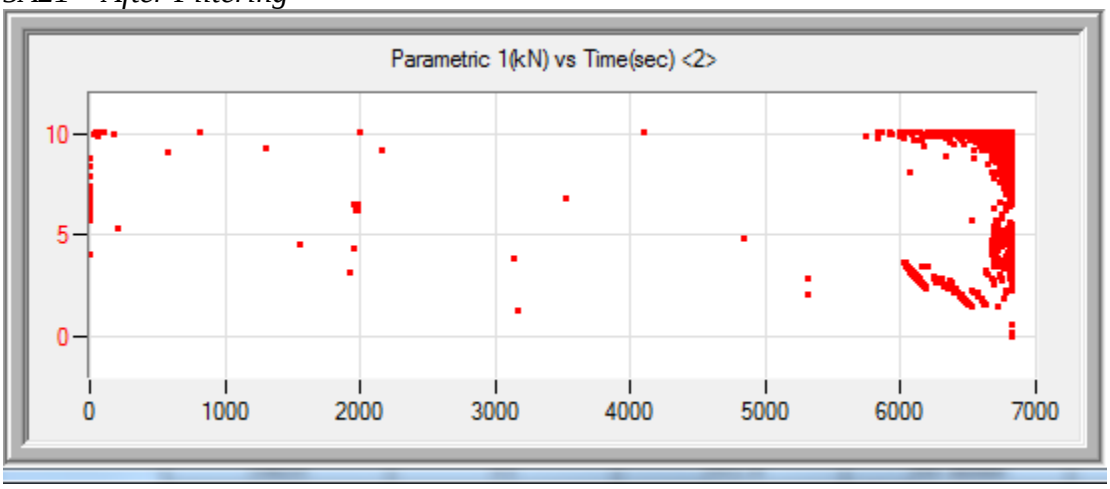

5A22 – Before Filtering

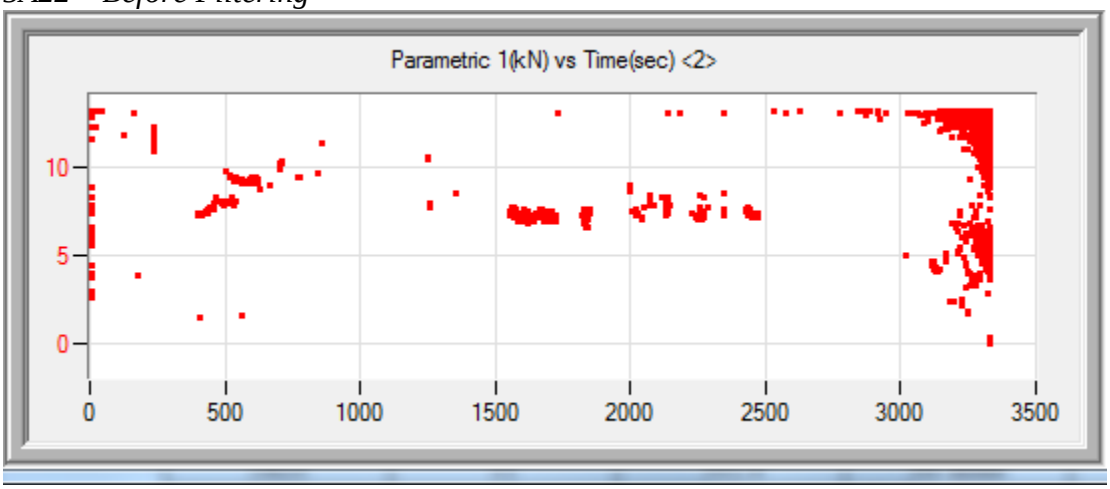

5A22 – After Filtering

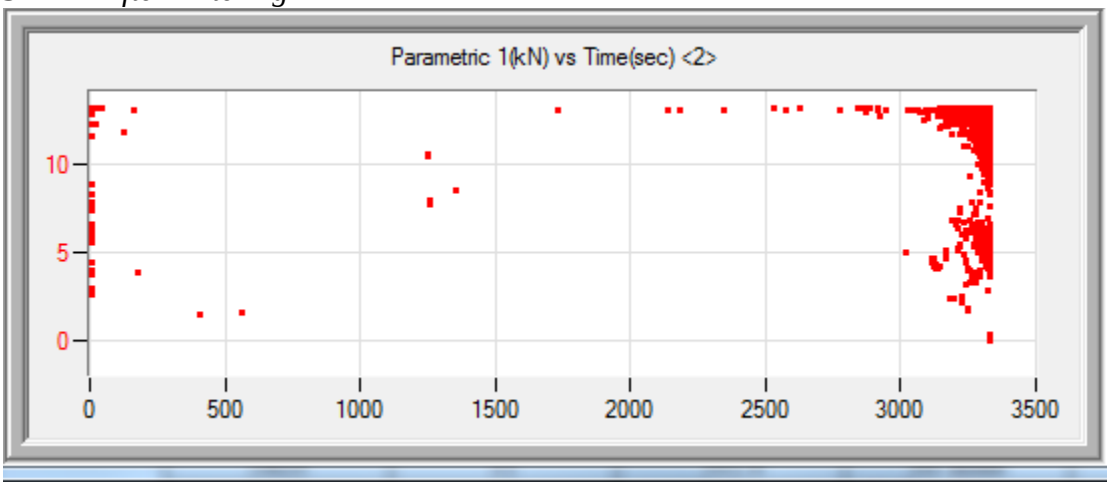

5A23 – Before Filtering

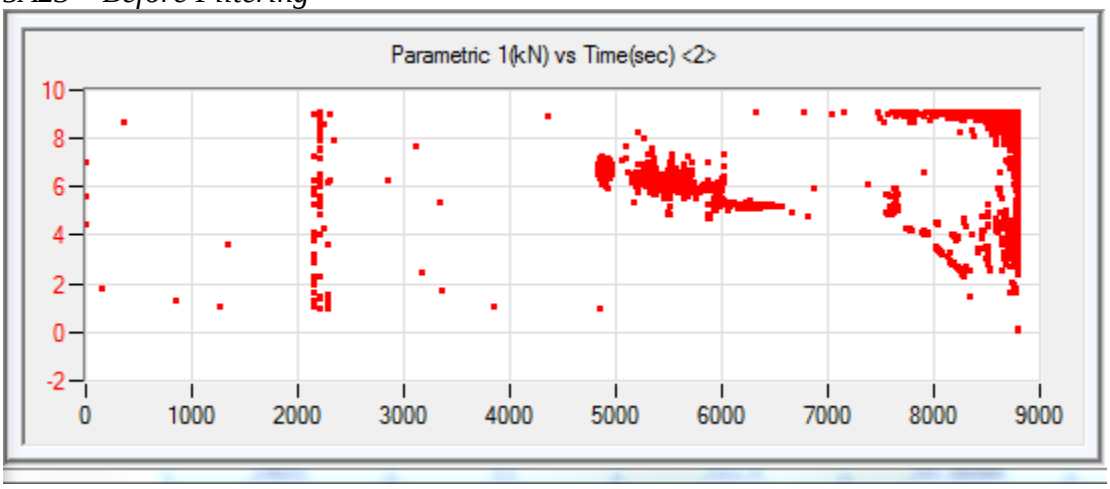

5A23 – After Filtering

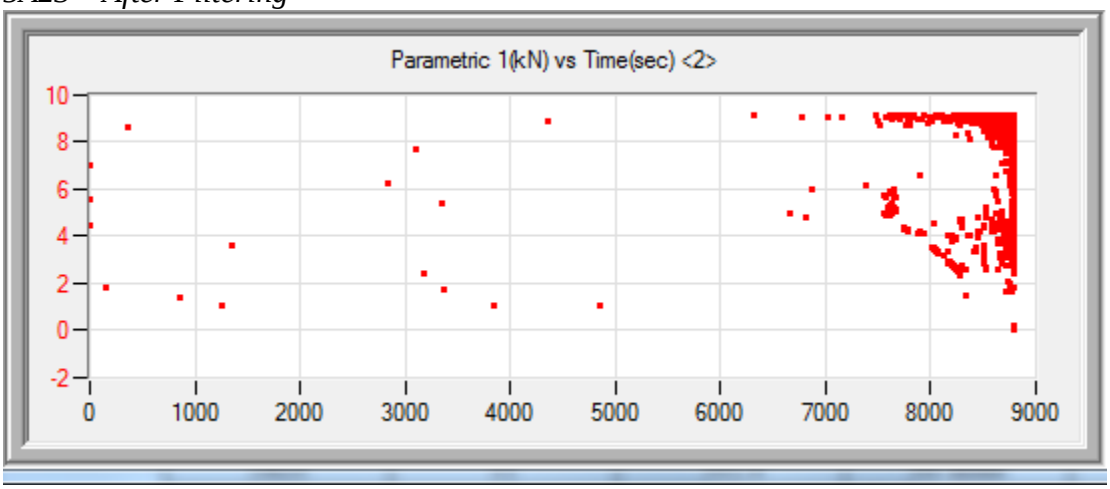

5A24 – Before Filtering

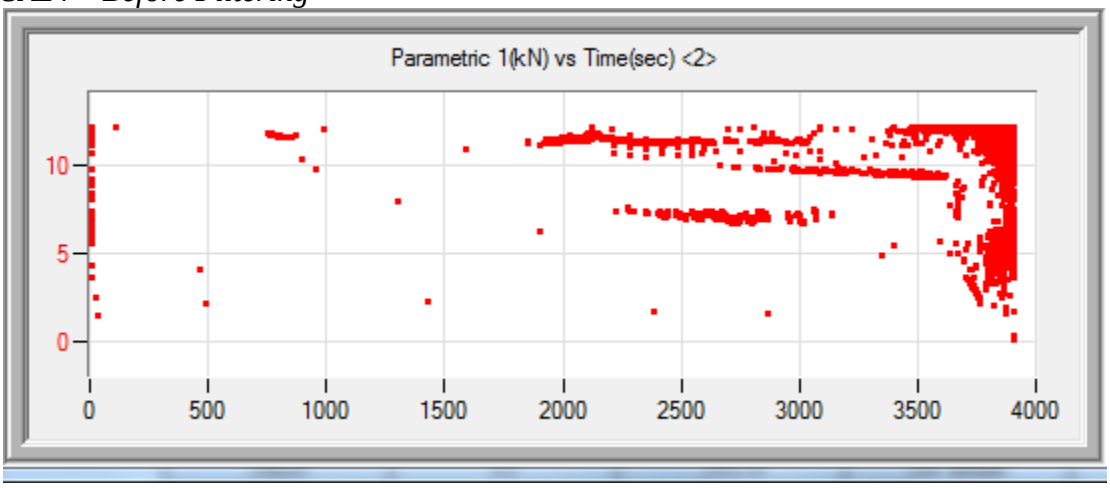

5A24 – After Filtering

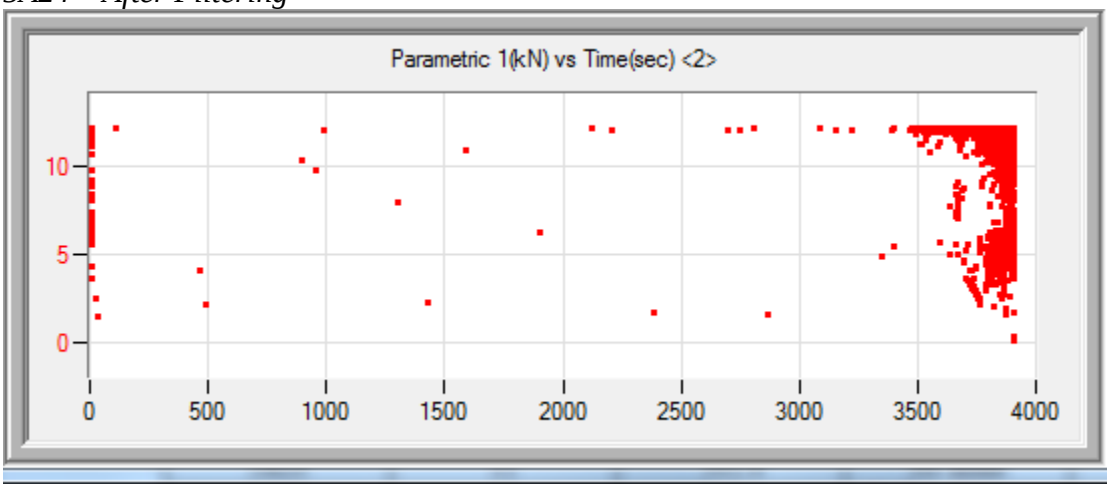

5A25 – No Filtering Needed

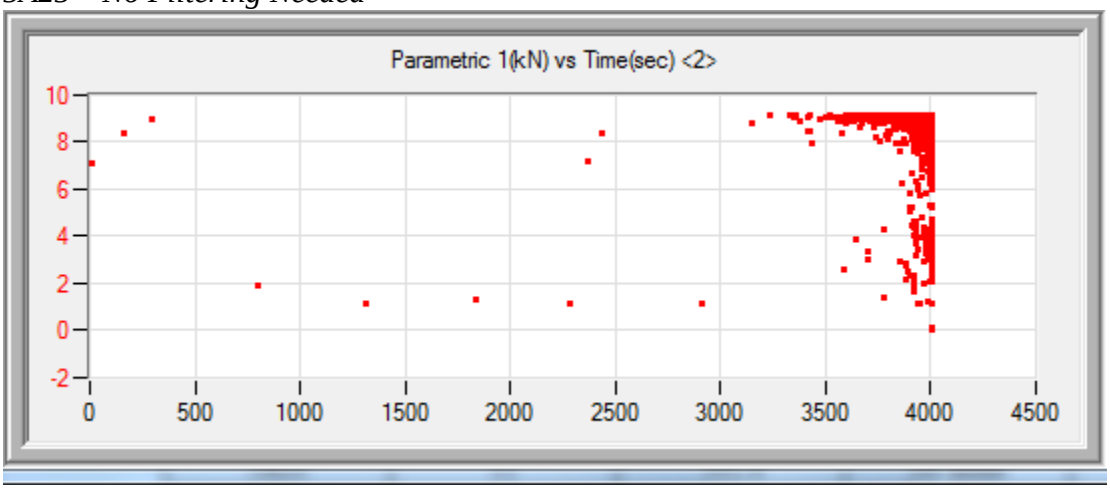

5A25 – No Filtering Needed

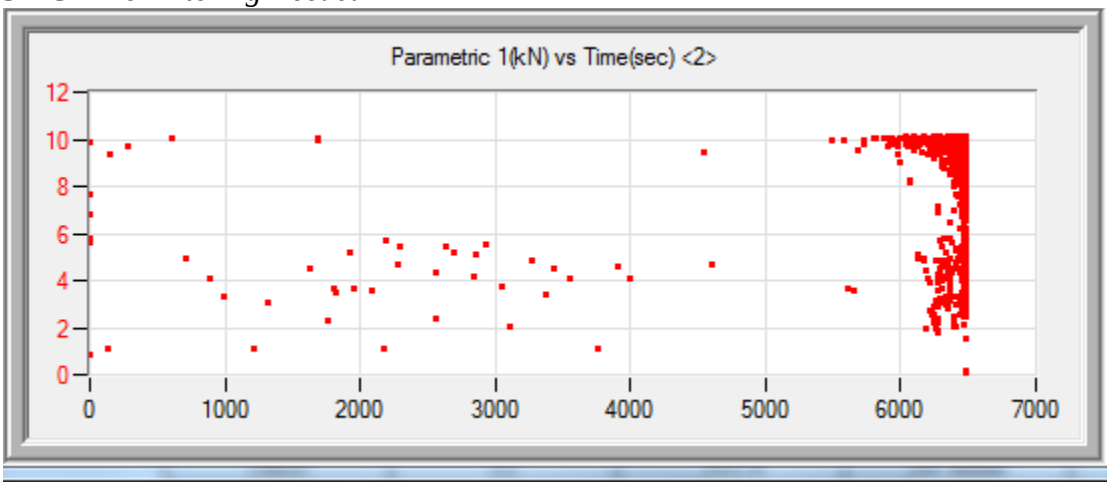

Appendix B – Code for Modulus Evolution

```
%% Strain and Modulus Calculation
clear all

%% Load Raw Data
% Experiments to find modulus degradation from
testLabels = [16 19 21 22 23 24 25 26];
% Find number of tests to be analyzed
numOfTests = length(testLabels);
% Pre allocate arrays
MTS = cell(1,numOfTests);
timeA = cell(1,numOfTests);
cyclesA = cell(1,numOfTests);
posA = cell(1,numOfTests);
loadA = cell(1,numOfTests);
extenA = cell(1,numOfTests);

% The data from the MTS machine is set up so that the first 5 seconds, the
% specimen is fully unloaded to 0 kN. Then the specimen is loaded to the
% minimum load. Then fatigue begins. Therefore, need to find the exact time
% when cyclic fatigue begins. This is done by plotting the data and finding
% the start time.
peakTimeMTS = [10.36 10.36 10.44 10.35 10.39 10.35 10.37 10.40];

% Load data from raw csv files
for j = 1:numOfTests
    begName = 'C:\Users\Lab Admin\Documents\AAAFiles,
040816\5_StrainCalc\Test1.steps.tracking_5A';
    fileIndex = num2str(testLabels(j));
    fileName = strcat(begName,fileIndex,'.csv');
    MTS{1,j} = csvread(fileName,1,0);
    timeA{1,j} = MTS{1,j}(:,1)-peakTimeMTS(j);
    cyclesA{1,j} = MTS{1,j}(:,6);
    posA{1,j} = MTS{1,j}(:,7);
    loadA{1,j} = MTS{1,j}(:,8);
    extenA{1,j} = MTS{1,j}(:,9);
    % Display the test as it has finished loading data
    disp(testLabels(j))
end

%% Input Constants
% Average thickness for each specimen found after three measurements around
% the notch with calibers
t = [3.157 3.157 3.15 3.15 3.163 3.16 3.157 3.167]; % mm
% Average width of specimens after three measurements
w = [18.07 18.137 18.057 18.027 18.053 18.067 18.073 18.063]; %mm
% Maximum applied load for each test
maxLoad = [12 14 10 13 9 12 9 10]; %kN
% Extensometer gauge length
localGaugeL = 25; %mm
% Estimated times when a crack initiated, was 0.25 mm, and was 1 mm from
% crack growth images. Went picture by picture until a crack of these
% lengths were measured with ImageJ.
crackInitTime = [4200 1582 4950 3130 6329 3420 3638 5822]; %s
crack025mmTime = [4260 1697 5612 3145 7276 3505 3682 6067]; %s
crack1mmTime = [4410 1757 6343 3231 8099 3701 3939 6222]; %s

%% Calculate stress, strain, modulus, measured damage
% Put specimen names into cell array Preallocate
```

```
maxim = cell(1,length(testLabels));
minim = cell(1,length(testLabels));
maxLoc = cell(1,length(testLabels));
minLoc = cell(1,length(testLabels));
posInv = cell(1,length(testLabels));
maxInd = zeros(1,length(testLabels));
minInd = zeros(1,length(testLabels));
firstMaxLoc = zeros(1,length(testLabels));
firstMinLoc = zeros(1,length(testLabels));
redPosMaxim = cell(1,length(testLabels));
redPosMinim = cell(1,length(testLabels));
redLoadMaxim = cell(1,length(testLabels));
redLoadMinim = cell(1,length(testLabels));
redExtenMaxim = cell(1,length(testLabels));
redExtenMinim = cell(1,length(testLabels));
graphTimeInd = cell(1,length(testLabels));
deltaPos = cell(1,length(testLabels));
deltaLoad = cell(1,length(testLabels));
deltaExten = cell(1,length(testLabels));
deltaStress = cell(1,length(testLabels));
localStrain = cell(1,length(testLabels));
modulus = cell(1,length(testLabels));
modTime = cell(1,length(testLabels));
changeInMod = cell(1,length(testLabels));
damage =  cell(1,length(testLabels));
initModulus = zeros(1,length(testLabels));
indCrackInitTime = zeros(length(testLabels),1);
indCrack025mmTime = zeros(length(testLabels),1);
indCrack1mmTime = zeros(length(testLabels),1);

for i = 1:length(testLabels)

    % Finding the max and min position values and their indices
    [maxim{1,i},maxLoc{1,i}] = findpeaks(posA{1,i});
    posInv{1,i} = 1.01*max(posA{1,i}) - posA{1,i};
    [minim{1,i},minLoc{1,i}] = findpeaks(posInv{1,i});
    minim{1,i} = posA{1,i}(minLoc{1,i});

    % Need to "line-up" the max and min position values with their cycles.
    % If there are a different number of maxs and mins, need to figure out
    % which ones should line up. This is what the next few lines and the if
    % loop do.

    % Getting the length of each max and min position vector
    maxInd(i) = length(maxLoc{1,i});
    minInd(i) = length(minLoc{1,i});
    % Getting the indice for the first max and min values
    firstMaxLoc(i) = maxLoc{1,i}(1);
    firstMinLoc(i) = minLoc{1,i}(1);
    % Ensure you get matching minimums and maximums during increasing part
    % of the cycle. Then calculate the deltaPosition and deltaLoads based
    % on the "matched-up" maxs and mins. Also identify the time for each
    % start of the cycle (time at the minimum values)
    if maxInd(i)> minInd(i) && firstMaxLoc(i) < firstMinLoc(i)
        redPosMaxim{1,i} = maxim{1,i}(2:end);
        redPosMinim{1,i} = minim{1,i}(1:end);
        redLoadMaxim{1,i} = loadA{1,i}(maxLoc{1,i}(2:end));
        redLoadMinim{1,i} = loadA{1,i}(minLoc{1,i}(1:end));
        redExtenMaxim{1,i} = extenA{1,i}(maxLoc{1,i}(2:end));
        redExtenMinim{1,i} = extenA{1,i}(minLoc{1,i}(1:end));
        graphTimeInd{1,i} = minLoc{1,i}(1:end);
        disp([i,1])
```

```
    elseif maxInd(i) == minInd(i) && firstMaxLoc(i) < firstMinLoc(i)
        redPosMaxim{1,i} = maxim{1,i}(2:end);
        redPosMinim{1,i} = minim{1,i}(1:end-1);
        redLoadMaxim{1,i} = loadA{1,i}(maxLoc{1,i}(2:end));
        redLoadMinim{1,i} = loadA{1,i}(minLoc{1,i}(1:end-1));
        redExtenMaxim{1,i} = extenA{1,i}(maxLoc{1,i}(2:end));
        redExtenMinim{1,i} = extenA{1,i}(minLoc{1,i}(1:end-1));
        graphTimeInd{1,i} = minLoc{1,i}(1:end-1);
        disp([i,2])
    elseif maxInd(i) < minInd(i) && firstMaxLoc(i) > firstMinLoc(i)
        redPosMaxim{1,i} = maxim{1,i}(1:end);
        redPosMinim{1,i} = minim{1,i}(1:end-1);
        redLoadMaxim{1,i} = loadA{1,i}(maxLoc{1,i}(1:end));
        redLoadMinim{1,i} = loadA{1,i}(minLoc{1,i}(1:end-1));
        redExtenMaxim{1,i} = extenA{1,i}(maxLoc{1,i}(1:end));
        redExtenMinim{1,i} = extenA{1,i}(minLoc{1,i}(1:end-1));
        graphTimeInd{1,i} = minLoc{1,i}(1:end-1);
        disp([i,3])
    elseif maxInd(i) == minInd(i) && firstMaxLoc(i) > firstMinLoc(i)
        redPosMaxim{1,i} = maxim{1,i}(1:end);
        redPosMinim{1,i} = minim{1,i}(1:end);
        redLoadMaxim{1,i} = loadA{1,i}(maxLoc{1,i}(1:end));
        redLoadMinim{1,i} = loadA{1,i}(minLoc{1,i}(1:end));
        redExtenMaxim{1,i} = extenA{1,i}(maxLoc{1,i}(1:end));
        redExtenMinim{1,i} = extenA{1,i}(minLoc{1,i}(1:end));
        graphTimeInd{1,i} = minLoc{1,i}(1:end);
        disp([i,4])
    end
    deltaPos{1,i} = redPosMaxim{1,i}-redPosMinim{1,i};
    deltaExten{1,i} = redExtenMaxim{1,i}-redExtenMinim{1,i};
    deltaLoad{1,i} = redLoadMaxim{1,i}-redLoadMinim{1,i};

    % From deltaPos, deltaExten, and deltaLoad, get stress, strain,
    % modulus, change in modulus, and measured damage
    deltaStress{1,i} = deltaLoad{1,i}./(t(i)*w(i))*1000; %MPa =
kN/mm/mm*1000
    localStrain{1,i} = deltaExten{1,i}./localGaugeL; %mm/mm
    modulus{1,i} = deltaStress{1,i}./localStrain{1,i};
    modTime{1,i} = timeA{1,i}(graphTimeInd{1,i});
    % Normalize modulus
    initModulus(1,i) = mean(modulus{1,i}(180:480))/1000;
    damage{1,i} = (modulus{1,i}(180:end-20)./1000-
initModulus(i))./(modulus{1,i}(end-20)/1000-initModulus(i));


    % Find the time indices for modulus where crack initiates, grows to 0.25
    % and to 1 mm.
    indCrackInitTime(i) = find(modTime{1,i}>crackInitTime(i),1);
    indCrack025mmTime(i) = find(modTime{1,i}>crack025mmTime(i),1);
    indCrack1mmTime(i) = find(modTime{1,i}>crack1mmTime(i),1);
    stopInd4(i,1) = length(modTime{1,i}); %Fracture
end
```

Appendix C – Error Propagation

C.1 Initial Elastic Modulus

$$For\ A = t * w,\ \delta A = |A|\sqrt{\left(\frac{\delta t}{|t|}\right)^2 + \left(\frac{\delta w}{|w|}\right)^2} \quad \text{(C.1)}$$

Test	t (mm)	δt (mm)	w (mm)	δw (mm)	A (mm^2)	δA (mm^2)
5A16	3.16	0.01	18.07	0.01	57.05	0.183
5A19	3.16	0.01	18.14	0.01	57.26	0.184
5A21	3.15	0.01	18.06	0.01	56.88	0.183
5A22	3.15	0.01	18.03	0.01	56.79	0.183
5A23	3.16	0.01	18.05	0.01	57.10	0.183
5A24	3.16	0.01	18.07	0.01	57.09	0.183
5A25	3.16	0.01	18.07	0.01	57.06	0.183
5A26	3.17	0.01	18.06	0.01	57.21	0.183

$$For\ \Delta P = P_{max} - P_{min},\ \delta\Delta P = \sqrt{(\delta P_{max})^2 + (\delta P_{min})^2} \quad \text{(C.2)}$$

Test	Pmax (kN)	δPmax (kN)	Pmin (kN)	δPmin (kN)	ΔP (kN)	δΔP (kN)
5A16	12.0	0.036	1.20	0.0096	10.80	0.037
5A19	14.0	0.042	1.40	0.0112	12.60	0.043
5A21	10.0	0.03	1.00	0.008	9.00	0.031
5A22	13.0	0.039	1.30	0.0104	11.70	0.040
5A23	9.0	0.027	0.90	0.0072	8.10	0.028
5A24	12.0	0.036	1.20	0.0096	10.80	0.037
5A25	9.0	0.027	0.90	0.0072	8.10	0.028
5A26	10.0	0.03	1.00	0.008	9.00	0.031

Test	Lo (mm)	δLo (mm)	lmax (mm)	δlmax (mm)	lmin (mm)	δlmin (mm)
5A16	25	0.002	0	0.00186	-0.07	0.00186
5A19	25	0.002	0.084	0.00186	0.005	0.00186
5A21	25	0.002	-0.025	0.00186	-0.082	0.00186
5A22	25	0.002	-0.02	0.00186	-0.093	0.00186
5A23	25	0.002	0.034	0.00186	-0.018	0.00186
5A24	25	0.002	-0.009	0.00186	-0.078	0.00186
5A25	25	0.002	0.038	0.00186	-0.012	0.00186
5A26	25	0.002	0.014	0.00186	-0.042	0.00186

$$For\ \Delta l = l_{max} - l_{min},\ \delta\Delta l = \sqrt{(\delta l_{max})^2 + (\delta l_{min})^2} \quad \text{(C.3)}$$

$$For\ \Delta\varepsilon = \frac{\Delta l}{L_o},\ \delta\Delta\varepsilon = |\Delta\varepsilon|\sqrt{\left(\frac{\delta\Delta l}{|\Delta l|}\right)^2 + \left(\frac{\delta L_o}{|L_o|}\right)^2} \quad \text{(C.4)}$$

$$For\ E = {\Delta P * L_o}/{\Delta l * A}, \delta E = |E|\sqrt{\left(\frac{\delta\Delta P}{|\Delta P|}\right)^2 + \left(\frac{\delta L_o}{|L_o|}\right)^2 + \left(\frac{\delta\Delta l}{|\Delta l|}\right)^2 + \left(\frac{\delta A}{|A|}\right)^2} \quad \text{(C.5)}$$

Test	Δl (mm)	δΔl (mm)	ΔStrain (mm/mm)	δDeltastrain (mm)	E (GPa)	δE (GPa)
5A16	0.070	0.00263	0.00280	0.000105	67.6	2.6
5A19	0.079	0.00263	0.00316	0.000105	69.6	2.3
5A21	0.057	0.00263	0.00228	0.000105	69.4	3.2
5A22	0.073	0.00263	0.00292	0.000105	70.6	2.6
5A23	0.052	0.00263	0.00208	0.000105	68.2	3.5
5A24	0.069	0.00263	0.00276	0.000105	68.5	2.6
5A25	0.050	0.00263	0.00200	0.000105	71.0	3.7
5A26	0.056	0.00263	0.00224	0.000105	70.2	3.3

C.2 Measured Crack Length

*The DIC was used for crack monitoring of 5A16 where the notch was in full view and the picture scale could be directly estimated

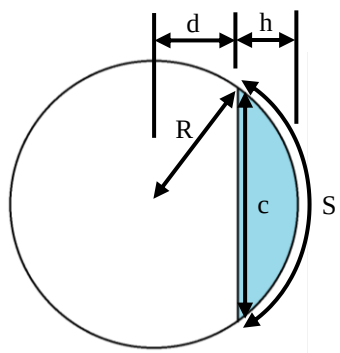

$$For\ c^2,\ \delta c^2 = 2 * c * \delta c \quad \text{(C.6)}$$

Test	R (mm)	δR (mm)	c (pixels)	δc (pixel)	h (pixels)	δh (pixels)	c^2 (pixels/mm)	δc^2 (pixels)
5A16*	1	0.05	-	-	-	-	-	-
5A19	1	0.05	774.7	4	122.7	4	600160	6198
5A21	1	0.05	712	4	93.3	4	506944	5696
5A22	1	0.05	768	4	112	4	589824	6144
5A23	1	0.05	786	4	132	4	617796	6288
5A24	1	0.05	546	4	57	4	298116	4368
5A25	1	0.05	695	4	110.7	4	483025	5560
5A26	1	0.05	754.7	4	108	4	569572	6038

$$For\ \frac{c^2}{8h},\ \delta\frac{c^2}{8h} = \left|\frac{c^2}{8h}\right|\sqrt{\left(\frac{\delta c^2}{|c^2|}\right)^2 + \left(\frac{\delta h}{|h|}\right)^2} \quad \text{(C.7)}$$

$$For\ \frac{c^2}{8h} + \frac{h}{2},\ \delta\left(\frac{c^2}{8h} + \frac{h}{2}\right) = \sqrt{\left(\delta\frac{c^2}{8h}\right)^2 + (\delta h)^2} \quad \text{(C.8)}$$

$$For\ Scale = \frac{\left(\frac{c^2}{8h}+\frac{h}{2}\right) pixels}{R\ mm},\ \delta Scale = |Scale|\sqrt{\left(\frac{\delta\left(\frac{c^2}{8h}+\frac{h}{2}\right)}{\left|\left(\frac{c^2}{8h}+\frac{h}{2}\right)\right|}\right)^2 + \left(\frac{\delta R}{|R|}\right)^2} \quad \text{(C.9)}$$

Test	$c^2/8h$ (pixels)	$\delta c^2/8h$ (pixels)	Numerator (pixel)	δNumerator (pixels)	Scale (pix/mm)	δScale (pix/mm)
5A16*	-	-	-	-	24.65	2
5A19	611.4	20.9	672.8	31.9	672.8	46.3
5A21	679.2	30.1	725.8	44.8	725.8	57.6
5A22	658.3	24.5	714.3	36.8	714.3	51.3
5A23	585.0	18.7	651.0	28.7	651.0	43.4
5A24	653.8	46.9	682.3	68.4	682.3	76.5
5A25	545.4	20.7	600.8	31.5	600.8	43.5
5A26	659.2	25.4	713.2	38.1	713.2	52.2

$$For\ Crack\ Length = \frac{CL\ (pixels)}{Scale\ (\frac{pixels}{mm})},\ \delta CL = |CL|\sqrt{\left(\frac{\delta(CL)}{|CL|}\right)^2 + \left(\frac{\delta Scale}{|Scale|}\right)^2} \quad \text{(C.10)}$$

Test	0.25 mm crack (mm)	δ0.25 mm crack (mm)	1 mm crack (mm)	δ1 mm crack (mm)	%error in 0.25 mm	% error in 1 mm
5A16	0.268	0.084	1.078	0.120	31.3	11.1
5A19	0.272	0.020	1.036	0.072	7.2	6.9
5A21	0.239	0.020	1.011	0.080	8.3	8.0
5A22	0.249	0.019	1.1	0.080	7.5	7.2
5A23	0.258	0.018	1.041	0.070	7.1	6.7
5A24	0.262	0.030	1.065	0.120	11.4	11.2
5A25	0.256	0.020	1.094	0.080	7.7	7.3
5A26	0.26	0.020	1.074	0.080	7.6	7.3

Appendix D – Code for AE Entropy Formulations

```
%% Entropy From AE Signals
clear all
clc

% Used as a reference for chooseTestInd
% 1 | 5A4
% 2 | 5A6
% 3 | 5A10
% 4 | 5A16
% 5 | 5A19
% 6 | 5A21
% 7 | 5A22
% 8 | 5A23
% 9 | 5A24
% 10 | 5A25
% 11 | 5A26

%% Setup
% Choose which test to get entropy from
chooseTestInd = 1; % out of 11
channel = 2; % 1 or 2
sizeOfWaveform = 2*1024;
freq = 5;
% Smallest division is 20V/65536 = 0.00030518, so choosing 0.001
binwidth = 0.0010;

testsStr =
{'5A4','5A6','5A10','5A16','5A19','5A21','5A22','5A23','5A24','5A25','5A26'}
;
% Assumes waveform files are in one folder. Input the folder location
testNames = {'C:\Users\Lab Admin\Documents\AAAFiles,
040816\5A4_102915\AE\Filtered_5A4_test1_';
    'C:\Users\Lab Admin\Documents\AAAFiles,
040816\5A6_111915\AE\Waveforms\ampAndCountAndLoadF_5A6_test1_';
    'C:\Users\Lab Admin\Documents\AAAFiles,
040816\5A10_120215\AE\test1_5A10_';
    'C:\Users\Lab Admin\Documents\AAAFiles,
040816\5A16_040516\AE\Waveforms\F_Test1_5A16_';
    'C:\Users\Lab Admin\Documents\AAAFiles, 040816\5A19_041916\AE\Waveforms
2\loadF_test1_5A19_';
    'C:\Users\Lab Admin\Documents\AAAFiles,
040816\5A21_042516\AE\Waveforms\timeF_test1_5A21_';
    'C:\Users\Lab Admin\Documents\AAAFiles,
040816\5A22_042616\AE\Waveforms\loadF_test1_5A22_'
    'C:\Users\Lab Admin\Documents\AAAFiles,
040816\5A23_042716\AE\Waveforms\loadF_test1_5A23_';
    'C:\Users\Lab Admin\Documents\AAAFiles,
040816\5A24_042916\AE\Waveforms\loadF_test1_5A24_'
    'C:\Users\Lab Admin\Documents\AAAFiles,
040816\5A25_050216\AE\Waveforms\test1_5A25_';
    'C:\Users\Lab Admin\Documents\AAAFiles,
040816\5A26_050216\AE\Waveforms\test1_5A26_'};

% Number of waveform files in the form of [ch1# ch2#; next test;...]
chNumberOfFiles = [141 408; 137 164; 140 520; 1157 2108; 934 1795;...
    653 2617; 958 1222; 888 2311; 863 2403; 658 1478; 418 1865];
% Specified threshold values
thresholds = [52 46; 53 48; 52 47; 50 45; 50 45;...
    50 45; 50 45; 50 45; 50 45; 50 45; 50 45];
```

```
% Test name, label, number of waveform files, specified threshold
% for particular test
testName = testNames{chooseTestInd};
testStr = testsStr{chooseTestInd};
numberOfFiles = chNumberOfFiles(chooseTestInd,channel);
thresholdDB = thresholds(chooseTestInd,channel);
%Changes channel number to string for file name
channelIndex = num2str(channel);
%Text files
fileType = '.txt';
% Preamp gain in dB
preamp = 40;
%Threshold gain in dB, equation from AEWin manual
thresholdVolt = (10^((thresholdDB+preamp)./20))*(10^-6);

% Preallocate
entropy1 = zeros(numberOfFiles,2);
entropy2 = zeros(numberOfFiles,2);
entropy3 = zeros(numberOfFiles,2);
maximum = zeros(numberOfFiles,2);
countsFromWaveforms = zeros(numberOfFiles,2);
time = zeros(1,numberOfFiles);
mat1 = zeros(sizeOfWaveform,1);
% Histogram bin edges and middle points for temporally weighted entropy
edges = -10:0.001:10;
mid = -10+0.0005:0.001:10-0.0005;
mat2 = zeros(sizeOfWaveform,1);
allProb = zeros(sizeOfWaveform,length(mid));
weightedProb = zeros(numberOfFiles,length(mid));


%% 3 different entropies as new signals are received
for i = 1:numberOfFiles

    %%% Loading data from iterative text files
    % Indexes through waveform numbers
    fileIndex = num2str(i);
    % Entire file name
    fileName = strcat(testName,channelIndex,'_',fileIndex,fileType);
    % Open file
    fileID = fopen(fileName);
    % Imports file to strings
    wholeWaveform = textscan(fileID,'%s','Delimiter','\n');
    timeWaveform = wholeWaveform{1,1}(11);
    workForTime= sscanf(timeWaveform{1,1},'%s%s%s%f');
    % Signal arrival time
    time(i) = workForTime(12);
    % AE signal voltage data in strings
    waveformData = wholeWaveform{1,1}(13:end);
    % AE signal voltage data in values
    for k = 1:sizeOfWaveform
        mat1(k) = sscanf(waveformData{k}, '%f');
    end
    %Close file
    fclose(fileID);

    %%% Indexing
    entropy1(i,1) = i;
    entropy2(i,1) = i;
    entropy3(i,1) = i;
    maximum(i,1) = i;
```

```
    countsFromWaveforms(i,1) = i;
    % Maximum voltage value from AE signal
    maximum(i,2) = max(mat1);
    % Counts directly from raw AE signal
    countsFromWaveforms(i,2) = sum(mat1>thresholdVolt);

    %%% 1) Feature Entropy from each waveform
    % Finding probability distribution with auto binning rules
    [prob1, Edge1] =
histcounts(mat1,'BinWidth',binwidth,'Normalization','probability');
    % Preallocate
    S1 = zeros(length(prob1),1);
    for q = 1:length(prob1)
        % Calculate individual terms of Shannon's equation for each
        % possible outcome (in this case, histogram bar)
        if prob1(q)>0
            S1(q) = -prob1(q)*log2(prob1(q));
        end
    end
    % Sum terms to get entropy
    entropy1(i,2) = sum(S1);

    %%% 2) Updated entropy from waveforms
    % Want histogram to be mobile with constant bin width. This means the
    % waveforms need to be put into one array and then passed to
    % histcounts.
    % Making one very large array with all waveforms together
    mat2(sizeOfWaveform*(i-1)+1:sizeOfWaveform*i) = mat1;
    % Finding probability distribution of all received voltage values
    [prob2, Edge2] =
histcounts(mat2,'BinWidth',binwidth,'Normalization','probability');
    % Preallocate
    S2 = zeros(length(prob2),1);
    for j = 1:length(prob2)
        % Calculate individual terms of Shannon's equation for each
        % possible outcome (in this case, histogram bar)
        if prob2(j)>0
            S2(j) = -prob2(j)*log2(prob2(j));
        end
    end
    % Sum terms to get entropy
    entropy2(i,2) = sum(S2);

    %%% 3) Temporally weighted entropy from waveforms
    % Want to devise a way so that the probability distribution of the
    % current signal has a greater effect on the system probability
    % distribution than the previous signals
    % Making one very large array with all waveforms together
    [prob, edge1] =
histcounts(mat1,'BinEdges',edges,'Normalization','probability');
    allProb(i,:) = prob; %
    % Get the current vector of arrival times
    current = time(1:i);
    % Get the temporal linear weights
    weights = current./sum(current);
    % Multiply probably distributions by weights
    weightedProb(i,:) = weights*allProb(1:i,:);
    % Preallocate
    S3 = zeros(length(weightedProb(i,:)),1);
    for j = 1:length(weightedProb(i,:))
        % Calculate individual terms of Shannon's equation for each
        % possible outcome (in this case, histogram bar)
```

```
        if weightedProb(i,j)>0
            S3(j) = -weightedProb(i,j)*log2(weightedProb(i,j));
        end
    end
    % Sum terms to get entropy
    entropy3(i,2) = sum(S3);

    % Checking all pdf's always sum to 1
    checkFor1_1 = sum(prob1);
    if checkFor1_1 > 1.0001 || checkFor1_1 < 0.9999
        str = sprintf('ERROR: PDF for %d does not sum to 1', i);
    end
    checkFor1_2 = sum(prob2);
    if checkFor1_2 > 1.0001 || checkFor1_2 < 0.9999
        str = sprintf('ERROR: PDF for %d does not sum to 1', i);
    end
    checkFor1_3 = sum(allProb(i,:));
    if checkFor1_3 > 1.0001 || checkFor1_3 < 0.9999
        str = sprintf('ERROR: PDF for %d does not sum to 1', i);
    end
    disp(i)
end
```

Appendix E – Code for Matching Modulus and AE Hits Data

```
%% Matching modulus to entropy and features at AE hits
clear all
clc

% Load AE features and modulus data
load('C:\Users\Lab Admin\Documents\AAAFiles,
040816\00_Thesis\Results\5A1619212223242526_hitdata_061516.mat');
load('C:\Users\Lab Admin\Documents\AAAFiles,
040816\00_Thesis\Results\modulus_062216.mat');

% Already in loaded data
% testsStr = {'5A16','5A19','5A21','5A22','5A23','5A24','5A25','5A26'};
% testNumber = [16,19,21,22,23,24,25,26];
% numOfTests = length(testNumber);
% crackInitTime = [4200 1582 4950 3130 6329 3420 3638 5822]; %s
% crack025mmTime = [4260 1697 5612 3145 7276 3505 3682 6067]; %s
% crack1mmTime = [4410 1757 6343 3231 8099 3701 3939 6222]; %s
% peakTimeMTS = [10.36 10.36 10.44 10.35 10.39 10.35 10.37 10.40];
% peakTimeAE = [10 10.16 10.68 10.36 9.82 10.54 10.56 10.26];
% Coefficients for damage models stored in coeff

% Preallocate
featureEntropy = cell(numOfTests,1);
updatedEntropy = cell(numOfTests,1);
tempEntropy = cell(numOfTests,1);
countsFromWaveformsA = cell(numOfTests,1);
timeFromWaveforms = cell(numOfTests,1);

% Load entropy data
workspaceNames = {'C:\Users\Lab Admin\Documents\AAAFiles,
040816\00_Thesis\Results\5A16_entropy_061316.mat';...
    'C:\Users\Lab Admin\Documents\AAAFiles,
040816\00_Thesis\Results\5A19_entropy_061316.mat';...
    'C:\Users\Lab Admin\Documents\AAAFiles,
040816\00_Thesis\Results\5A21_entropy_061316.mat';...
    'C:\Users\Lab Admin\Documents\AAAFiles,
040816\00_Thesis\Results\5A22_entropy_061316.mat';...
    'C:\Users\Lab Admin\Documents\AAAFiles,
040816\00_Thesis\Results\5A23_entropy_061316.mat';...
    'C:\Users\Lab Admin\Documents\AAAFiles,
040816\00_Thesis\Results\5A24_entropy_061316.mat';...
    'C:\Users\Lab Admin\Documents\AAAFiles,
040816\00_Thesis\Results\5A25_entropy_061316.mat';...
    'C:\Users\Lab Admin\Documents\AAAFiles,
040816\00_Thesis\Results\5A26_entropy_061316.mat'};
for I = 1:length(testsStr)
    clearvars countsFromWaveforms entropy1 entropy2 maximum maxLoad time
thresholdDB chooseTestInd testStr freq
    load(workspaceNames{I});
    featureEntropy{I,1} = entropy1(:,2);
    updatedEntropy{I,1} = entropy2(:,2);
    tempEntropy{I,1} = entropy3(:,2);
    countsFromWaveformsA{I,1} = countsFromWaveforms(:,2);
    timeFromWaveforms{I,1} = time;
end

% Concatenate AE feature data
```

```
hitdata = {hitdata_5A16_mat;hitdata_5A19_mat;hitdata_5A21_mat;
hitdata_5A22_mat;hitdata_5A23_mat;hitdata_5A24_mat;hitdata_5A25_mat;hitdata_
5A26_mat};
labels = {'Time','Load','Exten','Risetime','Counts','Duration','Amplitude',
'Abs Energy','Updated Entropy','Feature Entropy','Temporally-Weighted
Entropy'};

% Preallocate
time = cell(numOfTests,1);
load = cell(numOfTests,1);
exten = cell(numOfTests,1);
risetime = cell(numOfTests,1);
counts = cell(numOfTests,1);
duration = cell(numOfTests,1);
amp = cell(numOfTests,1);
energy = cell(numOfTests,1);
channel1 = cell(numOfTests,1);
channel2 = cell(numOfTests,1);
cycles = cell(numOfTests,1);
changeInModAtHit = cell(numOfTests,1);
damage = cell(numOfTests,1);
cumuFeat = cell(numOfTests,1);
cumuEnergy = cell(numOfTests,1);
cumuCounts = cell(numOfTests,1);
normCounts = cell(numOfTests,1);
normEnergy = cell(numOfTests,1);
normFeat = cell(numOfTests,1);
normUp = cell(numOfTests,1);
normTemp = cell(numOfTests,1);
diffCounts = cell(numOfTests,1);
diffEnergy = cell(numOfTests,1);
diffFeat = cell(numOfTests,1);
stopInd1 = zeros(numOfTests,1);
stopInd2 = zeros(numOfTests,1);
stopInd3 = zeros(numOfTests,1);
stopInd4 = zeros(numOfTests,1);
endD = zeros(numOfTests,1);
finalCounts = zeros(numOfTests,1);
finalEnergy = zeros(numOfTests,1);
finalFeat = zeros(numOfTests,1);
devCounts = zeros(numOfTests,1);
devEnergy = zeros(numOfTests,1);
devFeat = zeros(numOfTests,1);

for i = 1:numOfTests
    counter1 = 1;
    counter2 = 1;
    % Divide hit data into channel 1 and channel 2
    for j = 1:length(hitdata{i})
        if hitdata{i}(j,4) == 1
            channel1{i}(counter1,:) = hitdata{i}(j,:);
            counter1 = counter1 + 1;
        else
            channel2{i}(counter2,:) = hitdata{i}(j,:);
            counter2 = counter2 + 1;
        end
    end

    % Get rid of hits that don't match up between entropy code and hit code
    hitLength2 = length(channel2{i});
    waveformLength2 = length(updatedEntropy{i,1});
    if hitLength2 > waveformLength2
```

```
        channel2{i}(end,:) = [];
    elseif hitLength2 < waveformLength2
        featureEntropy{i}(end) = [];
        updatedEntropy{i}(end) = [];
        tempEntropy{i}(end) = [];
        countsFromWaveformsA{i}(end) = [];
        timeFromWaveforms{i}(end) = [];
    end

    time{i,1} = channel2{i}(:,1)-peakTimeAE(i);
    load{i,1} = channel2{i}(:,2);
    exten{i,1} = channel2{i}(:,3);
    risetime{i,1} = channel2{i}(:,5);
    counts{i,1} = channel2{i}(:,6);
    duration{i,1} = channel2{i}(:,7);
    amp{i,1} = channel2{i}(:,8);
    energy{i,1} = channel2{i}(:,9);
    cycles{i,1} = time{i,1}*5;
    stopInd1(i,1) = find(time{i,1}>crackInitTime(i),1);
    stopInd2(i,1) = find(time{i,1}>crack025mmTime(i),1);
    stopInd3(i,1) = find(time{i,1}>crack1mmTime(i),1);
    stopInd4(i,1) = length(time{i,1}); %Fracture

    % Find estimated modulus at AE hits
    % Exp model: change in modulus = a*exp(b*Cycles)

    endD(i) = coeff(i,1)*exp(cycles{i,1}(end).*coeff(i,2));
    % Need to divide by damage value of final AE signal so the final damage
    % value at fracture is 1
    damage{i,1} = coeff(i,1)*exp(cycles{i,1}.*coeff(i,2))/endD(i);
    cumuCounts{i,1} = cumsum(counts{i,1});
    cumuEnergy{i,1} = cumsum(energy{i,1});
    cumuFeat{i,1} = cumsum(featureEntropy{i,1});
    % Normalize all AE parameters
    normCounts{i,1} = (cumuCounts{i,1}-cumuCounts{i,1}(1))./
(cumuCounts{i,1}(end)-cumuCounts{i,1}(1));
    normEnergy{i,1} = (log10(cumuEnergy{i,1})-log10(cumuEnergy{i,1}(1)))./
(log10(cumuEnergy{i,1}(end))-log10(cumuEnergy{i,1}(1)));
    normFeat{i,1} = (cumuFeat{i,1}-cumuFeat{i,1}(1))./(cumuFeat{i,1}(end)-
cumuFeat{i,1}(1));
    normUp{i,1} = (updatedEntropy{i,1}-min(updatedEntropy{i,1}(10:end-
200)))./(max(updatedEntropy{i,1})-min(updatedEntropy{i,1}(10:end-200)));
    normTemp{i,1} = (tempEntropy{i,1}-min(tempEntropy{i,1}(1:end-
200)))./(max(tempEntropy{i,1})-min(tempEntropy{i,1}(1:end-200)));
    % Difference between actual and ideal relationships
    diffCounts{i,1} = normCounts{i,1}-damage{i,1};
    diffEnergy{i,1} = normEnergy{i,1}-damage{i,1};
    diffFeat{i,1} = normFeat{i,1}-damage{i,1};
    % Sum of the total deviations
    devCounts(i,1) = sum(abs(diffCounts{i,1}));
    devEnergy(i,1) = sum(abs(diffEnergy{i,1}));
    devFeat(i,1) = sum(abs(diffFeat{i,1}));
    % Final values for all parameter
    finalCounts(i,1) = cumuCounts{i,1}(end);
    finalEnergy(i,1) = cumuEnergy{i,1}(end);
    finalFeat(i,1) = cumuFeat{i,1}(end);
end
% Coefficients of variation
covCounts = std(finalCounts)/mean(finalCounts);
covEnergy = std(finalEnergy)/mean(finalEnergy);
covFeat = std(finalFeat)/mean(finalFeat);
```

Bibliography

[1] N. Iyyer *et al*., "Aircraft life management using crack initiation and crack growth models–P-3C Aircraft experience," *International Journal of Fatigue*, vol. 29, pp. 1584-1607, April 2007.

[2] M. E. Hoffman and P. C. Hoffman, "Corrosion and fatigue research – structural issues and relevance to naval aviation," *International Journal of Fatigue*, vol. 23, pp. S1-S10, 2001.

[3] A. Riley *et al*., *Aviation Maintenance Technician Handbook: General*, Department of Transportation, Federal Aviation Administration, Airmen Testing Standards Branch. Oklahoma City, OK, pp. 8-1–8-34, 2008.

[4] C. J. Hellier, "Acoustic emission testing," in *Handbook of Nondestructive Evaluation*. New York: McGraw-Hill, pp. 10.1-10.39, 2001.

[5] L. Pook, *Metal Fatigue: What it is, why it matters*. Dordrecht: Springer, 2007.

[6] W. Schütz, "A history of fatigue," *Engineering Fracture Mechanics*, vol. 54, no. 2, pp. 263-300, 1996.

[7] J. Schijve, *Fatigue of Structures and Materials*. Dordrecht: Kluwer Academic Publishers, 2001.

[8] U. Krupp, *Fatigue Crack Propagation in Metals and Alloy*. Weinheim: WILEY-VCH Verlag GmbH & Co. KGaA, 2007.

[9] P. Paris and F. Erdogan, "A critical analysis of crack propagation laws," *Journal of Basic Engineering*, vol. 85, no. 4, pp. 528-534, 1963.

[10] S. Suresh and R. O. Ritchie, "Propagation of short fatigue cracks," *International Metals Reviews*, vol. 29, no. 6, pp. 445-475, 1984.

[11] Y. Xue *et al*., "Microstructure-based multistage fatigue modeling of aluminum alloy 7075-T651," *Engineering Fracture Mechanics*, vol. 74, pp. 2810-2823, 2007.

[12] H. Mughrabi, "Microstructural fatigue mechanisms: cyclic slip irreversibility, crack initiation, non-linear elastic damage analysis," *International Journal of Fatigue*, vol. 57, pp. 2-8, 2013.

[13] J. C. Newman, "FASTRAN-2: A fatigue crack growth structural analysis program," NASA Technical Memorandum 104159, NASA Langley Research Center, Hampton VA, 1992.

[14] X. R. Wu *et al.*, “Small crack growth and fatigue life predictions for high-strength aluminum alloys: part I – experimental and fracture mechanics analysis,” *Fatigue & Fracture of Engineering Materials & Structures*, vol. 21, pp. 1289-1306, 1998.

[15] J. C. Newman *et al.*, “Small crack growth and fatigue life predictions for high-strength aluminum alloys: part II – crack closure and fatigue analyses,” *Fatigue & Fracture of Engineering Materials & Structures*, vol. 23, pp. 59-72, August 1999.

[16] S. C. Forth, J. C. Newman Jr., and R. G. Forman, “On generating fatigue crack growth thresholds,” *International Journal of Fatigue*, vol. 25, pp. 9-15, 2003.

[17] J. B. Jordon, J. D. Bernard, and J. C. Newman Jr., “Quantifying and microstructurally small fatigue crack growth in an aluminum alloy using a silicon-rubber replica method,” *International Journal of Fatigue*, vol. 36, pp. 206-210, 2012.

[18] J. C. Newman Jr., E. L. Anagnostou, and D. Rusk, “Fatigue and crack-growth analyses on 7075-T651 aluminum alloy coupons under constant- and variable-amplitude loading,” *International Journal of Fatigue*, vol. 62, pp. 133-143, 2014.

[19] H. Mughrabi, “Cyclic slip irreversibility and fatigue life: a microstructure-based analysis,” *Acta Materialia*, vol. 61, pp. 1197-1203, 2013.

[20] H. Mughrabi, “Damage mechanisms and fatigue lives: from the low to the very high cycle regime,” *Procedia Engineering*, vol. 55, pp. 636-644, 2013.

[21] H. Weiland *et al*., “Microstructural aspects of crack nucleation during cyclic loading of AA7075-T651,” *Engineering Fracture Mechanics*, vol. 76, pp. 709-714, 2009.

[22] C. Santus and D. Taylor, “Physically short crack propagation in metals during high cycle fatigue,” *International Journal of Fatigue*, vol. 31, pp. 1356-1365, 2009.

[23] J. Payne *et al*., “Observations of fatigue crack initiation in 7075-T651,” *International Journal of Fatigue*, vol. 32, pp. 247-255, 2010.

[24] M. Sangid, “The physics of fatigue crack initiation,” *International Journal of Fatigue*, vol. 57, pp. 58-72, 2013.

[25] O. M. Herasymchuk, “Microstructurally-dependent model for predicting the kinetics of physically small and long fatigue crack growth,” *International Journal of Fatigue*, vol. 81, pp. 148-161, 2015.

[26] C. Grosse and M. Ohtsu, *Acoustic Emission Testing: Basics for Research – Applications in Civil Engineering*. Berlin: Springer-Verlag, 2008.

[27] *AEwin Software User's Manual*, Physical Acoustic Corporation, Princeton Junction, NJ, 2007.

[28] T. M. Morton, R. M. Harrington, and J. G. Bjelectich, "Acoustic emissions of fatigue crack growth," *Engineering Fracture Mechanics*, vol. 5, pp. 691-697, 1973.

[29] M. N. Bassim, S. S. Lawrence, and C. D. Liu, "Detection of the onset of fatigue crack growth in rail steels using acoustic emission," *Engineering Fracture Mechanics*, vol. 47, no. 2, pp. 207-214, 1994.

[30] A. Berkovits and D. Fang, "Study of fatigue crack characteristics by acoustic emission," *Engineering Fracture Mechanics*, vol. 51, no. 3, pp. 401-416, 1995.

[31] T. M. Roberts and M. Talebzadeh, "Fatigue life prediction based on crack propagation and acoustic emission count rates," *Journal of Constructional Steel Research*, vol. 59, pp. 679-694, 2003.

[32] T. M. Roberts and M. Talebzadeh, "Acoustic emission monitoring of fatigue crack propagation," *Journal of Constructional Steel Research*, vol. 59, pp. 695-712, 2003.

[33] H. Chang *et al.*, "Acoustic emission study of corrosion fatigue crack propagation mechanism for LY12CZ and 7075-T6 aluminum alloys," *Journal of Materials Science*, vol. 40, pp. 5669-5674, 2005.

[34] M. Rabiei, "A Bayesian framework for structural health management using Acoustic Emission monitoring and periodic inspections," PhD dissertation, Department of Mechanical Engineering, University of Maryland, College Park, MD, 2011.

[35] Z. Han *et al.*, "Effects of micro-structure on fatigue crack propagation and acoustic emission behaviors in a micro-alloyed steel," *Materials Science & Engineering A*, vol. 559, pp. 534-542, 2013.

[36] A. Keshtgar, "Acoustic emission-based structural health management and prognostics subject to small fatigue cracks," PhD dissertation, Department of Mechanical Engineering, University of Maryland, College Park, MD, 2013.

[37] C. Sauerbrunn and M. Modarres, "Effects of material variation on acoustic emissions-based, large-crack growth model," in *Proceedings of the 2016 25th ASNT Research Symposium*, New Orleans, LA, pp. 105-109. 2016.

[38] P. A. Vanniamparambil *et al*., "An integrated structural health monitoring approach for crack growth monitoring," *Journal of Intelligent Material Systems and Structures*, vol. 23, no. 14, pp. 1563-1573, 2012.

[39] P. A. Vanniamparambil, U. Guclu, and A. Kontsos, "Identification of crack initiation in aluminum alloys using acoustic emission," *Experimental Mechanics*. pp. 1-14, 2015.

[40] E. Z. Kordatos, D. G. Aggelis, T. E. Matikas, "Monitoring mechanical damage in structural materials using complimentary NDE techniques based on thermography and acoustic emission," *Composites: Part B*, vol. 43, pp. 2672-2686, 2012.

[41] D. James and S. Carpenter, "Relationship between acoustic emission and dislocation kinetics in crystalline solids," *Journal of Applied Physics*, vol. 42, no. 12, pp. 4685-4697, 1971.

[42] A. Trochidis and B. Polyzos, "Dislocation annihilation and acoustic emission during plastic deformation of crystals," *Journal of the Mechanics and Physics of Solids*, vol. 42, no. 12, pp. 1933-1944, 1994.

[43] B. Polyzos and A. Trochidis, "Dislocation dynamics and acoustic emission during plastic deformation of crystals," *Wave Motion*, vol. 21, pp. 343-355, 1995.

[44] B. Polyzos, E. Douka, and A. Trochidis, "Acoustic emission induced by dislocation annihilation during plastic deformation of crystals," *Journal of Applied Physics*, vol. 89, no. 4, pp. 2124-2129, 2001.

[45] M. Landa *et al*., "Acoustic emission sources by atomistic simulations," *Journal of Acoustic Emission*, vol. 20, pp. 25-38, 2002.

[46] A. Spielmannová, A. Machová, and P. Hora, "Crack-induced stress, dislocations and acoustic emission by 3-D atomistic simulations in bcc iron," *Acta Materialia*, vol. 57, pp. 4065-4073, 2009.

[47] V. Chaswal *et al*., "Fatigue crack growth mechanism in aged 9Cro-1Mo steel: threshold and Paris regimes," *Materials Science and Engineering A*, vol. 395, pp. 251-264, 2005.

[48] Z. Rahman *et al*., "Incipient damage detection and its propagation monitoring of rolling contact fatigue by acoustic emission," *Tribology International*, vol. 42, pp. 807-815, 2009.

[49] S. L. McBride, J. W. MacLachlan, and B. P. Paradis, "Acoustic emission and inclusions fracture in 7075 aluminum alloys," *Journal of Nondestructive Evaluation*, vol. 2, no. 1, pp. 35-41, 1981.

[50] M. Elforjani and D. Mba, "Detecting natural crack initiation and crack in slow speed shafts with the acoustic emission technology," *Engineering Failure Analysis*, vol. 16, pp. 2121-2129, 2009.

[51] M. Lugo *et al*., "Quantification of damage evolution in a 7075 aluminum alloy using an acoustic emission technique," *Materials Science & Engineering A*, vol. 528, pp. 6708-6714. 2011.

[52] Z. Han *et al*., "Acoustic emission study of fatigue crack propagation in extruded AZ31 magnesium alloy," *Materials Science & Engineering A*, vol. 597, pp. 270-278, 2014.

[53] J. Čapek *et al*., "Study of the loading mode dependence of the twinning in random textured cast magnesium by acoustic emission and neutron diffraction methods," *Materials Science & Engineering A*, vol. 602, pp. 25-32, 2014.

[54] P. Mazal, F. Vlasic, and V. Koula, "Use of acoustic emission method for identification of fatigue micro-cracks creation," *Procedia Engineering*, vol. 133, pp. 379-388, 2015.

[55] D. Gager, P. Foote, and P. E. Irving, "Effects of loading and sample geometry on acoustic emission generation during fatigue crack growth: implications for structural health monitoring," *International Journal of Fatigue*, vol. 81, pp. 117-127, 2015.

[56] J. M. R. Parrondo, J. M. Horowitz, and T. Sagawa, "Thermodynamics of information," *Nature Physics*, vol. 11, pp. 131-139, 2015.

[57] D. J. C. MacKay, *Information theory, inference, and learning algorithms*, Cambridge: Cambridge University Press, 2003.

[58] J. P. Sethna, *Entropy, Order Parameters, and Complexity*, Oxford: Clarendon Press, 2011.

[59] C. E. Shannon, "A mathematical theory of communication," *The Bell System Technical Journal*, vol. 27, pp. 379-423, 623-656, 1948.

[60] R. Suzuki, J. Buck, and P. Tyack, "Information entropy of humpback whale songs," *Journal of Acoustic Society of America*, vol. 119, no. 3, pp. 1849-1866, March 2006.

[61] E. T. Jaynes, "Information theory and statistical mechanics," *The Physical Review*, vol. 106, no. 4, pp. 620-630, May 1957.

[62] E. T. Jaynes, "Information theory and statistical mechanics, II," *The Physical Review*, vol. 108, no. 2, pp. 171-190, October 1957.

[63] X. Guan, R. Jha, and Y. Liu, "Probabilistic fatigue damage prognosis using maximum entropy approach," *Journal of Intellectual Manufacturing*, vol. 23, pp. 163-171, 2012.

[64] X. Guan *et al.*, "Maximum relative entropy-based probabilistic inference in fatigue crack damage prognosis," *Probabilistic Engineering Mechanics*, vol. 29, pp. 157-166, 2012.

[65] H. Min, G. Jingjing, and G. Xuefei, "Probabilistic inference of fatigue damage propagation with limited and partial information," *Chinese Journal of Aeronautics*, pp. 1-11, 2015.

[66] H. Li, Y. Bao, and J. Ou, "Structural damage identification based on integration of information fusion and Shannon entropy," *Mechanical Systems and Signal Processing*, vol. 22, pp. 1427-1440, 2008.

[67] S. A. Timashev and A. V. Bushinskaya, "Markov approach to early diagnostics, reliability assessment, residual life and optimal maintenance of pipeline systems," *Structural Safety*, vol. 56, pp. 68-79, 2015.

[68] R. Unnthorsson, T. Runarsson, and M. Jonsson, "AE entropy for the condition monitoring of CFRP subjected to cyclic failure," *Journal of Acoustic Emission*, vol. 26, pp. 262-269. 2008.

[69] G. Qi, M. Fan, and G. Lewis, "An innovative multi-component variate that reveals hierarchy and evolution of structural damage in a solid: application to acrylic bone cement," *Journal of Material Science: Materials in Medicine*, vol. 23, pp. 217-228, 2012.

[70] M. Amiri and M. Modarres, "AE entropy for detection of fatigue crack initiation and growth," in *2015 IEEE Conference on Prognostics and Health Management*, Austin, TX, pp. 1-8. 2015.

[71] A. Kahirdeh, C. Sauerbrunn, and M. Modarres, "Acoustic emission entropy as a measure of damage in materials," in *35th International Workshop on Bayesian Inference and Maximum Entropy Methods in Science and Engineering*, 2015.

[72] *Standard Practice for Conducting Force Controlled Constant Amplitude Axial Fatigue Tests for Metallic Materials*, ASTM International Standard E466-07, 2007.

[73] W. D. Pilkey, *Peterson's Stress Concentration Factors*. New York: John Wiley & Sons, Inc. 1997.

[74] *Standard Test Methods for Determining Average Grain Size*, ASTM International Standard E112-12, 2012.

[75] *Standard Practice for Determining the Reproducibility of Acoustic Emission Sensor Response*, ASTM International Standard E976-15, 2015.

[76] R. Miller, "Acoustic emission: an application to fracture mechanics," PhD dissertation, Department of Mechanical Engineering, Purdue University, West Lafayette, IN, 1979.

[77] R. Peterson, *Metal Fatigue*, "Notch Sensitivity", New York: McGraw Hill, 1959.

[78] V. Ontiveros, "Strain energy density and thermodynamic entropy as prognostic measures of crack initiation in aluminum," PhD dissertation, Department of Mechanical Engineering, University of Maryland, College Park, MD, 2013.

[79] M. Rabiei, M. Modarres, "A recursive Bayesian framework for structural health management using online monitoring and periodic inspections," *Reliability Engineering and System Safety*, vol. 112, pp. 154-164. Dec. 2013.